UNIVERSITY OF CALIFORNIA SAN DIEGO

Investigations into the Combustion Interactions of Biofuels and the Optimization of Biomethane Production

A dissertation submitted in partial satisfaction of the
requirements for the degree Doctor of Philosophy

in

Engineering Sciences (Mechanical Engineering)

by

Liang Ji

Committee in charge:

Professor Kalyanasundaram Seshadri, Chair
Professor Robert Cattolica
Professor Richard K Herz
Professor Abhishek Saha
Professor Forman A Williams

2024

The Dissertation of Liang Ji is approved, and it is acceptable in quality and form for publication on microfilm and electronically.

University of California San Diego

2024

DEDICATION

I dedicate this thesis to my family and my girlfriend, whose support has been my anchor and inspiration.

To my parents, who raised me without expectations and encouraged me to pursue my dreams with selfless devotion. My mother taught me the virtues of hard work and perseverance, while my father showed me the importance of maintaining composure in the face of challenges.

To my sister, a Ph.D. student at Waseda University, whose mental guidance and support have been invaluable, especially during times of doubt and confusion.

To my girlfriend, Li Du, who has stood by me through every tough night for the past three years. Her unwavering support and assistance have been crucial to the completion of this work.

This journey has taught me to seek the truth with courage and without fear. This is not the end, nor is it the beginning of the end, but it is, perhaps, the end of the beginning.

TABLE OF CONTENTS

LIST OF FIGURES

LIST OF TABLES

ACKNOWLEDGEMENTS

I am deeply grateful to Prof. Kalyanasundaram Seshadri for his guidance as the chair of my committee. His support enabled my pursuit of a Ph.D. and instilled in me a profound commitment to seeking truth. His patience and tolerance have been crucial in my growth as a researcher.

I extend my sincere appreciation to Prof. Robert Cattolica. His financial support significantly eased my burden during my Ph.D., aiding me immensely throughout my journey.

I am thankful to Prof. Forman Williams for the enriching discussions that have greatly influenced my research. I am also indebted to Profs Saha and Herz for their valuable suggestions concerning my research.

I am grateful for the guidance of Prof. Thomas Avedisian and the assistance provided by Songtao Guo and Yujie Wang during my visit to Cornell.They provided invaluable insights into microgravity droplet flame research and set an exemplary standard in the field.

I extend my thanks to Prof. Alberto Cuoci for providing access to OpenSMOKE++ and computational resources at Politecnico di Milano, as well as to his student Lucia, who patiently taught me how to use OpenSMOKE++. Their guidance has been invaluable and greatly beneficial to my research.

Special thanks to my girlfriend, Li Du, for her companionship during challenging times and her invaluable help and selfless support, which have been key in encouraging me to persist in my research endeavors.

I express my gratitude to all my friends at UCSD; every quest for free food with you has been a wonderful adventure.

Chapter 1, in part, is a reprint of the material as it appears in *Proceedings of the Combustion Institute* 39 (2023).Experimental and computational investigation of the influence of iso-butanol on autoignition of n-decane and n-heptane in non-premixed flows by L. Ji, A. Cuoci, A. Frassoldati, M. Mehl, T. Avedisian, K. Seshadri. The dissertation author was the primary investigator and author of this paper.

Chapter 2, in part, is a reprint of the material as it appears in *Proceedings of the Combustion Institute* 40 (2024), Experimental and computational investigation of the influence of ethanol on auto-ignition of n-heptane in non-premixed flows by L. Ji, K. Seshadri, F. A. Williams. The dissertation author was the primary investigator and author of this paper.

Chapter 3, in part, is currently being prepared for submission for publication of the material. Analysis of Structure and Interactions Between Chemical Reactions, Species Transport and Heat Release in Laminar Flames, L. Ji, K. Seshadri. The dissertation author was the primary investigator and author of this material.

Chapter 4, in part, is from coauthored and unpublished material, Renewable Natural Gas Production from Biomass with Power to Gas, by L Ji, R Cattolica. The dissertation author was the primary investigator and author of this material.

VITA

2018	Bachelor of Engineering, School of Metallurgy, Northeastern University, China
2020	Master of Science, MAE Department, University of California San Diego
2024	Doctor of Philosophy, MAE Department, University of California San Diego

PUBLICATIONS

"Analysis of Structure and Interactions Between Chemical Reactions, Species Transport and Heat Release in Laminar Flames"

"Experimental and Computational Investigation of the Influence of Ethanol on Auto-ignition of n-Heptane in Non-Premixed Flows", Proceedings of the Combustion Institute. Vol 40, Issue 1-4, 2024

"Experimental and Computational Investigation of the Influence of iso-butanol on Autoignition of n-Decane and n-Heptane in Non-Premixed Flows", Proceedings of the Combustion Institute. Vol 39, Issue 2, 2022

"Rate-Ratio Asymptotic Analysis of Strained Premixed Laminar Methane Flame Under Non-adiabatic Conditions", Combustion Science and Technology. 2022

"Combustion characteristics and detailed simulations of surrogates for a Tier II gasoline certification fuel". Proceedings of the Combustion Institute. Vol 39, Issue 2, 2022

"Experimental and numerical investigation of ester droplet combustion: Application to butyl acetate", Proceedings of the Combustion Institute. Vol 39, Issue 2, 2022

FIELDS OF STUDY

Major Field: Mechanical Engineering

Studies in Combustion in Chemistry
Professors Kalyanasundaram Seshadri

Studies in Methanation
Professors Robert Cattolica

Studies in Microgravity Droplet Combustion
Professors C Thomas Avedisian

ABSTRACT OF THE DISSERTATION

Investigations into the Combustion Interactions of Biofuels and the Optimization of Biomethane Production

by

Liang Ji

Doctor of Philosophy in Engineering Sciences (Mechanical Engineering)

University of California San Diego, 2024

Professor Kalyanasundaram Seshadri, Chair

The urgent need to address the shortage of fossil fuels and mitigate environmental impacts from carbon emissions and greenhouse gases necessitates the exploration of renewable biofuels. This dissertation investigates the interactions during autoignition between biofuels and alkanes, focusing on the effects of additives on auto-ignition conditions and the catalytic methanation of biomass producer gas, augmented with hydrogen derived from power-to-gas technology, to optimize biomethane production.

The first part of the study focuses on the impact of iso-butanol on the auto-ignition of n-decane and n-heptane. Counterflow flame experiments and simulations show that small addi-

tions of iso-butanol significantly elevate the ignition temperature at low strain rates, effectively inhibiting the low-temperature chemistry of n-decane and n-heptane. Further investigations on the addition of ethanol to n-heptane using the same experimental setup and advanced computational models revealed that ethanol suppresses the low-temperature chemistry of n-heptane by competing for oxygen, particularly impacting the reaction $O_2 + CH_3CHOH \rightarrow HO_2 + CH_3CHO$.

To further investigate auto-ignition in n-heptane/ethanol counterflow diffusion flames, it is introduced a novel analytical method inspired by Zurada's sensitivity approach for neural networks. This method identifies critical species influencing the heat release rate and examines their interactions across various temperature regions. When applied to mixtures of n-heptane and ethanol under low strain rates, this method quantifies the influence of chemical kinetics and species diffusion, offering detailed insights into the interactions among species in reactive flow field.

In the second part, this study delves into biogas production, focusing on the catalytic methanation of biomass producer gas with additional hydrogen from power-to-gas. Evaluations of a Ni-Ru-MgO catalyst in both fixed and fluidized bed reactors under various conditions have been carried out to identify the optimal operational parameters. The optimal operational temperature for this catalyst in a fixed bed reactor is determined to be around 400 °C, considering both the catalyst's activation temperature and the influence of temperature on chemical equilibrium. A higher hydrogen/carbon ratio is also shown to enhance the methanation process. In fluidized bed reactors, the addition of C_2H_4 in a hydrogen-rich environment notably improves methanation, demonstrating the catalyst's adaptability across different reactor configurations.

Introduction

Fossil fuels have served as the primary energy source for industrial production and transportation for over a century. It is predicted that fossil fuel reserves could be depleted within the next 200 years. Moreover, fossil fuels are recognized as major contributors to climate change and environmental pollution due to their significant greenhouse gas emissions. Recently, there has been considerable interest in biofuels as an alternative transportation fuel, reflecting a shift towards more sustainable energy sources. Compared to traditional fuels, biofuels are considered to be more renewable and less polluting. In 2023, the U.S. Energy Information Administration estimated that 137 billion gallons of finished gasoline were consumed in the U.S, which included 13.7 billion gallons of ethanol as a gasoline additive [1, 2]. Additionally, predictions by the International Energy Agency indicate that biofuel consumption is expected to rise from 1.3 million barrels of oil equivalent per day in 2010 to 4.5 million barrels per day by 2035 [3]. These forecasts underscore the growing demand and significant future role of biofuels in the global energy mix.

Currently, the primary constituents of liquid biofuels are methanol, ethanol, and butanol [4]. Methanol is predominantly produced from fossil fuels using a catalyst [5], whereas ethanol is primarily produced from renewable resources, is less toxic, and has a higher energy density. Due to these advantages, ethanol accounted for over 90% of biofuel production in 2012 [6] and is extensively utilized as a biofuel in internal combustion engines in the United States, Brazil, and South Africa [7].

Recent interest in butanol has surged due to its advantageous properties compared to ethanol, including immiscibility with water, higher heat value (LHV), and lower vapor pressure

compared to ethanol [7, 8]. Butanol delivers a greater energy content, exhibits less corrosiveness to internal combustion engines, and poses fewer challenges in transportation. Notably, the characteristics of this four-carbon alcohol closely resemble those of traditional fossil fuels. There are four isomers of butanol: n-butanol, $CH_3CH_2CH_2CH_2OH$, 2-butanol, $CH_3CH_2CHOHCH_3$, iso-butanol, $(CH_3)_2CHCH_2OH$, and tert-butanol, $(CH_3)_3COH$. These isomers are produced through different methods. n-butanol is typically obtained via acetone-butanol-ethanol (ABE) fermentation [4, 8, 9]. A combination of fermentation and additional chemical conversion processes converts starch or cellulose to 2-butanol. Unlike the first two, tert-butanol is generally not produced biologically and is still considered a petrochemical product [8]. Iso-butanol has been produced in the petrochemical industry for many years and can also be derived from glucose fermentation using lignocellulosic biomass [10]. It's reported that Butamax retrofitted an ethanol plant to produce iso-butanol via fermentation at a cost comparable to that of cornstarch-based ethanol [11]. In 2019, Gevo demonstrated large-scale production of iso-butanol from biomass using fermentable sugars from ethanol plants [12]. Compared with n-butanol (RON=104, MON=89), iso-butanol has higher octane numbers (RON=109, MON=90) and enhances the gasoline's resistance to knocking when blended.

The first part of this thesis, encompassing Chapters 1, 2, and 3, will focus on the investigation of the combustion of mixtures of biofuels with liquid alkanes, specifically n-heptane and n-decane.

In addition to applications in the combustion of liquid biofuels, the production of gaseous biofuels is another area garnering significant attention. Biomethane, also known as renewable natural gas, is a widely used gaseous biofuel. The utilization of biomethane as an advanced renewable biofuel facilitates an improvement in air quality due to its lower greenhouse gas emissions. Biomethane has a lower heat value (LHV) of approximately 36 MJ/m³. It is indistinguishable from natural gas, which allows it to be utilized without any modifications to the existing transmission and distribution infrastructure or end-user equipment. Moreover, it is fully compatible for use in natural gas vehicles.

One method of producing biomethane involves upgrading biogas, which is a mixture of methane, carbon dioxide, and trace amounts of other gases, produced by the anaerobic digestion of organic matter in an oxygen-free environment. The specific composition of biogas varies depending on the type of feedstock and the production method used. Upgrading technologies leverage the differing properties of the gases in biogas to separate them, with water scrubbing and membrane separation accounting for almost 60% of global biomethane production today.

Another method of producing biomethane is through methanation following the thermal gasification of solid biomass. Woody biomass is first decomposed at high temperatures (between 700-800°C) and high pressure in a low-oxygen environment, converting it into a mixture of gases, primarily carbon monoxide, hydrogen, and methane, sometimes collectively referred to as syngas. To produce a pure stream of biomethane, this syngas is first cleaned to remove any acidic and corrosive components. The methanation process then employs a catalyst to promote the reaction between hydrogen and carbon monoxide or carbon dioxide to produce methane, with any remaining CO_2 or water removed at the end of this process. Our focus will be on this method—thermal gasification from biomass to produce biomethane.

During the methanation process, an excess of hydrogen is introduced. This additional hydrogen is derived from the power-to-gas process, specifically power-to-hydrogen, which involves storing surplus electricity from the grid. Utilizing hydrogen generated from surplus power not only helps stabilize the grid by providing a buffer for fluctuating power supply but also enhances the overall efficiency and quality of the biomethane produced. The integration of power-to-hydrogen technology offers several advantages: it allows for the effective utilization of intermittent renewable energy sources by converting excess electricity into hydrogen, which can be stored and used as needed. Additionally, it facilitates the decarbonization of the energy sector by replacing fossil fuel-based hydrogen with a sustainable alternative, further improving the environmental footprint of the methanation process.

The second part of the thesis, Chapter 4, will investigate the catalytic methanation of biomass producer gas, enhanced with additional hydrogen sourced from power-to-gas technol-

ogy, to optimize biomethane production. The chapter seeks to determine the most effective conditions for upgrading producer gas by assessing the impact of hydrogen/carbon ratios and process temperatures across different experimental configurations on the quality of the producing biomethane.

Chapter 1

Investigation of the Influence of *i*so-butanol on Autoignition of *n*-Decane and *n*-Heptane in Non-Premixed Flows

1.1 Introduction

The urgent need to address the depletion of fossil fuels and mitigate environmental impacts from carbon emissions and greenhouse gases has spurred significant interest in the combustion of biofuels for transportation [3, 13–17]. Biofuels, specifically ethanol and butanol isomers, provide significant benefits including higher energy density, reduced pollution, and increased renewability. As a result, blending these alcohols with gasoline has become standard practice. This trend has prompted extensive research into the interactions between butanol isomers and hydrocarbons fuels.[13, 18–25].

n-heptane is widely utilized as a primary reference fuel, alongside iso-octane, to rate the octane number of gasoline and represent linear alkanes in diesel fuels [26]. Similarly, *n*-decane is often employed as a mono-component surrogate or as part of multi-component surrogates for jet fuels to mimic their physical or combustion properties [27, 28]. Consequently, this chapter concentrates on the investigation of *n*-decane and *n*-heptane as representative alkanes. Additionally, numerous studies investigate the impact of adding biofuels to *n*-heptane or *n*-decane [21, 29–34].

Tipper and Titchard [35] investigated the effect of addition of large number of compounds on the cool flame combustion of *n*-heptane at around 533 K in a static system. Addition of olefins and alcohols was found to inhibit the low-temperature chemistry of *n*-heptane. A significant increase in ignition-delay time was observed when *iso*-butanol was added to *n*-heptane [35]. Goldsborough et al. [19] measured ignition delay times for autoignition of mixtures of research-grade gasoline with *iso*-propanol or *iso*-butanol at pressures of 20 and 40 bar and temperatures from 700 K to 1000 K. A key finding of this investigation is that at low-temperature/NTC conditions (700-860 K) the iso-alcohols inhibit first-stage reactivity of gasoline. Significantly at NTC/intermediate-temperature ranges between 860 K and 1000 K *iso*-butanol was found to promote ignition. Computations were performed using detailed chemistry and the results reproduced the experimental findings [19]. Similar results were obtained for ignition delay times measured in rapid compression machines for mixtures of *n*-butanol and *n*-heptane [21]. Addition of *n*-butanol was found to increase the ignition delay times for values of pressure between 15 bar and 30 bar and temperatures between 650 K and 830 K indicating that *n*-butanol inhibits autoignition of *n*-heptane [21]. Ignition delay times for autoignition of mixtures of alcohols with jet-fuels and petroleum derived fuels were investigated at engine-relevant conditions in a pressure vessel [20] at temperatures between 825 K to 900 K and pressures between 6 MPa to 9 MPa. The ignition delay times were found to increase with increasing addition of alcohol, thus confirming that alcohols inhibit low-temperature ignition of hydrocarbon fuels [20].

Previous experimental and computational studies have addressed combustion of droplets of *n*-butanol, *iso*-butanol, ethanol, mixtures of *n*-butanol/gasoline, *n*-heptane/*iso*-butanol, and a surrogate of gasoline/ethanol[23–25]. Measurements of droplet and flame diameters as a function of time were made and compared with predictions. The burning rate of *n*-heptane/*iso*-butanol droplets and the amount of particulates formed in these droplets decreased with increasing amounts of *iso*-butanol in the liquid [24].

Studies of autoignition in rapid compression machines and shock tube are primarily concerned with premixed systems and do not consider the influence of flow time on autoignition.

The previous studies on combustion of liquid droplets of mixtures of hydrocarbon fuels with alcohols were carried out in stagnant air and did not address autoignition of these droplets [23–25].

Here an experimental and computational investigation is carried out to characterize the influence of addition of *iso*-butanol (C_4H_8OH) on autoignition of *n*-heptane (C_7H_{16}) and *n*-decane ($C_{10}H_{22}$) employing the counterflow configuration. Critical conditions of autoignition are measured as a function of strain rate for various values of mixture ratios of the fuels. Computations are performed using detailed chemistry and compared with measurements.

1.2 Experiments and Numerical Simulations

1.2.1 Experimental Apparatus

Figure 2.2 is a schematic illustration of the "condensed-fuel" counterflow configuration

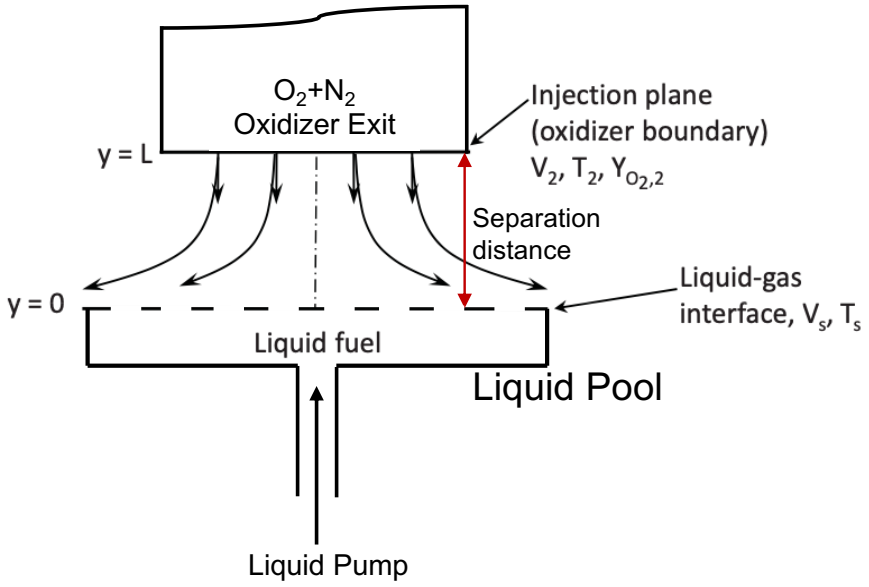

Figure 1.1: Schematic illustration of the counterflow configuration. V_2 and V_s are the velocities at the oxidizer boundary and on the gas side of the liquid-gas interface, respectively. T_2 and T_s are the temperatures at the oxidizer boundary and the liquid-gas interface, respectively, and $Y_{O_2,2}$ is the mass fraction of oxygen at the oxidizer boundary.

employed here in the experimental and computational study. In this configuration, an axisymmetric flow of a gaseous oxidizer stream is directed over the surface of an evaporating pool of a liquid fuel. The oxidizer stream is a mixture of oxygen (O_2) and nitrogen (N_2). It is injected from the oxidizer-duct, the exit of which is the oxidizer boundary. The origin is placed on the axis of symmetry at the surface of the liquid pool, and y is the axial co-ordinate and r the radial co-ordinate. The distance between the liquid-gas interface and the oxidizer boundary is L. At the oxidizer boundary, the magnitude of the injection velocity is V_2, the temperature T_2, the density ρ_2, and the mass fraction of oxygen $Y_{O_2,2}$. Here subscript 2 represents conditions at the oxidizer boundary. The radial component of the flow velocity at the oxidizer boundary is presumed to be equal to zero. The temperature at the liquid-gas interface is T_s, and the mass averaged velocity on the gas side of the liquid-gas interface is V_s. Here subscript s represents conditions on the gas side of the liquid-gas interface. It has been shown previously [36] that the radial component of the flow velocity at the liquid-gas interface is small and can be presumed to be equal to zero. It has been shown that in the asymptotic limit of large Reynolds number the stagnation plane formed between the oxidizer stream and the fuel vapors is close to the liquid-gas interface and a thin boundary layer is established there. The inviscid flow outside the boundary layer is rotational. The local strain rate, a_2, at the stagnation plane, is given by $a_2 = 2V_2/L$ [36, 37].

The counterflow burner is made up of two concentric tubes; the inner tube is ceramic and the outer tube is quartz. The inner tube has an inner diameter of 26 mm and an outer diameter of 28.6 mm. The oxidizer stream flows through the inner tube and a curtain flow of nitrogen through the outer tube. Three 200 mesh fine wire Inconel 600 screens are placed at the exit of the ceramic tube to achieve plug-flow conditions at the exit. The screens are held with Inconel rings and are recessed by 1.3 mm. As a consequence, the effective exit diameter of the oxidizer-duct, taking into consideration the thickness of the ring, is 23.5 mm. The distance between the liquid-gas interface and the oxidizer boundary, taking into consideration the thermal expansion of the oxidizer-duct, is $L = 10.5$ mm. These numbers are used to evaluate the exit velocity, V_2, and the strain rate. The one-dimensional approximation for scalar quantities employed in the numerical

formulation requires that L/D be small where D is the diameter of the oxidizer duct. The value of D is limited by volumetric flow rates of the gases. Thus $L = 10.5\,\text{mm}$ was found to be optimal for the ratio L/D that satisfies many of the limitations of the experiment and approximations employed in the simulations. A silicon carbide heating element, is placed inside the inner ceramic tube. The surface of the heating element can reach a temperature of 1900 K. To minimize heat losses to the environment the duct is surrounded by two layers of thermal insulating sheet. All gaseous streams are controlled by computer regulated analog mass flow controllers. The temperature of the oxidizer at the exit of the duct is measured using a Pt 13 % Rh thermocouple with a wire diameter of 0.21 mm and a bead diameter of 0.457 mm. The thermocouple is held in place by a ceramic holder. Since the thermocouple is placed sufficiently far from the region where ignition takes place it has negligible effect on the flow field at this location and as a consequence on the critical conditions of autoignition. The measured temperatures are corrected for radiative heat losses from the thermocouple bead using the Ranz and Marshall correlation for the Nusselt number for convective heat transfer from the gas to the spherical thermocouple bead [38, 39]. The repeatability of temperatures measured by the thermocouple is $\pm$ 5 K. Correction for radiative losses from the thermocouple bead are found to be approximately 20 K, therefore the uncertainty in radiation correction is expected to be $\pm$ 10 K. Figure 1.2 shows a photograph of the experimental setup.

1.2.2 Experimental Procedures

The procedure for measuring critical conditions of autoignition is as follows. First the flow-field is established at a specific value of the strain rate where ignition does not occur. Liquid fuel is introduced into the fuel-cup. The syringe pump is used to control the level of the liquid fuel fixed at the top of the cup. The temperature of the oxidizer stream is gradually increased in small increments, allowing sufficient time for the system to reach steady-state, until autoignition takes place. When auto-ignition occurs, the temperature of the oxidizer stream measured by

thermocouple will be recorded through LabView along with the corresponding strain rate.

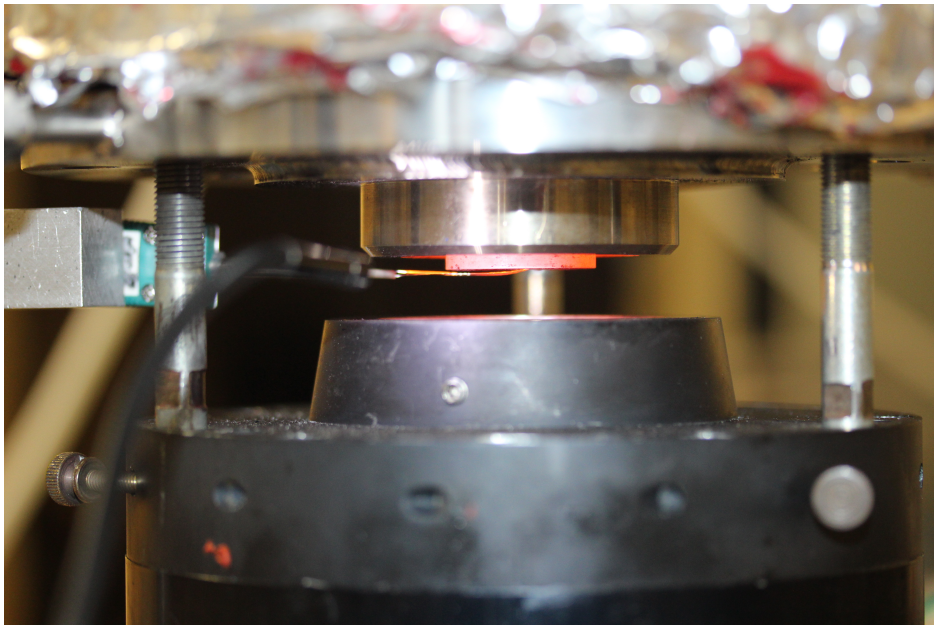

Figure 1.2: Photograph of the experimental apparatus. The photograph shows the oxidizer duct, the liquid pool and the thermocouple.

Then, the flame is extinguished by increasing the N_2 concentration and decreasing the heating power in the oxidizer stream. Following extinguishing the flame, oxidizer flow velocity will be elevated to achieve to a higher strain rate. The auto-ignition temperature for this elevated strain rate is then measured. This process is repeated to gather all auto-ignition temperature cross various strain rate. Finally, all measured auto-ignition temperatures are plotted against their corresponding strain rate for comparison.

The fuels tested are *iso*-butanol (HPLC grade, purity $\geq$ 99 %), *n*-decane (purity $\geq$ 95 %), *n*-heptane (HPLC grade, purity $\geq$ 99 %), and mixtures of *n*-decane/*iso*-butanol, and *n*-heptane/*iso*-butanol. The ratios of mixtures are 80%/20%, 50%/50% and 20%/80%, respectively. The oxidizer we used is air.

1.2.3 Measured Temperature Correction

As previously mentioned, a thermocouple made from Pt and a 13% Rh-Pt alloy, with a diameter of 0.008 inches (0.2 mm), is positioned near the duct exit to measure the temperature of the oxidizer gases. However, due to thermocouple radiation, the measured temperature may not accurately reflect the true values. To correct for this discrepancy, it is necessary to compensate for the heat loss caused by thermocouple radiation.

Initially, the thermocouple junction is assumed to be spherical. For temperature correction of the spherical joint, the Ranz & Marshall correction [39] is employed. Established in 1952, this method explains the heat transfer between a spherical particle and the surrounding plasma gas. The correlation equation used is:

$$\mathrm{Nu} = h\frac{d_{tc}}{k} = 2.0 + 0.6 \times \mathrm{Re}^{1/2}\mathrm{Pr}^{1/3} \tag{1.1}$$

The Reynolds number $\mathrm{Re} = \frac{\rho_\infty (V_\infty - V_{tc}) d_{tc}}{\mu}$ and the Prandtl number $\mathrm{Pr} = \frac{\mu c_p}{\kappa}$ are key parameters in temperature correction. Here, ρ_∞ and V_∞ represent the density and velocity of the hot air, respectively. To determine the average velocity of the air, we divide the volume flow rate by the cross-sectional area of the oxidizer duct. The values for the heat capacity c_p, dynamic viscosity μ, and thermal conductivity κ of the hot air are obtained from standard tables and linearly interpolated to achieve precise data. The diameter of the thermocouple, d_{tc}, critical for our calculations, is directly measured to be 0.457 mm. The heat transfer coefficient h, at the interface between the hot air and the thermocouple joint, is obtained from Eq. 1.1 as the output value.

For the thermocouple joint, we assume energy is balanced between heat convection from the air and heat radiation to the surrounding space. This equilibrium is expressed by the following equation:

$$h \times (\mathrm{T}_{gas} - \mathrm{T}_c) = \varepsilon \times \sigma \times (T_c^4 - T_{surr}^4) \times \frac{1}{2} \tag{1.2}$$

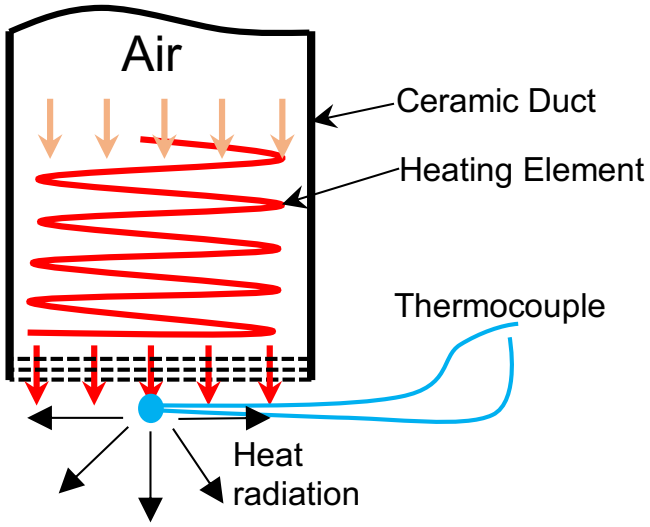

Figure 1.3: Illustration of energy balance of the thermocouple.

The emissivity, ε, is assumed to be 0.2. The Stefan–Boltzmann constant, σ, is set at 5.67×10^{-8} W·m^{-2}·K^{-4}. T_c represents the measured thermocouple temperature, while T_{gas} denotes the actual gas temperature. T_{surr} refers to the surrounding temperature, which is considered to be at room temperature.

Figure 1.3 illustrates the energy balance of the thermocouple located at the exit of the oxidizer duct. The air within the duct is heated by a heating element in ceramic material. Given the proximity of the thermocouple to the duct exit, the heat radiation flux between the thermocouple and the duct exit is considered negligible relative to the radiation flux emitted to the lower hemispherical space. Therefore, it is assumed that the radiative heat loss from the thermocouple is directed into hemispherical space, justifying the application of the factor $\frac{1}{2}$ to the radiation term in Equation 1.2.

In the calculation, the thermocouple temperature T_c is obtained from measurement, and all properties of gas, such as density, viscosity and thermal conductivity are initially evaluated at T_c. Equation 1.1 is then solved to determine the heat transfer coefficient based on the initially assumed temperature of the gas. This heat transfer coefficient is subsequently used in Equation 1.2 to update the gas temperature. The updated gas temperature is then utilized in a subsequent

iteration of Equation 1.1. This iterative process is repeated until the gas temperature converges. The converged value is then used as the corrected temperature of the gas.

1.2.4 Numerical Model

The computations were performed with the OpenSMOKE++ framework [40] developed by the CRECK Modeling Lab. The structure of the reactive flow-field is obtained by solving the one-dimensional transport equations of mass, momentum and energy and described in detail elsewhere [41, 42]. Boundary conditions are applied at the oxidizer boundary and at the liquid-gas interface [36, 43, 44]. At the oxidizer boundary, the injection velocity V_2, the temperature, T_2, and the value of $Y_{O_2,2}$ are specified, and the radial component of the flow velocity is assumed to be zero. Equations (1.3)-(1.6) shows the mixed boundary conditions for species conservation and energy conservation that are applied at the liquid-gas interface.

$$\dot{m}Y_{i,s} + j_{i,s} = 0 \tag{1.3}$$

$$\dot{m}\left(1 - \sum_j Y_{j,s}\right) - \sum_j j_{j,s} = 0 \tag{1.4}$$

$$\left[\lambda \left(dT/dy\right)\right]_{\mathrm{s}} - \dot{m}\sum_j Y_{j,l} h_{\mathrm{j,l}} = 0 \tag{1.5}$$

$$P_{\mathrm{v,j}} X_{j,l} - p X_{j,s} = 0 \tag{1.6}$$

Here subscripts i and j respectively refer to non-evaporating and evaporating species (specifically components of the liquid fuel), $\dot{m}$ is the mass evaporation rate, $Y_{i,s}$, and $j_{i,s}$ the mass fraction and diffusive flux of the non-evaporating species, $Y_{j,s}$, $X_{j,s}$ and $j_{j,s}$ the mass fraction, mole fraction and diffusive flux of the evaporating species on the gas side of the interface, λ the

thermal conductivity of the gas, $Y_{j,l}$, $X_{j,l}$, $h_{j,l}$, and $P_{\mathrm{v,j}}$ the mass fraction, mole fraction, heat of vaporization and vapor pressure of component j in the liquid, and p the total pressure. The total mass flux of all species, i, on the gas-side of the liquid-gas interface is comprised of the diffusive flux, $j_{i,s}$, and the convective flux $\dot{m}Y_{i,s}$.

The Eq. (1.3) imposes the condition that the total mass flux for all species, excluding those from evaporating fuel components, is zero at the liquid-gas interface. This assumption is based on the premise that gaseous species cannot dissolve in the liquid pool.

Unlike transient evaporation of a multicomponent liquid droplet, which is a closed system with moving boundaries, where the flux of different components of the fuel evaporating from the surface of the liquid droplet changes with time, the counterflow burner is an open-system where the liquid fuel in the cup is continuously replenished from a reservoir and the liquid-gas interface is a fixed boundary. In view of mass conservation, at steady-state the incoming mass flux of the multicomponent liquid fuel from the reservoir to the fuel-cup must be equal to the mass flux of fuel vapors evaporating from the liquid-gas interface. This outgoing flux has convective, $\dot{m}\sum_j Y_{j,s}$, and diffusive, $\sum_j j_{j,s}$, components. Thus, the Eq. (1.4) imposes the constraint that this outgoing total flux must be equal to the sum of incoming mass flux, $\dot{m}$. If the boiling points of the components of the fuel are not the same, diffusion gradients will be established in the pool such that the fluxes remain the same as the incoming flux from the reservoir.

The Eq. (1.5) imposes the condition that the heat conduction at the liquid-gas interface is balanced by the sum of all products of $\dot{m}$ and the heat of vaporization of the fuel components.

Assuming the liquid mixture behaves as an ideal mixture, Raoult's law is applied to the boundary conditions. This law states that the partial pressure of each component in an ideal liquid mixture equals the vapor pressure of the pure component multiplied by its mole fraction in the solution. As vapor pressure, $P_{\mathrm{v,j}}$, depends on temperature, equation (1.6) is crucial for determining the interface temperature, T_{s}.

For simplification, it is assumed that the pool is well mixed and the mole fractions of the components of the liquid fuel are the same everywhere in the pool and equal to that in the

reservoir. Experimental confirmation that the fluxes remain the same was established in an earlier experimental study on extinction of flames stabilized over pools of jet fuels and surrogates of jet fuels made up of mixtures of fuels with different boiling points [45]. It was possible to stabilize flames over a long period of time and no movement of the flamesheet was observed confirming that the mass flux of the reactants evaporating from the liquid-gas interface was constant and did not change.

Empirical coefficients for calculating the vapor pressure, and the heat of vaporization, for these fuels are given in [46].

1.2.5 Chemical Mechanism

Kinetic modeling is carried out using the recently updated version of the comprehensive CRECK chemical kinetic mechanism, CRECK_2003_TOT_HT_LT [47]. A detailed description of the core chemistry of the CRECK kinetic mechanism is described elsewhere [48]. The kinetic mechanism for the pyrolysis and oxidation of *n*-alkanes was updated to include new reaction classes, to facilitate better prediction of the reactivity of alkanes, including *n*-decane at very low temperatures [49]. Details of combustion of butanol isomers employed in the mechanism are described elsewhere [14, 50].

The Figure 1.4 illustrates a simplified oxidation mechanism for n-decane, as reported in [51]. The mechanism is predominantly governed by the reactions of decyl radicals ($nC_{10}H_{21}\cdot$) with molecular oxygen. At low temperature and moderate pressures, the reaction of decyl radicals with O_2 proceeds largely but not exclusively by association to form the decylperoxy radical ($R_{10}OO\cdot$). This radical typically undergoes isomerization through internal hydrogen atom abstraction, leading to the creation of a hydroperoxydecyl radical, often denoted by $\cdot Q_{10}OOH$. Being a substituted alkyl radical with the unpaired electron located on a carbon atom, $\cdot Q_{10}OOH$ is vulnerable to further attack by a second O_2 molecule, forming $\cdot OOQ_{10}OOH$. The $\cdot OOQ_{10}OOH$ can undergo isomerization, via internal H abstraction, to produce ketohydroperoxide and subse-

quently dissociate into multiple radicals, thereby facilitating a chain-branching pathway at low temperatures [52].

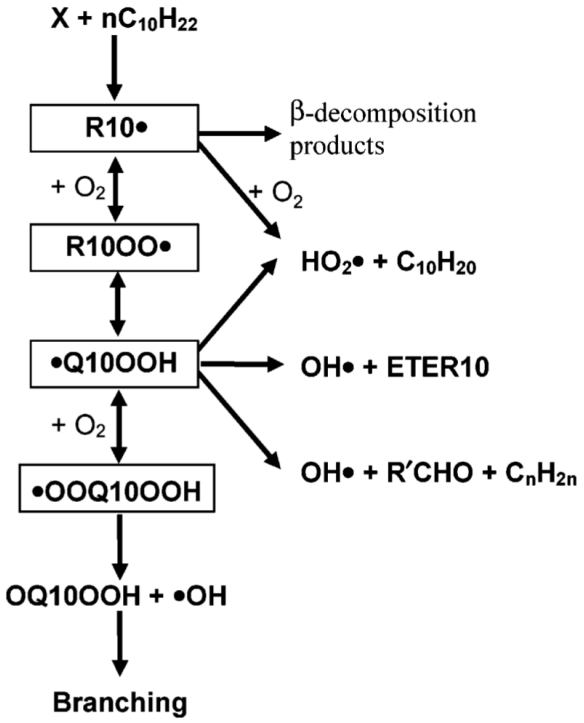

Figure 1.4: Simplified low temperature oxidation mechanism of n-decane[51]

1.2.6 Simulation Procedures

In the simulation, a process similar to the experimental measurement is employed, beginning from unreactive ambient conditions at (300 K), steady state solution will be obtained initially.

Then, the boundary condition at the exit of the oxidizer duct is modeled using a rate of rise for the oxidizer stream temperature of 0.1 K/s to solve governing equations in this field. This value is sufficiently slow, because with faster temperature rise rates (1 K/s) the model predicts the same autoignition temperatures.

As the oxidizer temperature reaches a certain threshold, ignition is indicated by a temperature profile where the highest temperature occurs in the flow field, not on the oxidizer side.

When the temperature difference between the oxidizer and the highest point reaches 10K, this oxidizer temperature is recorded as the auto-ignition temperature. It is observed that the oxidizer temperatures corresponding to a 10K and a 1000K temperature difference are close. However, achieving a fully ignited flame solution takes significantly longer at 1000K, which supports using the simpler measure of a 10K difference for determining the auto-ignition temperature.

This procedure will be repeated across higher strain rates and various fuels. Finally, the recorded auto-ignition temperatures will be plotted against the corresponding strain rates to compare with the measured results.

1.3 Results and Discussion

Figures 1.5, 1.6 and 1.8, show the temperature of the air at autoignition, T_{ig}, as a function of strain-rate, a_2, for the various fuels and fuel mixtures. In these figures the symbols represent experimental data and the lines are predictions. In general, at a given value of the strain rate, the predicted T_{ig} for all fuels and fuel mixtures are higher than those for the measurements and the differences between these values decrease with increasing strain rate. These differences could partly be attributed to inaccuracies in estimating the radiation correction to the temperature measured by the thermocouple as a consequence of uncertainties in correlation for the Nusselt number used to evaluate the convective heat transfer from the gas to the thermocouple and uncertainties in estimating values of the thermal conductivity of the gas and emissivity of the thermocouple bead. Close to the critical conditions of autoignition small disturbances in the flow field or fluctuation in temperature can lead to premature ignition and as a consequence, the measured temperature would be less than the actual value. It has been observed in an earlier investigation that uncertainties in evaluating coefficient of diffusion of fuels will result in inaccuracies in the prediction of T_{ig} [43]. Figure 1.5 shows critical conditions of autoignition for *iso*-butanol, *n*-decane, and *n*-heptane. The experimental data and computations show that at low strain rates *n*-decane is the easiest to ignite followed by *n*-heptane and *iso*-butanol, while

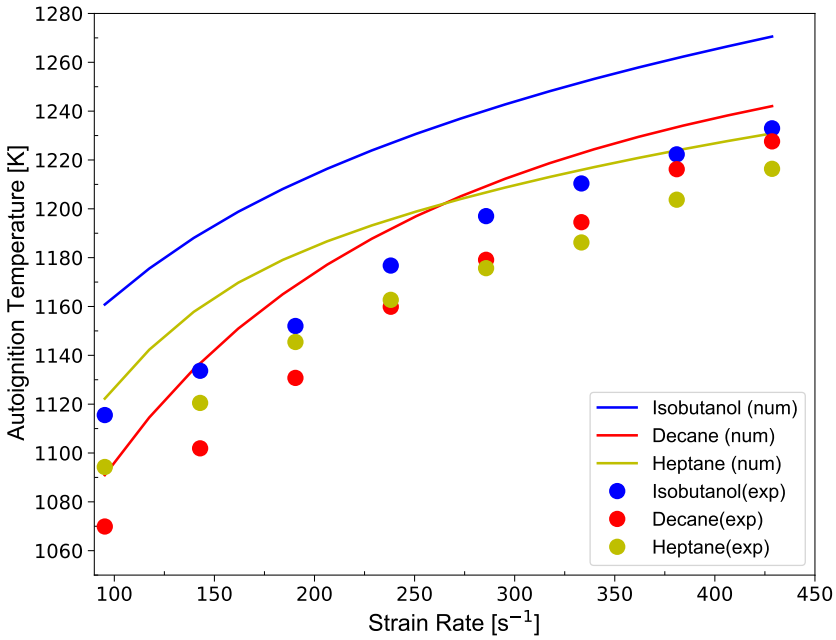

Figure 1.5: The temperature of the air at autoignition of *iso*-butanol, *n*-decane, and *n*-heptane as a function of strain-rate, a_2. The symbols represent experimental data and the lines are predictions. The uncertainty in experimental data is $\pm$ 10 K.

at high strain rates *n*-heptane is the easiest to ignite followed by *n*-decane and *iso*-butanol. The "crossover" between the values of T_{ig} for *n*-decane and *n*-heptane shown in Fig. 1.5 was experimentally observed and reported in a previous study [36] and is attributed to competition between low-temperature chemistry, high-temperature chemistry and molecular transport [43]. At low-strain there is sufficient residence time for low-temperature chemistry to be active, hence *n*-decane ignites at a lower temperature than *n*-heptane. At high-strain rates there is insufficient residence time for low-temperature chemistry to be active and molecular transport becomes important. Since, *n*-heptane diffuses at a higher rate than *n*-decane, it has a lower T_{ig} than *n*-decane [43].

Figure 1.6 shows measured and predicted critical conditions of autoignition for *n*-decane, *iso*-butanol, and mixtures of *n*-decane/*iso*-butanol. Computations and experimental data show that for all a_2, the value of T_{ig} for *n*-decane is less than that for *iso*-butanol. They also show

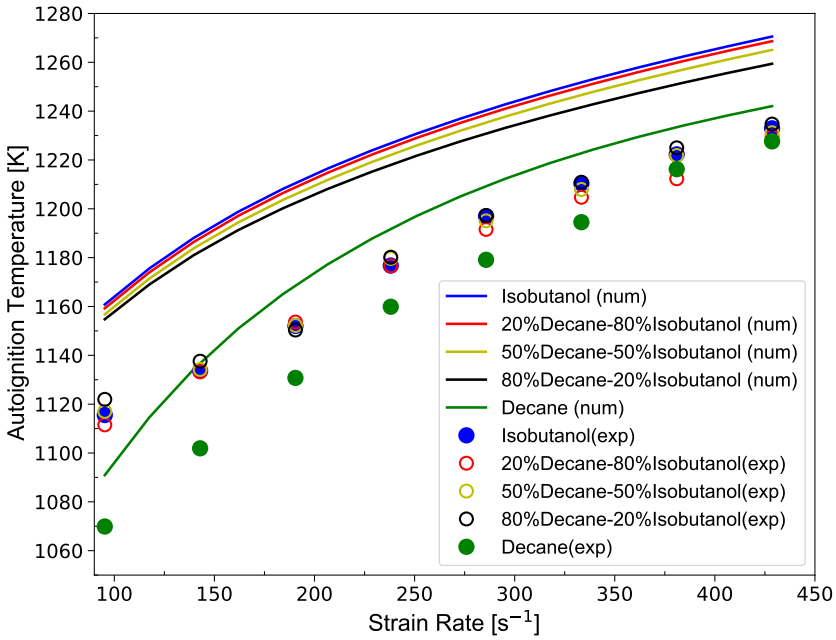

Figure 1.6: The temperature of the air at autoignition, of *n*-decane, *iso*-butanol, and liquid mixtures of *n*-decane/*iso*-butanol with percent volume ratios of 80/20, 50/50, and 20/80, as a function of strain-rate, a_2. The symbols represent experimental data and the lines are predictions obtained using detailed chemistry. The uncertainty in experimental data is $\pm$ 10 K.

that at low strain rates addition of small amount (20 %) of *iso*-butanol to *n*-decane increases T_{ig} by a significant amount from that for *n*-decane, indicating that addition of *iso*-butanol strongly inhibits the low-temperature chemistry of *n*-decane.

The calculations predict that for a given a_2, the values of T_{ig} for the mixtures are between those for *n*-decane and *iso*-butanol. Moreover, it is observed the value of T_{ig} increases as the proportion of amounts of *iso*-butanol. The experimental data show that T_{ig} for the mixtures are nearly the same as those for *iso*-butanol and the differences are well within experimental uncertainties.

Figure 1.7 shows predictions made with the complete mechanism and those with the low-temperature reactions removed from the kinetic model (labeled as HT in Fig. 1.7). For *n*-decane, at low strain rates, T_{ig} calculated using complete kinetic model is lower than that

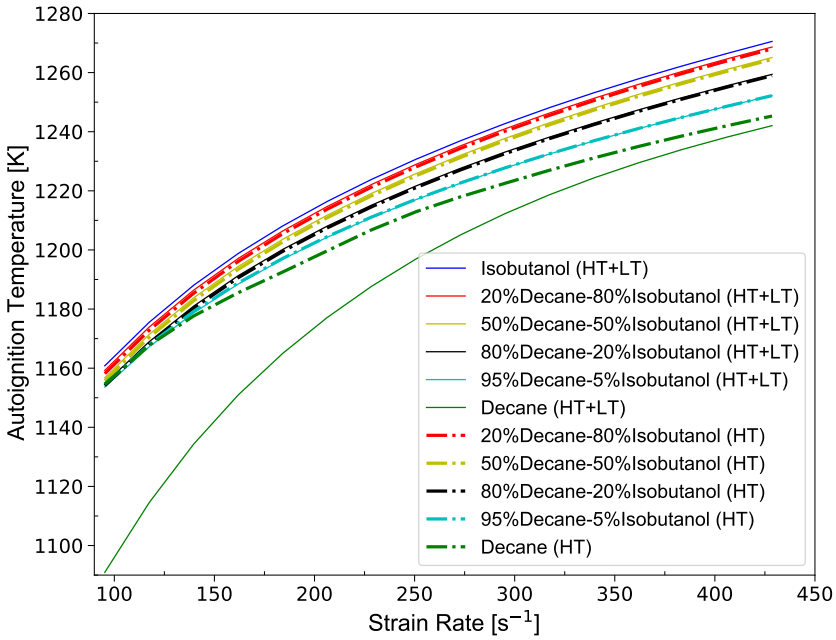

Figure 1.7: The predicted temperature of the air at autoignition, T_{ig}, of *n*-decane, *iso*-butanol, and mixtures of *n*-decane/*iso*-butanol with percent volume ratios of 80/20, 50/50, and 20/80 and 95/5, as a function of strain-rate, a_2. The figure shows predictions with the complete kinetic mechanism and those with low-temperature chemistry removed (HT).

calculated using high-temperature chemistry and the differences decrease with increasing a_2, indicating that at low strain rates autoignition is promoted by low temperature chemistry and there is insufficient residence time for low temperature to be active at high strain rates. A remarkable result is that the critical conditions of autoignition for the mixtures calculated using the complete kinetic model and those calculated neglecting low-temperature chemistry are the same even for mixtures containing only 5 % *iso*-butanol by liquid volume indicating that addition of *iso*-butanol has suppressed low-temperature chemistry of *n*-decane.

Figure 1.6 shows that at low strain rates the mixtures have nearly the same autoignition temperature as that of *iso*-butanol because as shown in Fig. 1.7, the autoignition temperature of pure *n*-decane calculated neglecting low temperature chemistry is close to that of *iso*-butanol. Since *iso*-butanol interferes with the radical pool and as a consequence with the low temperature

chemistry of *n*-decane, the autoignition temperature for the mixtures can be expected to be close to those for *iso*-butanol and *n*-decane calculated neglecting low-temperature chemistry as shown in Fig. 1.6.

In Figure 1.6, as the strain rate increases, for pure *n*-decane, the deviation in auto-ignition temperature between the complete mechanism and the mechanism excluding low-temperature processes decreases. This suggests that the impact of the low-temperature mechanism on auto-ignition diminishes with an increased strain rate. At a strain rate of 425 s^{-1}, the auto-ignition temperatures are nearly identical between the high-temperature (HT) mechanism and the complete mechanism. This may be because at high strain rates, there is insufficient residence time for low-temperature chemistry to occur, thereby limiting its influence.

Unlike the distribution of autoignition temperatures of mixtures at low strain rates, which are nearly the same, the autoignition temperatures at a high strain rate (e.g. 425 s^{-1}) are evenly distributed between pure *iso*-butanoland *n*-decane. This confirms that the phenomenon where autoignition temperatures are concentrated at low strain rate near the autoignition temperature of *iso*-butanol is primarily due to the inhibition of the low-temperature mechanism.

Figure 1.8 shows experimental and computation results similar to those in Fig. 1.6 with *n*-decane replaced by *n*-heptane. They show that at low strain rates T_{ig} for *n*-heptane is significantly lower than that for the mixtures and the differences between these values decreases with increasing strain rate. This clearly indicates that addition of *iso*-butanol inhibits the low temperature chemistry of *n*-heptane. The experimental data show that T_{ig} for the mixtures, at strain rates greater than $250\,s^{-1}$, is nearly the same as that for *iso*-butanol, while for $a_2 < 250\,s^{-1}$, they are slightly larger than that for *iso*-butanol. The computations, however, predict that the value of T_{ig} for the mixtures increases as the proportion of amounts of *iso*-butanol. The departures from linear behavior indicated by the experimental data for the mixtures remains to be investigated.

Figure 1.9 shows results similar to those in Fig. 1.7 with *n*-decane replaced by *n*-heptane. The simulations again show that the addition *iso*-butanol significantly increases the value of T_{ig} from that for *n*-heptane thus inhibiting low-temperature chemistry of *n*-heptane.

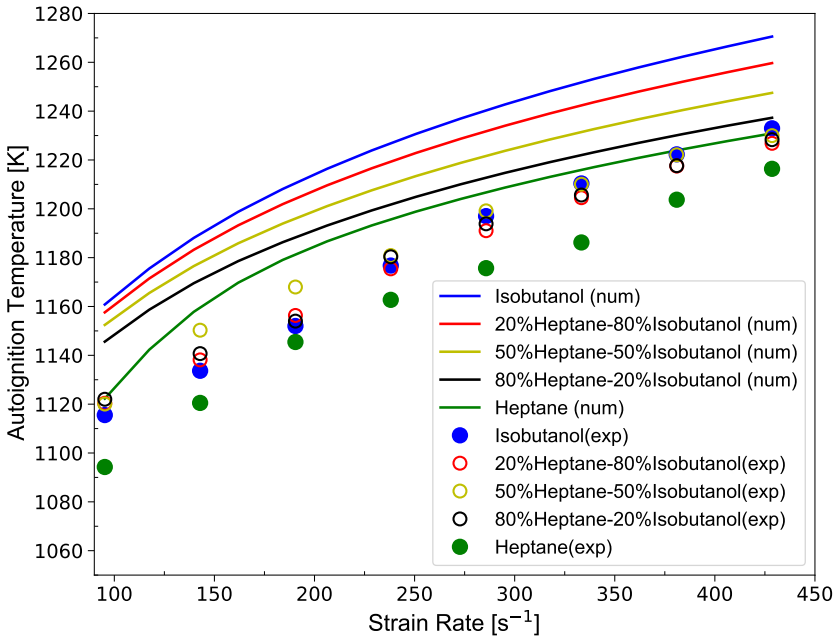

Figure 1.8: The temperature of the air at autoignition, T_{ig}, of *n*-heptane, *iso*-butanol, and mixtures of *n*-heptane/*iso*-butanol with percent volume ratios of 80/20, 50/50, and 20/80, as a function of strain-rate, a_2. The symbols represent experimental data and the lines are predictions obtained using detailed chemistry. The uncertainty in experimental data is $\pm$ 10 K.

Figures 1.10, 1.11, and 1.12 compare aspects of flame structure and results of sensitivity analysis at $a_2 = 100\,\mathrm{s}^{-1}$ and at $a_2 = 450\,\mathrm{s}^{-1}$ for mixtures of 100%/0%, 95%/5%, 80%/20%, 50%/50%, 20%/80%, and 0%/100% by volume of *n*-decane/*iso*-butanol.

In Fig. 1.10 the heat release rate profile in the mixing layer above a liquid pool of 100 % *n*-decane shows two peaks; the first corresponds to heat release from low temperature chemistry and the second is indicative of hot ignition. It is noteworthy that the first peak is more pronounced at $a_2 = 100\,\mathrm{s}^{-1}$ when compared to that at $a_2 = 450\,\mathrm{s}^{-1}$ confirming the previous observation [36, 43] that low temperature chemistry is dominant at low strain rates. The temperature in the mixing layer at the axial location where the rates of low temperature chemistry is a maximum is approximately 750 K which is close to the crossover temperature defined by Peters et al. [53]. Figure 1.10 shows that when *iso*-butanol is added to *n*-decane, the first peak disappears even at

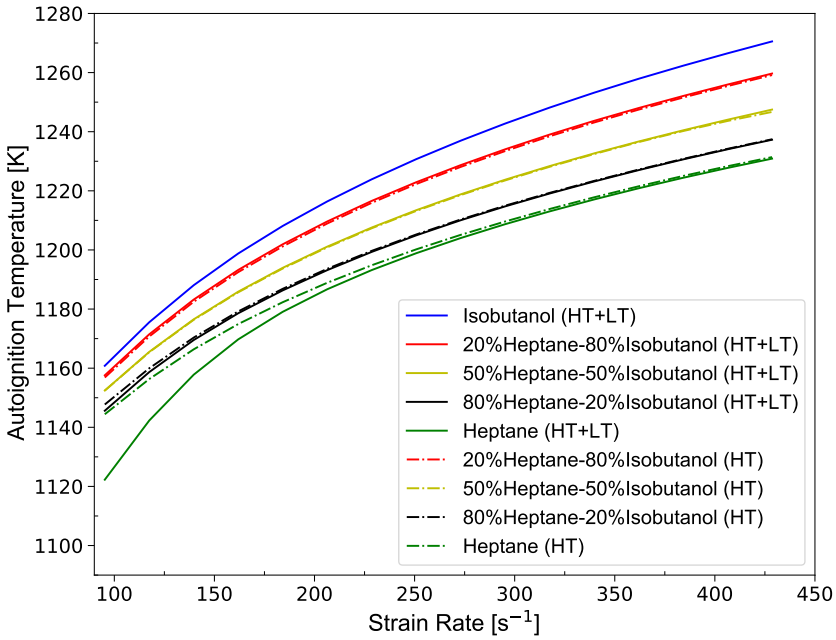

Figure 1.9: The predicted temperature of the air at autoignition, T_{ig}, of *n*-heptane, *iso*-butanol, and mixtures of *n*-heptane/*iso*-butanol with percent volume ratios of 80/20, 50/50, and 20/80, as a function of strain-rate, a_2. The figure shows predictions with the complete kinetic mechanism and those with low-temperature chemistry removed (HT).

low strain rates indicating that low-temperature chemistry of *n*-decane has been suppressed.

Figure 1.11 shows the significant effect of liquid fuel composition on the temperature and mole fractions of *n*-decane, *iso*-butanol, *n*-decane-ketohydroperoxide (*n*-C_{10}-OQOOH) and hydrogen peroxide (H_2O_2) in the gas phase at the liquid-gas interface. Note that the temperature at the liquid gas interface is not significantly affected by the strain rate. In general, the liquid temperature is about 20 to 30 K below the corresponding boiling point (447 K for *n*-decane, and 381 K for *iso*-butanol). As a consequence of the large difference in volatility of *n*-decane and *iso*-butanol, a small amount of *iso*-butanol is sufficient to reduce the temperature at the surface of the liquid fuel, and the mass fraction of *n*-decane in the gas phase at the liquid-gas interface.

Figure 1.11 shows that, in the gas phase, the mole-fraction of *iso*-butanol is higher than that of *n*-decane for all values of mole fraction of *n*-decane in the liquid less than 80 %. In the

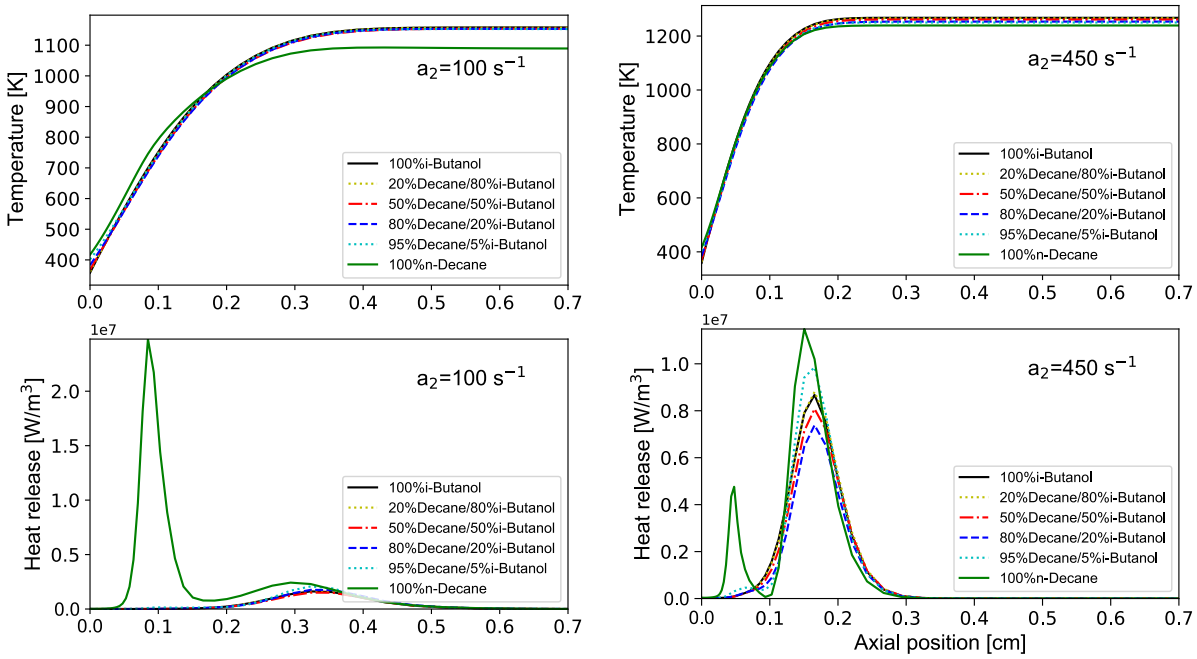

(a) $a_2 = 100\ s^{-1}$ **(b)** $a_2 = 450\ s^{-1}$

Figure 1.10: Axial temperature and heat release rate profiles just before the onset of autoignition for liquid mixtures of 100%/0%, 95%/5%, 80%/20%, 50%/50%, 20%/80%, and 0%/100% (by liquid volume) of *n*-decane/*iso*-butanol.

gas-phase, the sum of the mole fractions of *iso*-butanol and *n*-decane is less than unity for all values of mole fraction of *n*-decane in the liquid. As a consequence, the flux balance indicated by the Eq. (1.4) is satisfied. Hence the total outgoing flux of the vaporized fuel components are equal to the incoming flux. Better prediction of the mole fraction of the fuel in the gas-phase can be achieved by replacing the well mixed model for the fuel components in the fuel-cup by an analysis of the convective and diffusive transport in the fuel-cup. An improved model that incorporates these factors will be employed in the next chapter for further investigation.

The well mixed model will likely overpredict the value of mole fraction of *iso*-butanol in the gas-phase. The influence of this overprediction on predicted T_{ig} is expected to be small because, as shown in Fig. 1.7, T_{ig} for the mixtures follow a linear trend and are bounded on either side by predicted value of T_{ig} for *iso*-butanol and *n*-decane calculated neglecting low-temperature chemistry. The role of the low temperature chemistry, which is negligible for *iso*-butanol, is

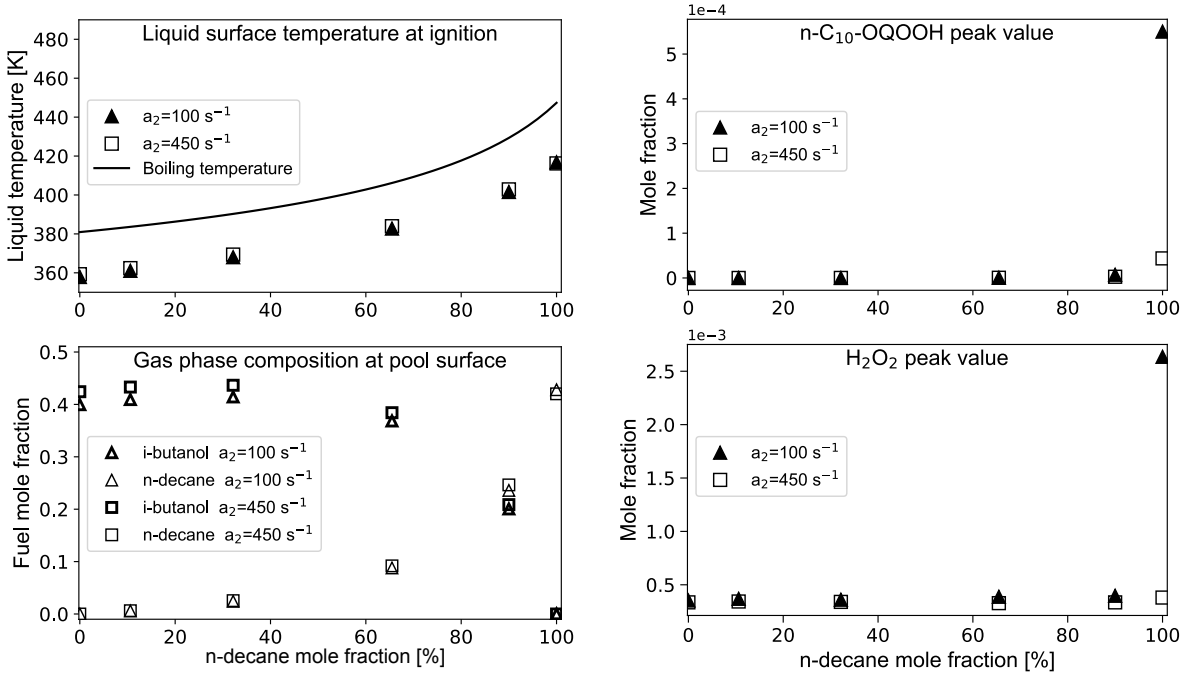

Figure 1.11: The temperature at the surface of the liquid pool, and values of the mole fraction of *n*-decane, *iso*-butanol, *n*-decane-ketohydroperoxide (*n*-C_{10}-OQOOH) and hydrogen peroxide (H_2O_2) in the gas phase at the liquid-gas interface as a function of mole fraction of *n*-decane in the mixture *n*-decane/*iso*-butanol in the liquid pool at $a_2 = 100\,\mathrm{s}^{-1}$ and at $a_2 = 450\,\mathrm{s}^{-1}$. The peak values are at various axial locations

.

evident only for the case where the liquid fuel is entirely *n*-decane. Figure 1.11 shows the peak values of H_2O_2 and *n*-decane-ketohydroperoxide are approximately at the same axial location as the peak of the heat release in the low temperature region of the mixing layer shown in Fig. 1.10.

The second plot in Fig. 1.10 illustrates the formation rates of *n*-decane-ketohydroperoxide decrease when 10% vol *iso*-butanol is added to *n*-decane. Since *n*-decane-ketohydroperoxide is a crucial radical involved in low-temperature chemistry, this finding confirms the suppression effect of *iso*-butanol. Notably, in this mixture, the gas-phase mole fraction of *n*-decane is approximately equal to that of *iso*-butanol, further highlighting the significant impact of *iso*-butanol on the chemical dynamics.

The results of the sensitivity analysis for 100% *n*-decane shown in the Fig. 1.12 confirms the dominant role of the low temperature chemistry in promoting autoignition of *n*-decane

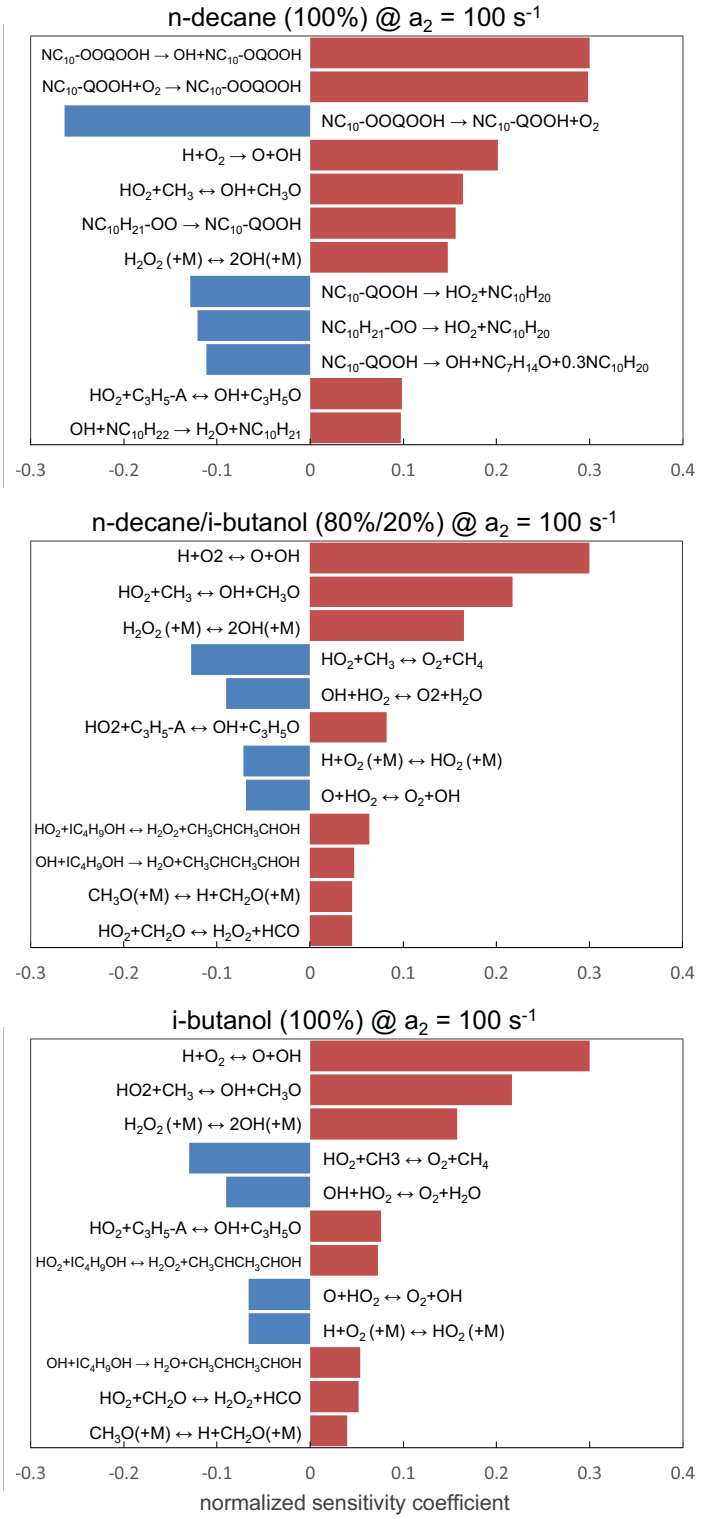

Figure 1.12: Maximum sensitivity coefficient for temperature just before the onset of autoignition for 100%/0%, 80%/20%, 0%/100% (by liquid volume) of *n*-decane/*iso*-butanol at $a_2 = 100\,\mathrm{s}^{-1}$. Positive sensitivity coefficients identify reactions that enhance the reactivity of the system, favoring autoignition.

at low strain rates as a result of high sensitivity of the kinetic steps that include *n*-decane-ketohydroperoxide.

The similarity in the sensitivity analysis results between pure *iso*-butanol and the 80% *n*-decane/20% *iso*-butanol mixture indicates a similar mechanism of auto-ignition for both. In the 80% *n*-decane/20% *iso*-butanol mixture, the gas-phase presence of *n*-decane is approximately equal to that of *iso*-butanol. This similarity, observed in both the pure *iso*-butanol and the mixture, is due in part to the inhibitory effect of *iso*-butanol on low-temperature chemistry.

Moreover, when *iso*-butanol is present in the liquid fuel, a small amount of *n*-decane is available in the gas phase and its low concentration maynot effectively sustain the low temperature degenerate branching oxidation process. As a result, autoignition of 100 % *iso*-butanol and the 80 %/20 % *n*-decane/*iso*-butanol mixtures is controlled by the chain branching reaction H + O_2 and reactions of HO_2 forming OH or H_2O_2, followed by decomposition of H_2O_2 to OH.

1.4 Concluding Remarks

Experiments and simulations confirm that addition of *iso*-butanol inhibits the low-temperature chemistry of *n*-decane and *n*-heptane, especially at low strain rate. The results obtained in this research complements previous studies on influence of iso-alcohols on autoignition in premixed systems [19, 20, 35].

The comparison of results from mechanisms that include low-temperature chemistry versus those that exclude it reveals that the influence of low-temperature chemistry on the auto-ignition of *n*-decane diminishes as the strain rate increases.

The further sensitivity analysis of temperature confirms the dominant role of the low temperature chemistry in promoting autoignition of n-decane at low strain rates and shows that the rates of formation of *n*-decane-ketohydroperoxide are sharply declined when *iso*-butanol is added to *n*-decane.

The impact of liquid fuel composition on the mole fractions of *n*-decane and *iso*-butanol

in the gas phase suggests that the mole fraction of *n*-decane plays a crucial role in the low-temperature degenerate branching oxidation process. This observation highlights the need to develop a more refined liquid-pool model that replaces the existing well-mixed model, which may lead to the over-prediction of *iso*-butanol mole fraction.

In future research, it would be of interest to isolate those kinetic steps that arise from addition of *iso*-butanol which compete with the kinetic steps that form *n*-decane-ketohydroperoxide. Identification of these kinetic steps would give a better fundamental understanding of the mechanisms of low-temperature chemistry inhibition.

Acknowledgements

This chapter, in part, is a reprint of the material as it appears in *Proceedings of the Combustion Institute* 39 (2023). Experimental and computational investigation of the influence of iso-butanol on autoignition of n-decane and n-heptane in non-premixed flows by L. Ji, A. Cuoci, A. Frassoldati, M. Mehl, T. Avedisian, K. Seshadri. The dissertation author was the primary investigator and author of this paper.

Chapter 2

Experimental and Computational Investigation of the Influence of Ethanol on Autoignition of n-Heptane in Non-Premixed Flows

2.1 Introduction

Amid rising environmental concerns, there's a growing interest in alternative fuels, with ethanol emerging as a particularly promising candidate to supplement or even replace oil-based fuels. Ethanol blends easily with hydrocarbons, and mixtures like E85, which contains 85% ethanol and 15% gasoline, are commercially available across the Americas and Europe. [54]

Schifter et al. explored the impact of using gasoline-ethanol mid-level blends (0–20% ethanol) on engine performance. For 20% blends, the reduction in fuel consumption was less than expected based on the energy content reduction in the gasoline, suggesting enhanced combustion efficiency. [55]

Additionally, Lavadera et al. determined the post-flame NO mole fractions and adiabatic laminar burning velocities for neat and blended ethanol and *n*-heptane premixed flames using a heat flux burner and laser-induced fluorescence. These studies indicated that adding ethanol to n-heptane increases the laminar burning velocity, despite not directly proportional to the ethanol content, and decreases NO formation[56]

Although ethanol is widely recognized for enhancing the performance of hydrocarbon fuels and reducing nitrogen oxide emissions, the precise chemical interactions of ethanol with the low-temperature oxidation chemistry of alkanes, especially under diffusion flame conditions, are not well understood. Therefore, a detailed investigation into the interactions between ethanol and other alkanes is essential.

Heptane, used as one of the two primary reference fuels for octane rating in gasoline with an octane number of 0[57], also serves as a surrogate for the n-alkanes in diesel fuels [58] .Given its susceptibility to pre-ignition (knocking) in engines, blending *n*-heptane with ethanol can increase its octane number, thereby enhancing its anti-knocking properties. In this chapter, *n*-heptane is selected to elucidate the influence of ethanol on it, particularly focusing on its low-temperature oxidation chemistry through detailed experiments and simulations.

In previous chapter, we carried out an experimental and computational investigation, employing the counterflow configuration, to elucidate the influence of *iso*-butanol on critical conditions of autoignition of *n*-decane and *n*-heptane. The temperature of the air stream at autoignition, T_{ig}, was measured at various values of the strain rate. Kinetic modeling was carried out using the San Diego mechanism. Critical conditions of autoignition were predicted and compared with the measurements. Low-temperature chemistry was found to play a significant role in promoting autoignition of *n*-decane and *n*-heptane. Experimental data and numerical simulations showed that addition of even small amounts of *iso*-butanol to *n*-decane or *n*-heptane increased the value of T_{ig} at low strain rates, indicating that *iso*-butanol strongly inhibits the low-temperature chemistry of *n*-decane and *n*-heptane. Predicted flame structures showed that the peak values of mole fraction of ketohydroperoxide were significantly reduced when *iso*-butanol was added to *n*-decane, indicating that the kinetic pathway to low temperature ignition is blocked. This observation was confirmed by sensitivity analysis [59].

However, investigation in the previous chapter [59] did not identify the steps specific to the kinetic model for alcohol combustion that are responsible for inhibiting low-temperature chemistry of *n*-decane and *n*-heptane. Additionally, the well-mixed model employed in the

previous analyses has a potential issue that may result in the over-prediction of liquid components with high vapor pressures.

In this chapter, both experimental and computational investigations are conducted to assess the impact of adding ethanol (C_2H_5OH) on the autoignitionof *n*-heptane (C_7H_{16}) using the counterflow configuration with condensed fuels. Critical conditions for autoignition are determined as a function of strain rate across various fuel mixture ratios. The computations utilize the San Diego mechanism [60] with the results compared against experimental measurements.

Notably, an enhanced liquid pool model is adopted for the multi-component mixture, accounting for both convective and diffusive transport within the liquid pool. A primary objective of this investigation is to identify specific kinetic steps in the combustion of ethanol that influence the low-temperature chemistry of *n*-heptane, a goal that has not been achieved in previous investigations.

2.2 Experiments and Numerical Simulations

2.2.1 Experimental Apparatus and Procedures

The experimental apparatus and procedures employed are identical to those described in Chapter 1. Additionally, we utilized a high-speed camera to capture the onset of auto-ignition.

Figure 2.1 is a high-speed photograph of the onset of autoignition. When the critical condition of autoignition is reached, a thin flame in the form of a disc first appears around the axis of symmetry above the liquid pool and subsequently rapidly covers the entire pool surface.

2.2.2 Numerical Model

The computations are performed using Cantera [61] C++ interface. The counterflow flame has been built with modified boundary conditions for liquid-gas interface of liquid-pool [1].

[1] https://github.com/LJ1356/cantera.git

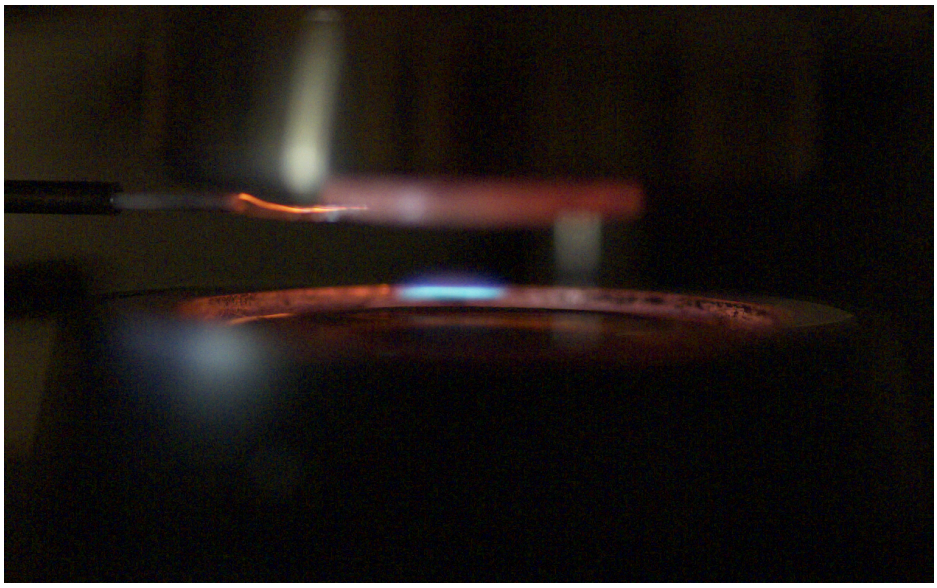

Figure 2.1: High-speed photograph of the onset of autoignition at strain rate $a_2 = 100\,\mathrm{s}^{-1}$. The fuel is 50 % *n*-heptane/50 % *n*-heptane. The photo shows the rims of the fuel-cup and the oxidizer-duct, and the thermocouple employed to measure the autoignition temperature of the oxidizer stream.

Mix-average transport model is applied in reactive flowfield to obtained steady-state solutions. At the oxidizer boundary, the injection velocity V_2, the temperature, T_2, and the value of $Y_{\mathrm{O}_2,2}$ are specified. At the fuel side, Eq. (2.1) shows the boundary conditions for species conservation and energy conservation that are applied at the liquid-gas interface. There are 5 equations included in Eq. (2.1). Eq. (2.1) is improved from Equations (1.3)-(1.6) in Chapter 1.

$$\begin{aligned}
&\dot{m}Y_{i,s} + j_{i,s} = 0 \\
&\dot{m}Y_{j,s} + j_{j,s} = \dot{m}Y_{j,l,in} \\
&[\lambda\,(dT/dy)]_{\mathrm{s}} - \dot{m}\textstyle\sum_j Y_{j,l}h_{j,l,out} = 0 \\
&P_{v,j}X_{j,l,out} - pX_{j,s} = 0 \\
&\textstyle\sum_j X_{j,l,out} - 1 = 0
\end{aligned} \tag{2.1}$$

In Eq. (2.1), subscripts i and j, respectively, refer to non-evaporating and evaporating species (specifically components from the liquid fuel). The subscripts s and l, respectively, refer to gas phase and liquid phase. Unlikely the well-mixed model employed in Chapter 1, in this

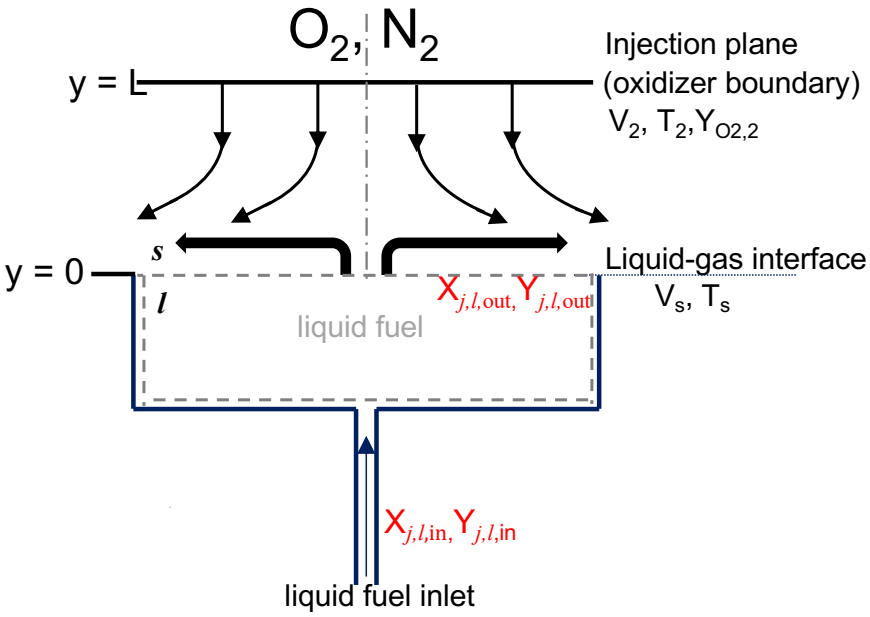

Figure 2.2: Schematic illustration of the advanced counterflow configuration. V_2 and V_s are the velocities at the oxidizer boundary and on the gas side of the liquid-gas interface, respectively. T_2 and T_s are the temperatures at the oxidizer boundary and the liquid-gas interface, respectively, and $Y_{O_2,2}$ is the mass fraction of oxygen at the oxidizer boundary.

model, we did not assume the same mass fraction between inlet and outlet liquid pool. Instead, the convective and diffusive transport within the liquid pool is considered. Therefore, inlet and outlet of liquid pool are required to be separately calculated in boundary conditions.

We considered the liquid phase mixtures as a control volume. Here, subscripts *in* and *out* refer to the inlet and outlet of this control volume, respectively. $Y_{j,l,out}$, $X_{j,l,out}$ are mass and mole fraction at the outlet of liquid pool, corresponding to the liquid side of liquid-gas interface. Meanwhile, $Y_{j,l,in}$, $X_{j,l,in}$ denote the mass fractions at the inlet of liquid pool, which is controlled by syringe pump during the experiment.

$\dot{m}$ is the mass evaporation rate, $Y_{i,s}$, and $j_{i,s}$ the mass fraction and diffusive flux of the non-evaporating species, $Y_{j,s}$, $X_{j,s}$ and $j_{j,s}$ the mass fraction, mole fraction and diffusive flux of the evaporating species on the gas side of the interface, λ is the thermal conductivity of the gas, and $h_{j,l,in}$, and $P_{v,j}$, respectively, are the heat of vaporization and vapor pressure of component

j on the liquid-side of liquid-gas interface and p the total pressure. The total mass flux of all species, i, on the gas-side of the liquid-gas interface comprises the diffusive flux, $j_{i,s}$, and the convective flux $\dot{m}Y_{i,s}$.

The saturation vapor, $P_{\mathrm{v,j}}$ and the heat of vaporization $h_{j,l}$ in Eq. (2.1) for any species j are evaluated using the expressions $\log_{10} P_{v,j} = A_{1,j} + B_j/T + C_j \times \log_{10}(T) + D_j \times T + F_j \times T^2$, and $h_{j,l} = A_{2,j}\left(1 - T/T_{j,cr}\right)^{N_j}$, where the value for the critical temperature $T_{j,cr}$ and the values for the empirical coefficients $A_{1,j}, B_j, C_j, D_j, F_j, A_{2,j}$ and N_j are obtained from [62].

The first expression in Eq. (2.1) imposes the condition that the total mass flux for all species, except for those of the evaporating fuel components, vanishes at the liquid-gas interface. This equation aligns with Eq. (1.3).

The second expression of Eq. (2.1) enforces the balance that the outgoing mass flux of each evaporating component from the liquid-gas interface must be equal to the corresponding incoming mass flux of liquid pool, specifically the product of $\dot{m}$ and the mass fraction of the species at liquid pool inlet, $Y_{j,l.in}$. While it provides a similar mass flux constraint for evaporated species as previous model, this equation differs from Eq. (1.4) by emphasizing the conservation of mass flux for each individual component rather than the sum of mass flux inflow liquid pool. This adjustment is critical for preventing the overestimation of species with higher vapor pressure. In previous model, even though the total mass flux is maintained, the mass flux or mass fraction of each component mainly dependent on their vapor pressures, as associated in the Eq. (1.6). The conservation of individual component mass flux is not applied in previous model.

The third expression in Eq. (2.1) addresses energy balance at the liquid-gas interface. It equates the product between the average vaporization enthalpy at the outlet of liquid pool and mass evaporation rate with the heat conduction in the gas side of liquid-gas interface. It is assumed that, in the center of counterflow flame, only heat conduction plays a predominantly part in heat transfer.

The fourth expression in Eq. (2.1) is Raoult's law relating the mole-fraction of the evaporating species on the gas side to the corresponding mole-fraction in the outlet of liquid

pool. The fifth expression in Eq. (2.1) ensures the mass conservation at the outlet of liquid pool. Its inclusion is crucial for rendering this set of equations solvable.

Notably, Eq. (2.1) remains effectively for modeling scenarios involving multi-components in the liquid pool, without requiring any modifications. Moreover, if the liquid pool only contains single species, this group of equations will be automatically simplified to the model employed for single fuel liquid pool [63]. In this simplification, the fifth equation in Eq. (2.1) become redundant and is omitted.

Eq. (2.1) has been implemented by C++ interface of Cantera. New class of boundary has been established to accommodate this model. For further details about the liquid pool, please refer to the files named *Phase_liquid* at https://github.com/LJ1356/cantera.git. With the implementation of the new boundary condition for the liquid pool, a counterflow flame configuration has been established. This setup has enabled the determination of critical conditions for auto-ignition across various fuels and strain rates.

The fuels tested are *n*-heptane (HPLC grade, purity $\geq$ 99 %), ethanol and mixtures with volumetric composition of 20% *n*-heptane/80% ethanol, 50% *n*-heptane/50% ethanol, and 80% *n*-heptane/20% ethanol. The oxidizer is air.

2.2.3 Chemical Mechanism

Kinetic modeling is carried out using the San Diego mechanism [60]. Figure 2.3 illustrates the low-temperature oxidation chemistry of *n*-heptane. At low temperatures, the n-heptyl radicals ($R_7\cdot$) react with molecular oxygen and form the corresponding peroxy-heptyl radicals ($R_7OO\cdot$). These radicals subsequently undergo isomerization to hydroperoxy-heptyl radical($\cdot Q_7OOH$) by internal hydrogen transfer. Following this, a second oxygen addition leads to formation if peroxy-heptylhydroperoxy $\cdot OQ_7OOH$ radicals, which then isomerize and decompose into carbonyl-hydro-peroxides (CHPs) and OH. The very low O-O bond energy of the hydroperoxy function makes CHPs key radicals in the low-temperature chain-branching reactions [26].

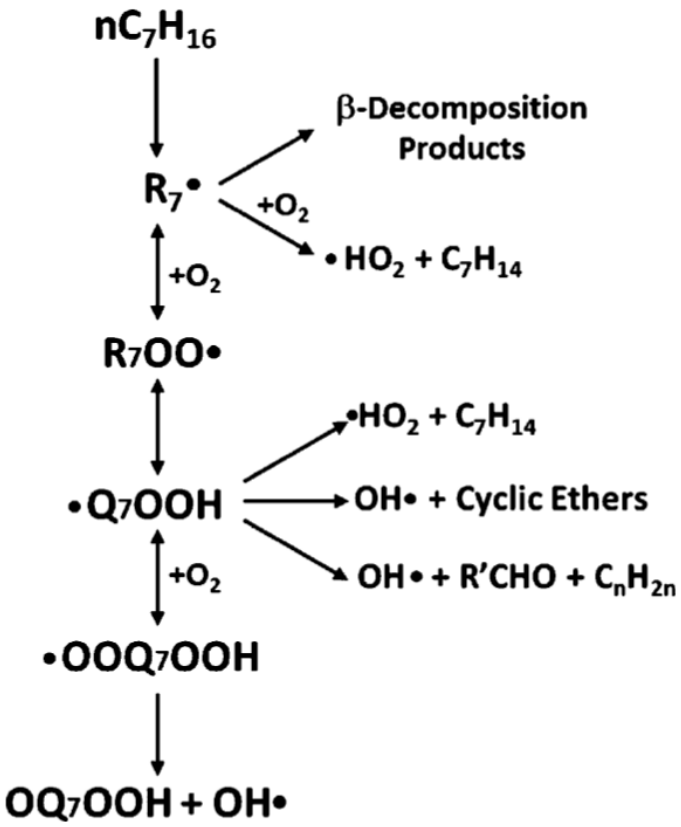

Figure 2.3: Simplified low temperature oxidation chemistry of *n*-heptane[26].

2.3 Results and Discussion

Figure 2.4 shows the temperature of the air at autoignition, T_{ig}, as a function of strain-rate, a_2, for *n*-heptane, ethanol and mixtures of these fuels. In this figure, the symbols represent experimental data and the lines are predictions. At low strain rates, around $a_2 = 95\,\mathrm{s}^{-1}$, measurements show that *n*-heptane is easiest to ignite because it has the lowest value of T_{ig} and the value of T_{ig} increases in the order, ethanol, 20% *n*-heptane/80% ethanol, 50% *n*-heptane/50% ethanol, and 80% *n*-heptane/20%ethanol. It is noteworthy that at low strain rates, all mixtures have higher values of T_{ig} than the components of the mixture. At low strain rates computations show a similar trend where *n*-heptane is easiest to ignite followed by ethanol and 80% *n*-heptane/20%ethanol that have nearly the same value of T_{ig}, while the mixtures 20% *n*-heptane/80% ethanol, and 50% *n*-

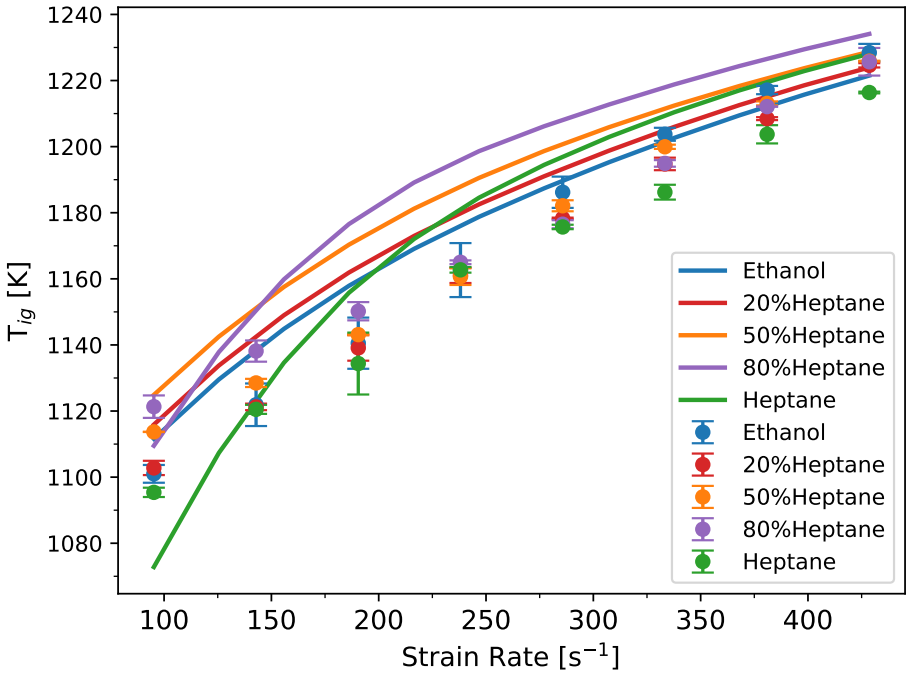

Figure 2.4: The temperature of the air at autoignition, T_{ig}, of *n*-heptane, ethanol and mixtures of *n*-heptane and ethanol by volume as a function of strain-rate, a_2. The symbols represent experimental data and the lines are predictions. The uncertainty in experimental data is $\pm$ 10 K.

heptane/50% ethanol have values of T_{ig} that are higher than those for *n*-heptane and ethanol. Moreover, experimental data and predictions show that at low strain rates addition of a small amount (20 %) of ethanol increases T_{ig} by a significant amount from that for *n*-heptane, indicating that addition of ethanol strongly inhibits the LTC of *n*-heptane. This behavior is similar to that observed in a previous investigation where *iso*-butanol was found to inhibit LTC of *n*-heptane and *n*-decane [59]. Figure 2.4 shows that at high strain rates the measured value of T_{ig} for *n*-heptane is the lowest and T_{ig} for the mixtures are nearly the same as that for ethanol and the differences are well within experimental uncertainties. At high strain rates the predictions show that T_{ig} for ethanol is the lowest followed by 20% *n*-heptane/80% ethanol, 50% *n*-heptane/50% ethanol, *n*-heptane and 80% *n*-heptane/20%ethanol. Thus, the order of increase in values of T_{ig} in the experiment and predictions do not match at high strain rates. In general, at low strain rate, the quantitative agreement between the measurements and predictions are within experimental

uncertainty. The deviations can also arise from uncertainties in the kinetic model for ethanol and requires further investigation.

Following previous investigation where *iso*-butanol was found to inhibit LTC of *n*-heptane and *n*-decane [59], computations were carried out with the complete mechanism and with the LTC reactions of *n*-heptane removed from the kinetic model and the results are shown in Fig. 2.5.

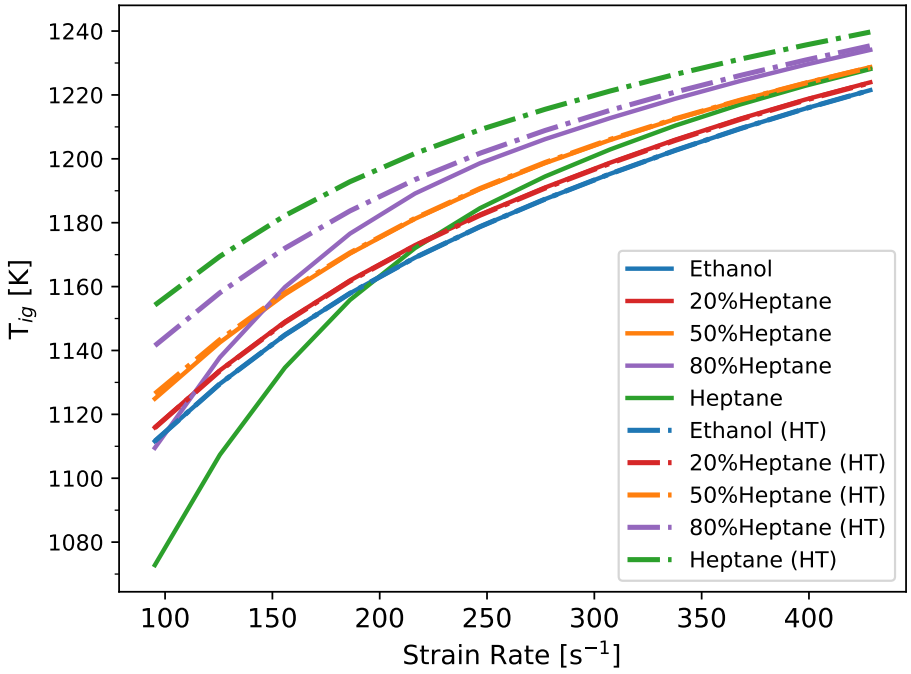

Figure 2.5: The predicted temperature of the air at autoignition, T_{ig}, of *n*-heptane, ethanol and mixtures of *n*-heptane/ethanol with percent volume ratios of 80/20, 50/50, and 20/80, as a function of strain-rate, a_2. The figure shows predictions with the complete kinetic mechanism and those with low-temperature chemistry removed (HT).

For *n*-heptane, at low strain rates, the value of T_{ig} calculated excluding LTC is significantly higher than that predicted using complete kinetic model. This discrepancy diminishes as the strain rate increases, however the deviation remains when a_2 reaches 450 s^{-1}. It suggests that the LTC is still active under high strain rates, which is different from CRECK mechanism for *n*-decane. Thus, further investigation of the San Diego mechanism is warranted to explain this difference.

For the mixture with 80% *n*-heptane/20%ethanol T_{ig} calculated without LTC is higher than that calculated using the complete model, but the differences are not as large as those for *n*-heptane. This suggests that while the addition of ethanol does influence the LTC, it does not completely inhibit it. Therefore, some effects of LTC on auto-ignition are still evident in this mixture. The reasons could be that the ethanol concentrations are not sufficiently high to fully suppress the LTC, or the LTC within the San Diego mechanism is too strong to be inhibited under the same conditions when compared with other chemical mechanisms.

It is noteworthy that for the mixtures 20% *n*-heptane/80% ethanol and 50% *n*-heptane/50% ethanol the values of T_{ig} calculated with and without LTC are nearly the same, indicating that ethanol has entirely inhibited the LTC of *n*-heptane for these mixtures. It is confirmed that 20% additional ethanol is insufficient to entirely suppress LTC of *n*-heptane which exhibits stronger influence in San Diego mechanism.

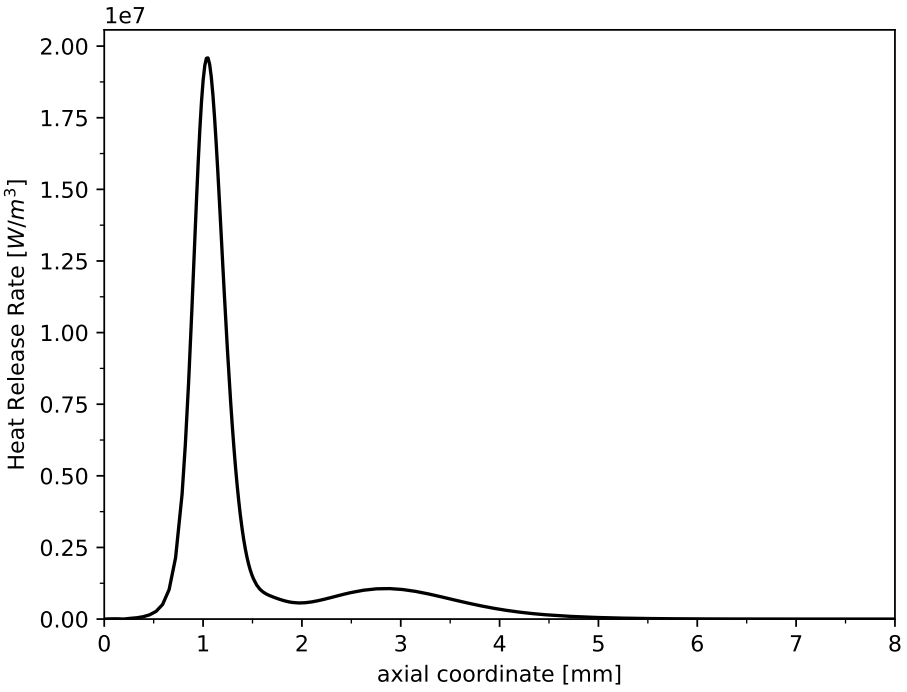

Figure 2.6: Predicted profile of heat release for *n*-heptane. Oxidizer temperature, $T_2 = 1040\,\mathrm{K}$, strain rate $a_2 = 95\,\mathrm{s}^{-1}$.

Figures 2.6, 2.7, and 2.8 respectively, show predicted profiles of heat release rate, main

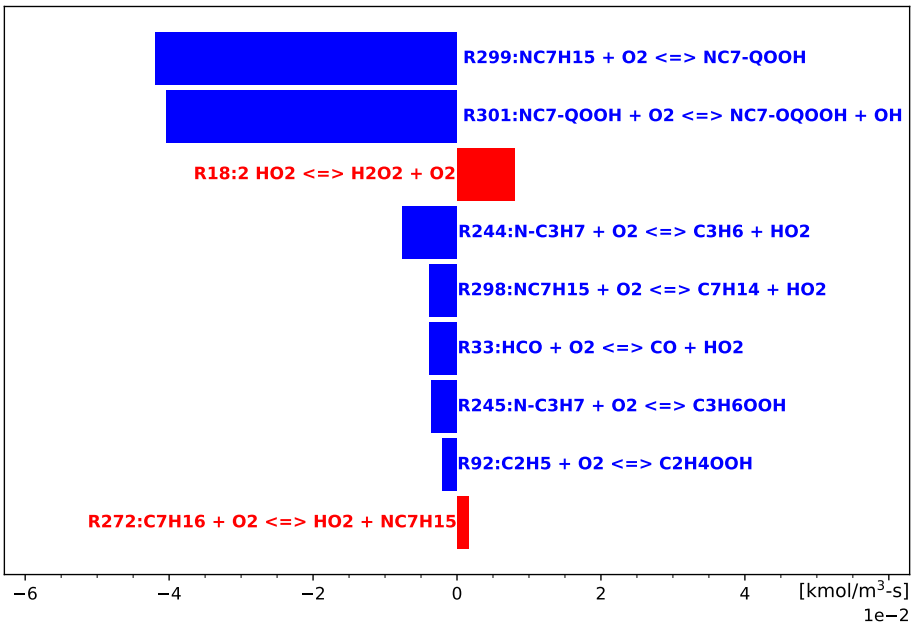

Figure 2.7: Key elementary steps that consume oxygen for *n*-heptane at the location of maximum heat release indicated in Fig. 2.6 (y = 1.07 mm). Oxidizer temperature, $T_2 = 1040\,\mathrm{K}$, strain rate $a_2 = 95\,\mathrm{s}^{-1}$. Blue represents consumption and red formation.

elementary steps that consume oxygen, and the main elementary steps that contribute to the rise in temperature, for pure *n*-heptane at low strain rate, $a_2 = 95\,\mathrm{s}^{-1}$ and $T_2 = 1040\,\mathrm{K}$.

The liquid gas interface is at the axial location, $y = 0$ and the exit of the duct at $y = 10.5\,\mathrm{mm}$. Figure 2.6 illustrates that the heat release profile features two distinct peaks: one around $y \approx 1\,\mathrm{mm}$ and the other around $y \approx 3\,\mathrm{mm}$. The first peak, where LTC is expected to take place, is significantly higher than the second peak, where high temperature chemistry is expected to take place. As oxidizer temperature increases, the second peak increases until auto-ignition occurs. Auto-ignition is directly influenced by the second peak in Figure 2.6. The first and the second peaks are referred to low-temperature heat release peak and high-temperature heat release peak, respectively.

Figures 2.7 shows the reactions that consumed oxygen near the low-temperature heat release peak where LTC is highly activated. It reveals that O_2 is consumed primarily by the low-temperature reactions of, *n*-heptane, specifically, through R299: n-C_7H_{15} + O_2 $\Longleftrightarrow$ n-C_7QOOH

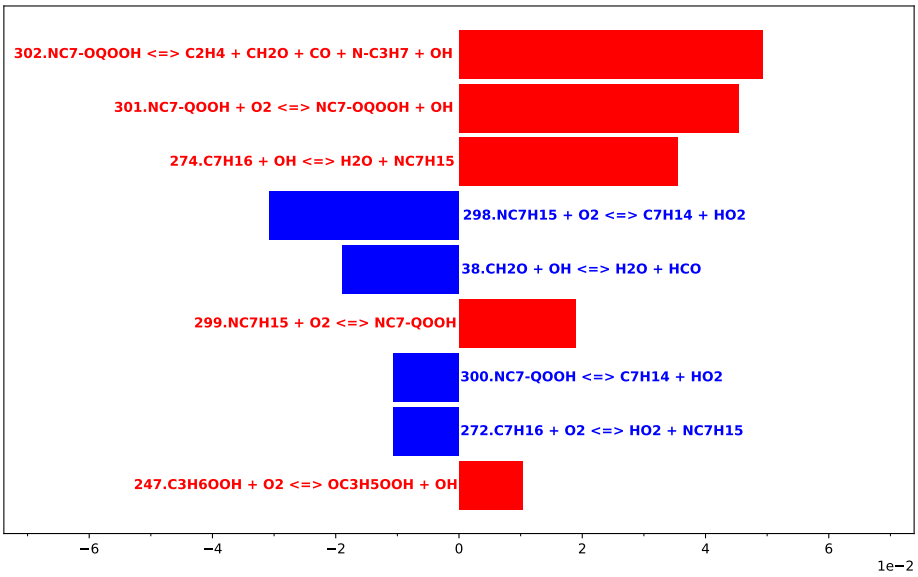

Figure 2.8: Key elementary steps that contribute to the rise of temperature for *n*-heptane at the location of maximum heat release indicated in Fig. 2.6 (y = 1.07 mm). Oxidizer temperature, $T_2 = 1040\,\mathrm{K}$, strain rate $a_2 = 95\,\mathrm{s}^{-1}$. Blue represents reactions that decrease temperature and red reactions that increase temperature

and R301: n-C_7QOOH + O_2 $\Longleftrightarrow$ n-C_7OQOOH +OH. These reactions correspond to the two oxygen addition steps in the LTC of *n*-heptane.

Fig. 2.8 shows sensitivity of reaction constant to temperature near the low-temperature heat release peak. It indicates that temperature rise at this peak is primarily due to low-temperature kinetic steps, R299, R301 and R302.

Fig. 2.9 illustrates the sensitivity of temperature analysis results at the high-temperature heat release peak. The dominant reactions are similar to those shown in Fig. 2.8. Two oxygen addition steps, R301 and R302, play significant positive roles in the temperature increase at this location. Given that the auto-ignition is directly affected by high-temperature heat release peak, it suggests for *n*-heptane, at low strain rates autoignition, is promoted by LTC.

Figure 2.10 shows predicted profile of heat release at low strain rate, $a_2 = 95\,\mathrm{s}^{-1}$ and $T_2 = 1040\,K$. Unlike the heat release profile for *n*-heptane, shown in Figure 2.6, which features two distinct peaks, the heat release profile for ethanol shows only one single peak around 3 mm. This observation is consistent with the widely accepted point of view that unlike *n*-heptane,

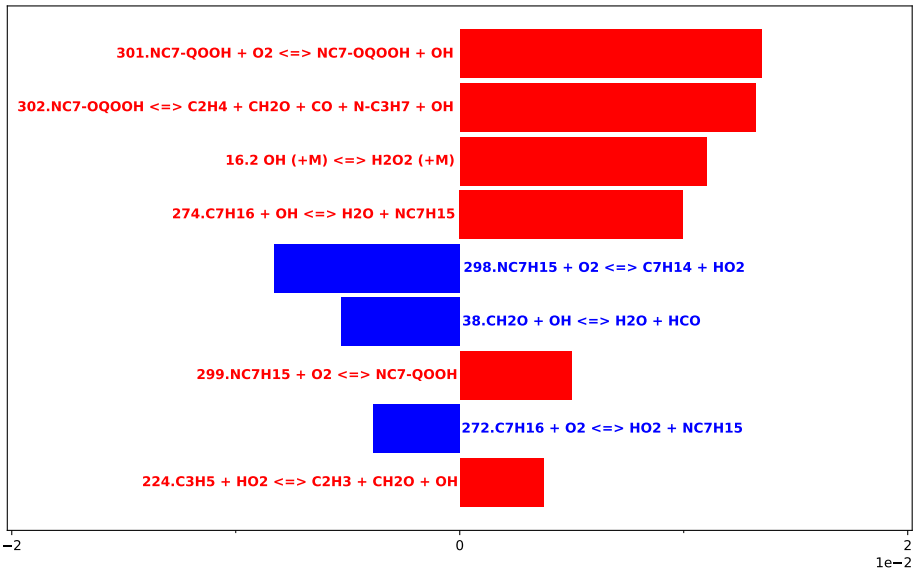

Figure 2.9: Key elementary steps that contribute to the rise of temperature for *n*-heptane at the location of maximum heat release indicated in Fig. 2.6 (y = 2.89 mm). Oxidizer temperature, $T_2 = 1040\,\mathrm{K}$, strain rate $a_2 = 95\,\mathrm{s}^{-1}$. Blue represents reactions that decrease temperature and red reactions that increase temperature

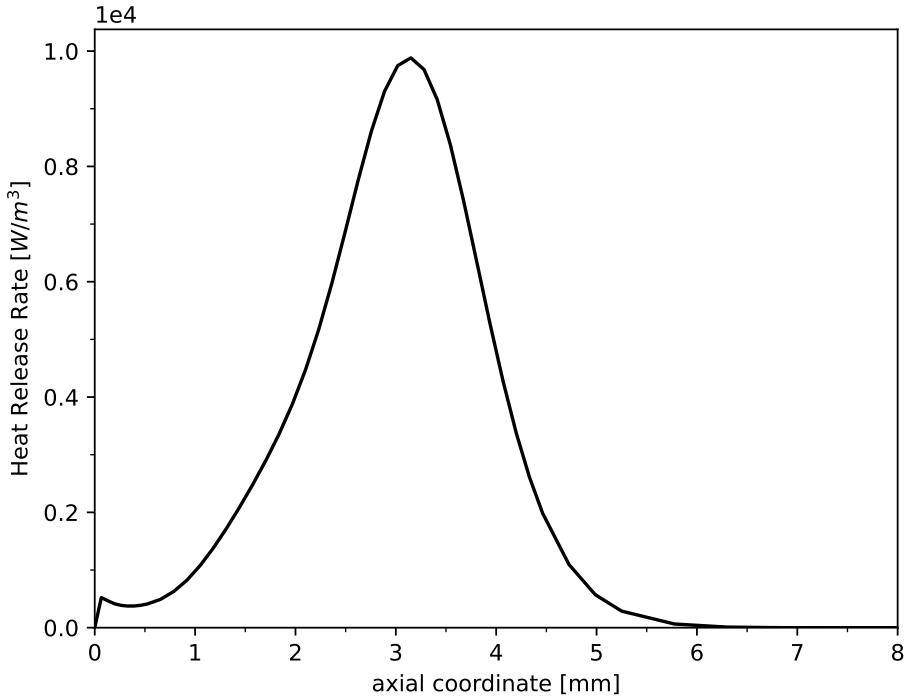

Figure 2.10: Predicted profile of heat release for ethanol. Oxidizer temperature, $T_2 = 1040\,\mathrm{K}$, strain rate $a_2 = 95\,\mathrm{s}^{-1}$.

ethanol does not exhibit separate low-temperature and high-temperature chemistry.

Figures 2.11, 2.12, and 2.13, respectively, show the profile of heat release rate, main elementary steps that consume oxygen, and the main elementary steps that contribute to the rise in temperature for mixtures with volumetric composition of 50% *n*-heptane/50% ethanol. The oxidizer temperature, $T_2 = 1040\,\mathrm{K}$ and strain rate $a_2 = 95\,\mathrm{s}^{-1}$.

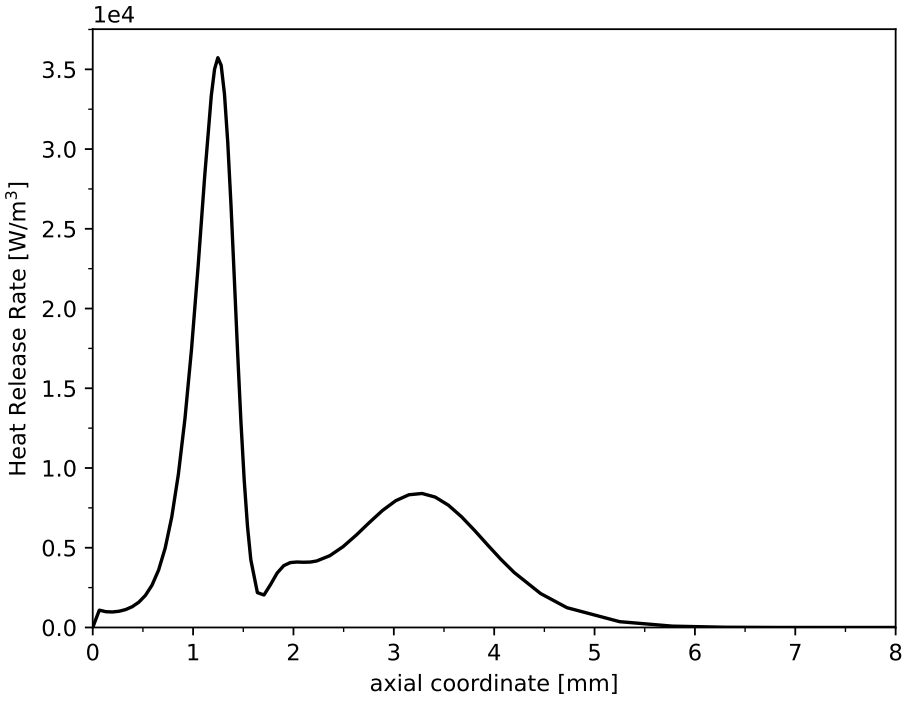

Figure 2.11: Predicted profile of heat release for mixtures with volumetric composition of 50% *n*-heptane/50% ethanol. Oxidizer temperature, $T_2 = 1040\,\mathrm{K}$, strain rate $a_2 = 95\,\mathrm{s}^{-1}$.

The heat release profile in Fig. 2.11 shows two peaks at approximately the same locations as those in Fig. 2.6. However, the low-temperature heat release peak near the liquid-gas interface in Figure 2.11, where low-temperature reactions are expected, is significantly lower, at around $3.5 \times 10^4\,\mathrm{W/m^3}$. This is substantially less than the peak in Figure 2.6, which reaches about $1.9 \times 10^7\,\mathrm{W/m^3}$. Given that the oxidizer temperatures are the same for both fuel scenarios, the reduction in the low-temperature heat release peak is primarily due to the inhibited effects of ethanol.

Figure 2.12 highlights the key steps consuming O_2, which include R195:O_2 + CH_3CHOH

$\Longleftrightarrow$ HO_2 + CH_3CHO R299:n-C_7H_{15} + O_2 $\Longleftrightarrow$ n-C_7QOOH and R301:n-C_7QOOH + O_2 $\Longleftrightarrow$ n-C_7OQOOH +OH. R299 and R301 are involved in the LTC of *n*-heptane, while R195, which involves ethanol, is another significant oxygen-consuming step. It is considered that there is a competition between LTC of *n*-heptane and ethanol for oxygen. Specifically, this competition involves species n-C_7H_{15}, n-C_7QOOH and CH_3CHOH.

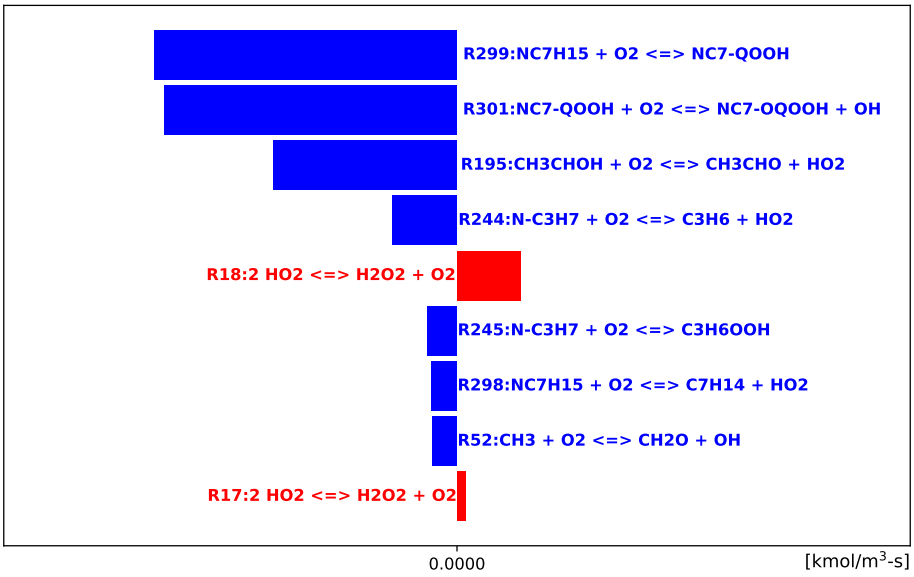

Figure 2.12: Key elementary steps that consume oxygen for mixtures with volumetric composition of 50% *n*-heptane/50% ethanol at the location of maximum heat release indicated in Fig. 2.11 (y = 1.25 mm). Oxidizer temperature, $T_2 = 1040$ K, strain rate $a_2 = 95\ s^{-1}$. Blue represents consumption and red formation

Figure 2.13 illustrates that the temperature rise is sensitive to several key reactions. These include R274: C_7H_{16} + OH $\Longleftrightarrow$ H_2O + n-C_7H_{15} and R275: C_7H_{16} + HO_2 $\Longleftrightarrow$ H_2O_2 + n-C_7H_{15}, which contribute to the generation of n-heptyl radicals; R172: C_2H_5OH + OH $\Longleftrightarrow$ CH_3CHOH + H_2O, involving the breakdown of ethanol.

The inclusion of reaction R172 marks a difference from the kinetics steps observed in Fig. 2.8, where the temperature rise was primarily attributed to the reactions related to LTC of *n*-heptane. The product of R172, CH_3CHOH, plays an important role in the competition for oxygen with nC_7H_{15}, which is the product from R274 and R275.

Figure 2.14 shows the temperature sensitivity coefficient of various reactions. Notably,

R172 and R173, which are related to ethanol, play more dominant roles than R274, R275, and R302, which are associated with the low-temperature chemistry (LTC) of *n*-heptane. It indicates the autoignition for this mixture is influenced by both ethanol-related reactions and the LTC of *n*-heptane, highlighting an existing competition for oxygen between ethanol and *n*-heptane, as depicted in Figure 2.14.

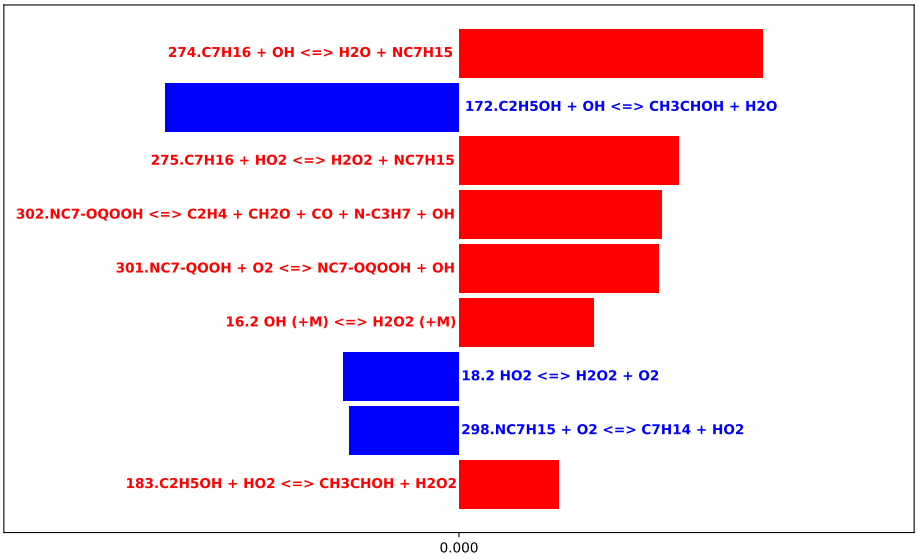

Figure 2.13: Key elementary steps that contribute to the rise of temperature for mixtures with volumetric composition of 50% *n*-heptane/50% ethanol at the location of maximum heat release indicated in Fig. 2.11 (y = 1.25 mm). Blue represents reactions that decrease temperature and red reactions that increase temperature.

The *n*-heptane become the n-heptyl radicals after H abstraction is converted into n-heptyl radicals via hydrogen abstraction, such as R274 and R275. Simultaneously, ethanol is transformed into CH_3CHOH through similar hydrogen abstraction, notably via reaction R172. These active radicals, n-heptyl radicals and CH_3CHOH, then participate in reactions with O_2, specifically through R299 for n-heptyl radicals and R195 for CH_3CHOH. Furthermore, the product of R299, nC_7-QOOH, also engages in reactions with oxygen. The oxygen consumption by these reactions suggests a potential competition among them.

Besides, there is another possible competition for hydroxyl radical OH between ethanol and *n*-heptane, by reactions R274 (involving *n*-heptane) and R172 (involving ethanol). This

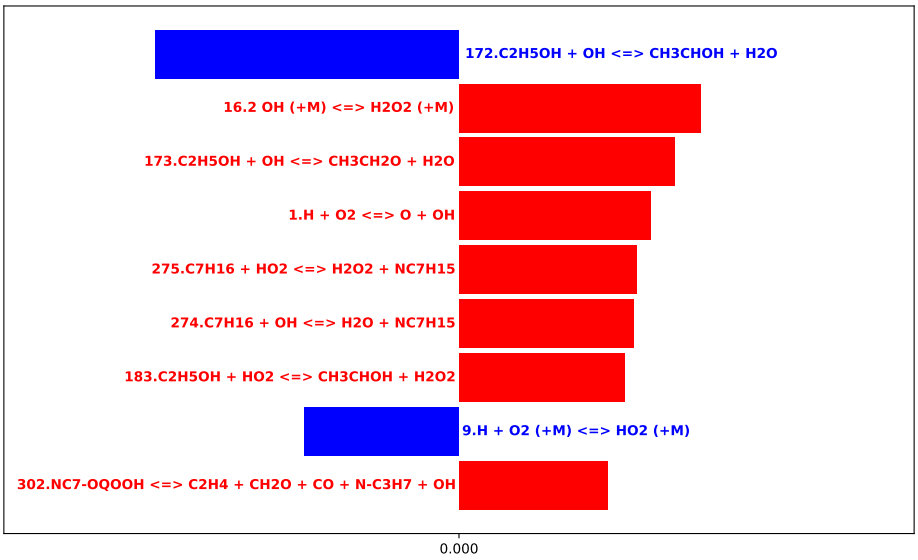

Figure 2.14: Key elementary steps that contribute to the rise of temperature for mixtures with volumetric composition of 50% *n*-heptane/50% ethanol at the location of the second heat release peak indicated in Fig. 2.11 (y = 3.28 mm). Blue represents reactions that decrease temperature and red reactions that increase temperature.

introduces another possible layer of complexity to the chemical interactions within the system.

To investigate whether competition between kinetic steps that consume O_2 in the mechanisms of *n*-heptane and ethanol are responsible for inhibition of autoignition at low strain rates, computations were performed with the step R195: $O_2 + CH_3CHOH \Longleftrightarrow HO_2 + CH_3CHO$ removed from the kinetic model. Given that the *n*-heptane mechanism features relatively independent low-temperature and high-temperature oxidation chemistry, removing the low-temperature chemistry (LTC) of *n*-heptane allows for a clearer observation of ethanol's suppression effects on auto-ignition temperatures. However, the ethanol mechanism involves several coupled reactions; thus, the removal of a single reaction can lead to complex effects on the auto-ignition temperature. It is more straightforward to observe the restoration of low-temperature heat release peak to examine the influence of removing oxidation competition step.

Figures 2.15 show profiles of heat release rate comparing the effects of removing reactions associated with O_2 and OH competition. The oxygen competition is predominantly driven by reaction R195: $O_2 + CH_3CHOH \Longleftrightarrow HO_2 + CH_3CHO$, while OH competition is primarily

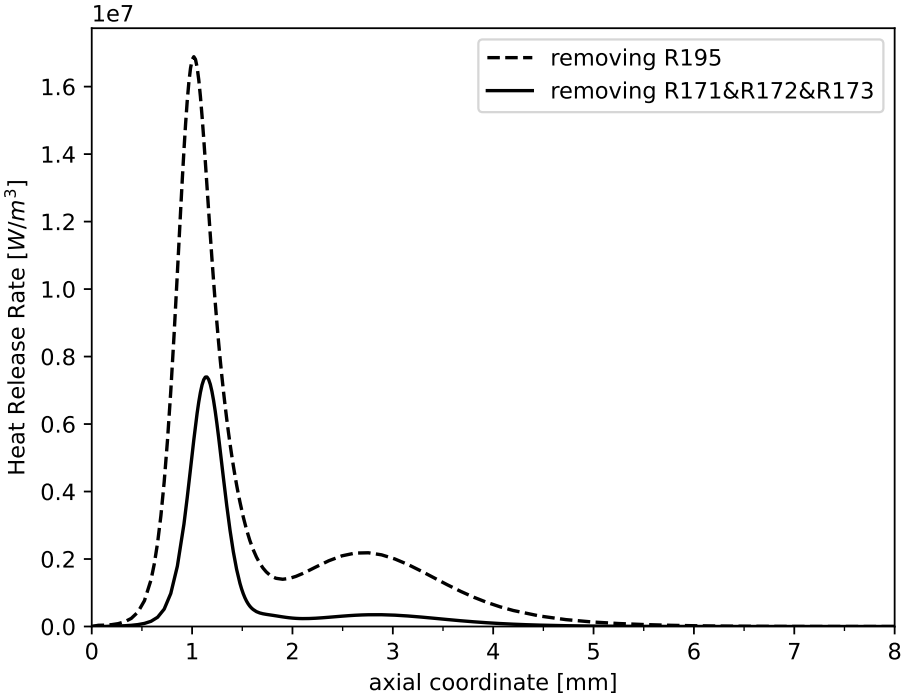

Figure 2.15: Predicted profile of heat release for mixtures with volumetric composition of 50% *n*-heptane/50% ethanol with removal of R195, compared with removals of R171, R172, R173 and oxidizer temperature, $T_2 = 1040\,\mathrm{K}$, strain rate $a_2 = 95\,\mathrm{s}^{-1}$.

influenced by reactions R171, R172, and R173.

Comparing the profile in of Fig. 2.15 with that in Fig. 2.11, removal of the oxygen competition restores the low-temperature heat release peak from $3.6 \times 10^4\,\mathrm{W/m^3}$ to approximately $1.7 \times 10^7\,\mathrm{W/m^3}$, which is close to the peak observed in pure *n*-heptane, in Figure 2.6, at $1.9 \times 10^7\,\mathrm{W/m^3}$. In contrast, removing OH competition only partially increases the low-temperature heat release peak, indicating that while some of the suppression from ethanol is reduced, other competitive interactions involving different radicals persist after the removal of OH competition.

The product of R172, CH_3CHOH, reacts with O_2 via R195. Removing R172 interrupts the main pathway for producing CH_3CHOH. However, alternative pathways that continue to produce CH_3CHOH remain active, continuing to compete for oxygen with *n*-heptane. Therefore, directly removing reactions involved in oxygen competition is the most effective method to

eliminate the inhibitory effects of ethanol. This indicates that LTC of *n*-heptane is affected by oxygen competition, rather than OH competition in San Diego mechanism.

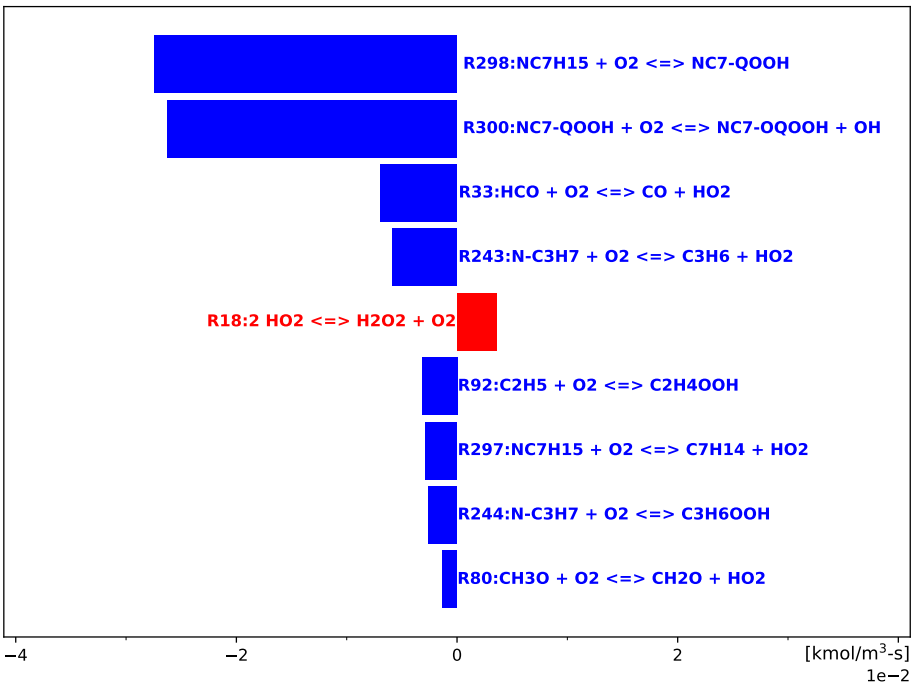

Figure 2.16: Key elementary steps that consume oxygen for mixtures with volumetric composition of 50% *n*-heptane/50% ethanol at the location of maximum heat release indicated in Fig. 2.15 (y = 1.1 mm) with step O_2 + $CH_3CHOH \Longleftrightarrow HO_2$ + CH_3CHO removed and oxidizer temperature, $T_2 = 1040$ K, strain rate $a_2 = 95\ s^{-1}$. Blue represents consumption and red formation

Figures 2.16, and 2.17, respectively, show profiles of main elementary steps that consume oxygen, and the main elementary steps that contribute to the rise in temperature predicted at conditions close to autoignition for mixtures with volumetric composition of 50% *n*-heptane/50% ethanol with step O_2 + $CH_3CHOH \Longleftrightarrow HO_2$ + CH_3CHO removed with $T_2 = 1040$ K, strain rate $a_2 = 95\ s^{-1}$. It should be noted that the order numbers of reactions in these figures differ from those in the original mechanism, as the removal of reactions alters the total number of reactions within the mechanism.

Figure 2.12 shows that O_2 is primarily consumed in the step O_2 + $CH_3CHOH \Longleftrightarrow HO_2$ + CH_3CHO and low-temperature steps. Additionally, Fig. 2.16 shows that O_2 is still consumed by the low-temperature steps of *n*-heptane. Moreover, Fig. 2.14 shows that the temperature rise in

the reaction zone is primarily from high temperature chemistry and ethanol-related steps, while dominant reactions shown in Fig. 2.17, includes the low-temperature reactions of *n*-heptane, specifically n-C_7H_{15} + O_2 $\Longleftrightarrow$ n-C_7QOOH, which plays an important role in controlling the rise of temperature. These observations provide further confirmation that the step, O_2 + CH_3CHOH $\Longleftrightarrow$ HO_2 + CH_3CHO, competes with O_2 consumption by low-temperature reactions of *n*-heptane. As a consequence, the low-temperature reactions of *n*-heptane are suppressed when ethanol is added.

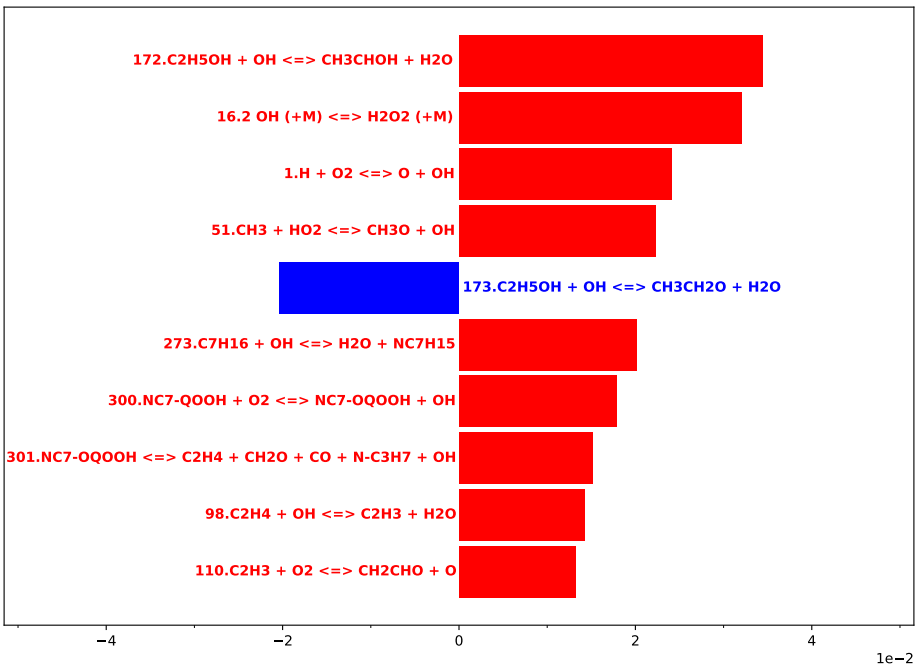

Figure 2.17: Key elementary steps that contribute to the rise of temperature for mixtures with volumetric composition of 50% *n*-heptane/50% ethanol at the location of the second heat release peak indicated in Fig. 2.15 (y = 2.76 mm) with step O_2 + CH_3CHOH $\Longleftrightarrow$ HO_2 + CH_3CHO removed and oxidizer temperature, $T_2 = 1040$ K, strain rate $a_2 = 95\ s^{-1}$. Blue represents reactions that decrease temperature and red reactions that increase temperature.

Cheng et al. [64] studied autoignition behavior of gasoline/ethanol blends in a rapid compression machine. In the low-temperature regime ethanol was found to retard first stage and main ignition delay times and suppress the rates and extents of low-temperature heat release. Qualitatively this is similar to observations reported here where addition of ethanol not only increases the autoignition temperature at low strain rates but also decreases the level of heat

release in the region where LTC is expected to take place.

2.4 Concluding Remarks

In this chapter, by isolating the low-temperature oxidation reactions of *n*-heptane and the reactions associated with ethanol, and comparing their respective influences on auto-ignition temperature and heat release profiles, it is identified the key mechanism through which ethanol addition inhibits the low-temperature autoignition process of *n*-heptane in San Diego Mechanism. Just as the heptyl radical exhibits an attractive site for addition of an oxygen molecule, so does the radical produced by H-atom abstraction from the ethanol site adjacent to the hydroxyl exhibit sufficient attraction for oxygen molecules to compete favorably with heptyl, yielding hydroperoxyl plus a stable molecule. By depriving heptyl and its isomerized oxygen-addition product (often denoted by QOOH in the literature) from a sufficient supply of oxygen molecules, the ethanol-generated radical turns off the low-temperature path in *n*-heptane, thereby increasing its auto-ignition temperature.

This same mechanism is likely to prevail for higher alcohols, as well, thereby contribution to other perhaps unexpected experimental results. Future research involving these higher alcohols, as well as different normal alkanes, would be worthwhile, to determine how generally relevant this type of new mechanism may be. Implications may be expected on autoignition behaviors of developing environment-friendly new fuels designed to mitigate detrimental climate effect.

Acknowledgements

This chapter, in part, is a reprint of the material as it appears in *Proceedings of the Combustion Institute* 40 (2024), Experimental and computational investigation of the influence of ethanol on auto-ignition of n-heptane in non-premixed flows by L. Ji, K. Seshadri, F. A. Williams. The dissertation author was the primary investigator and author of this paper.

Chapter 3

Analysis of Interactions Between Chemical Reactions, Species Transport and Heat Release in Laminar Flames

3.1 Introduction

The laminar, steady, one-dimensional counterflow diffusion flame is investigated to elucidate interaction between diffusion and chemistry[65]. Through the counterflow configuration, Seshadri [37] studied extinction of diffusion flame methanol, heptane and wood in the presence of suppressive agents such as nitrogen and water. Seiser et al. [66] elucidated the mechanisms of extinction and autoignition of n-heptane, finding that strain has greater influence on low-temperature chemistry than the temperature of the reactants. Ji et al. [59] investigated the impact of iso-butanol and ethanol on the auto-ignition of n-decane and n-heptane. It is observed that addition of iso-butanol and ethanol to n-decane or n-heptane elevated the auto-ignition temperature at low strain rates, indicating that iso-butanol and ethanol inhibits the low-temperature chemistry (LTC) of n-decane and n-heptane. These observations were further supported by sensitivity analysis.

Sensitivity analysis have been extensively employed to elucidate the influence of selected parameters on combustion, specifically, reaction rate constant. They are useful for identification and quantification of the role of selected parameters, revealing their predominant controlling

influence on changes in concentrations [67]. They play a crucial role in uncertainty analysis, estimation of parameter, and investigation or reduction of mechanism [68]. This approach is instrumental in understanding the sensitivity of the predicted outcomes or quantities of interest (QoIs) to uncertain parameters [69]. For example, sensitivity analysis facilitates quantification of the indirect influence of the rate constants of reactions in terms of temperature. However, the traditional sensitivity analysis in combustion research focuses on the systematic impact of parameters on output variables. It falls short of detailed explaining the direct influence between reactions and the output variables, nor the subsequent effects of these output variables changes on other output variables.

Another widely used method, path flux analysis (PFA) method, plays a crucial role in dissecting the production and consumption fluxes (pathways) in chemical mechanism. It is employed alongside in direct relation graph (DRG) method to identify critical species and reactions. Sun et al.[70] [71] demonstrated that the skeletal mechanisms refined by PFA exhibits enhanced accuracy compared to those derived by DRG method with the similar size in several cases. Path flux analysis could explicitly offer insight into the consumption and production of species in zero-dimensional models or single point in one-dimensional flame configuration, facilitating analysis of kinetic mechanism. However, for the counterflow flame configuration, it has difficulty in elucidating the interaction cross different spatial points.

Recently, there have been numerous studies applying deep learning to chemical ordinary differential equations (ODEs). Ji et al.[72] developed the stiff-PINN approach that utilizes QSSA to enable the PINN to solve stiff chemical kinetics. The multiscale physics-informed neural network (MPINN) approach proposed by Weng et al.[73] is based on the regular physics-informed neural network (PINN) for solving stiff chemical kinetic problems with governing equations of stiff ODEs. Su et al.[74] employed a neural ordinary differential equation (Neural ODE) framework to optimize the kinetic parameters of reaction mechanisms, showing that the proposed algorithm can optimize stiff chemical models with sufficient accuracy, efficiency, and robustness. The forward propagation in neural networks shows a kind of equivalence to chemical

ODEs. Thus, it is also possible to introduce sensitivity analysis methods for neural networks to chemical systems.

Zurada's sensitivity method, widely used in the analysis of neural networks for the reduction of training set size[75], employs calculations based on partial derivatives with respect to input variables for redundant feature selection or deletion. Inspired by Zurada's method and considering the unique characteristics of combustion chemistry alongside the governing equations of the counterflow configuration, we introduce a supplemental method. This method, grounded in the use of partial derivatives, aims to analyze the interplay across different temperature zones in counterflow flames. It is employed to provide a detailed explanation of the interactions between n-heptane and ethanol in their binary mixtures in counterflow diffusion flames.

3.2 Methodology

3.2.1 Analysis of reaction rate change

The objective of this analysis is to identify factors, either changes in value of the rate constant, species concentration or both, that primarily contribute to variations of the reaction rate under selected conditions.

The rates of forward reaction $\dot{\omega}_{f,k}$ and reverse reaction $\dot{\omega}_{b,k}$ of the k^{th} reversible reaction are determined by the product of the concentration of species i, c_i and their respective rate constants $k_{f,k}$ and $k_{b,k}$. Hence, $\dot{\omega}_{f,k} = k_{f,k} \prod_{i=1}^{m} c_i^{\nu_i'}$, $\dot{\omega}_{b,k} = k_{b,k} \prod_{i=1}^{m} c_i^{\nu_i''}$, where the parameters ν_i', ν_i'' represent the stoichiometric coefficients for species i appearing as a reactant and as a product in a reversible reaction, respectively.

In the analysis described here, forward and reverse steps of an elementary reaction is considered to be two separate reactions. Thus, if there are M reversible reactions, the total number of reactions considered as $2M$.

$$\dot{\omega}_n = \begin{cases} \dot{\omega}_{f,k}, n = 2k-1, \text{(for forward step)} \\ \dot{\omega}_{b,k}, n = 2k, \text{(for reverse step)} \end{cases} \quad \text{where } k = 1,2 \ldots M \tag{3.1}$$

Here, k denotes the k^{th} reversible elementary reactions before their separation into forward and reverse steps, while n represents the n^{th} reactions after separation. The total number of reactions after separation is N.

Similar to the approach taken in sensitivity analysis, the calculation of partial derivatives of the n^{th} reaction rate, $\dot{\omega}_n$, with respect to the rate constant, k_n, and species concentration, c_i, is a key parameter in reaction-rate-change-analysis.

Let $\Delta\dot{\omega}_n$ represent the difference in the value of $\dot{\omega}_n$ as a result of changes in the input variables, for example changes in initial composition of the reactive mixture. Let the corresponding changes in value of the rate constant k_n and concentration of species i be Δk_n and Δc_i, respectively. It follows that,

$$\begin{aligned} \Delta\dot{\omega}_n|_{k_n} &= \frac{\Delta\dot{\omega}_n}{\Delta\dot{\omega}_n^{\text{approx}}} \times \frac{\partial\dot{\omega}_n}{\partial k_n} \times \Delta k_n \\ \Delta\dot{\omega}_n|_{c_i} &= \frac{\Delta\dot{\omega}_n}{\Delta\dot{\omega}_n^{\text{approx}}} \times \frac{\partial\dot{\omega}_n}{\partial c_i} \times \Delta c_i \end{aligned} \tag{3.2}$$

where $\Delta\dot{\omega}_n|_{k_n}$ and $\Delta\dot{\omega}_n|_{c_i}$ are change of reaction rate caused by Δk_n and Δc_i. And the derivatives $\Delta\dot{\omega}_n^{\text{approx}}$, $\partial\dot{\omega}_n/\partial k_n$ and $\partial\dot{\omega}_n/\partial c_i$ are given by:

$$\begin{aligned} \Delta\dot{\omega}_n^{\text{approx}} &= \frac{\partial\dot{\omega}_n}{\partial k_n} \times \Delta k_n + \sum_{i=1}^{m} \left(\frac{\partial\dot{\omega}_n}{\partial c_i} \times \Delta c_i \right) \\ \frac{\partial\dot{\omega}_n}{\partial k_n} &= \prod_{i=1}^{m} c_i^{|\nu_i|}, \frac{\partial\dot{\omega}_n}{\partial c_i} = k_n \nu_i c_i^{|\nu_i|-1} \prod_{\substack{j=1 \\ i\neq j}}^{m} c_j{}^{|\nu_j|} \end{aligned} \tag{3.3}$$

with $\nu_i = \nu_i'' - \nu_i'$. Here, m represents the total number of species involved in the n^{th} reaction. The term $\Delta\dot{\omega}_n^{\text{approx}}$ is an approximation of $\Delta\dot{\omega}_n$, derived from the Taylor expansion truncated at

the first-order derivative. A second-order Taylor series expansion can be employed if improved accuracy is desired in evaluation of $\Delta\dot{\omega}_n|_{c_i}$ and $\Delta\dot{\omega}_n|_{k_n}$. Details are provided in below derivations.

The formula below outlines the approximated reaction rate from the second-order Taylor expansion for function of multiple variables:

$$\Delta\dot{\omega}_n^{\text{approx}} = \sum_{i=0}^{m} \frac{\partial \dot{\omega}_n}{\partial x_i}\Delta x_i + \frac{1}{2}\sum_{i=0}^{m}\sum_{j=0}^{m} \frac{\partial^2 \dot{\omega}_n}{\partial x_i \partial x_j}\Delta x_i \Delta x_j \tag{3.4}$$

For simplification, let the variable x_i encompasses both the rate constant, k_n, and the species concentration, c_i, with x_0 specifically denoting k_n.

$$x_i = \begin{cases} k_n, i = 0 \\ \\ c_i, i \neq 0 \end{cases} \quad \text{where} i = 0, 1... \tag{3.5}$$

By employing the second derivative in Taylor series, the change in reaction rate attributed to Δx_i could be written as:

$$\Delta\dot{\omega}_n|_{x_i} = \frac{\Delta\dot{\omega}_n}{\Delta\dot{\omega}_n^{\text{approx}}} \times \left(\frac{\partial \dot{\omega}_n}{\partial x_i}\Delta x_i + \frac{1}{2}\frac{\partial^2 \dot{\omega}_n}{\partial x_i^2}(\Delta x_i)^2 + \sum_{\substack{j=0 \\ j\neq i}}^{m} \frac{1}{2}\frac{\partial^2 \dot{\omega}_n}{\partial x_i \partial x_j}\Delta x_i \Delta x_j\right) \tag{3.6}$$

The term $\frac{\partial \dot{\omega}_n}{\partial x_i}\Delta x_i + \frac{1}{2}\frac{\partial^2 \dot{\omega}_n}{\partial x_i^2}(\Delta x_i)^2$ delineates the direct contribution of Δx_i to $\Delta\dot{\omega}_n$, encapsulating both linear and quadratic influences. While, the term $\frac{1}{2}\frac{\partial^2 \dot{\omega}_n}{\partial x_i \partial x_j}\Delta x_i \Delta x_j$ quantifies the synergistic influence on $\Delta\dot{\omega}_n$ emanating from interaction between Δx_i and Δx_j. This synergistic influence could be symmetrically attributed to the influence from both Δx_i and Δx_j.

3.2.2 Analysis of heat release rate change

The goal of the heat-release-rate-analysis is to provide quantitative information concerning the impact of changes in concentration each species on overall heat release rate, $\dot{Q}$, under different input boundary conditions. The quantity $\dot{Q} = \sum_k \Delta \mathrm{H}_k \times \dot{\omega}_k$, where $\Delta \mathrm{H}_k$ and $\dot{\omega}_k$ are,

respectively, the enthalpy change and net reaction rate of the k^{th} reaction. Furthermore, the net reaction rate $\dot{\omega}_k = \dot{\omega}_{f,k} - \dot{\omega}_{b,k}$. Hence, through separation operation, Eqn. (3.1), it follows that

$$\dot{Q} = -\sum_n \Delta \mathrm{H}_n \times \dot{\omega}_n \tag{3.7}$$

Heat-release-rate-analysis presented here is primarily focused on the high-temperature region where the input enthalpy of the reactant streams is maintained at constant values. Therefore, the local temperature at selected points for different boundary conditions of fuel streams are nearly the same allowing for the reasonable assumption that reaction enthalpy $\Delta \mathrm{H}_n$, which depends on local temperature, remains constant. Therefore, the contribution to change of heat release rate, $\Delta\dot{Q}$, arising from changes in rate constant, Δk_n and species concentrations Δc_i, are written as follows:

$$\Delta\dot{Q}|_{k,n} = -\Delta \mathrm{H}_n \times \Delta\dot{\omega}_n|_{k,n} \tag{3.8}$$

$$\Delta\dot{Q}|_{c_i} = \sum_n (-\Delta \mathrm{H}_n \times \Delta\dot{\omega}_n|_{c_i}) \tag{3.9}$$

The terms $\Delta\dot{Q}|_{k,n}$, and $\Delta\dot{Q}|_{c_i}$ represent the change of heat release rate attributed to the change in value of rate constant Δk_n of the n^{th} reaction and the change in value of concentration of species i, Δc_i.

3.2.3 Analysis of species concentration change

The goal of the analysis of species concentration change is to provide quantitative information concerning the impact of changes in rates of reactions on changes in concentration of species and elucidate the interaction among various species, particularly for those for which steady-state approximation are reasonably accurate. For species that do not satisfy steady-state approximation, the analysis includes the effects of species diffusion and convection on

concentration. Furthermore, diagrams illustrating species governing equation terms provides a visual representation that enhances understanding interactions associated with these species.

As an example, for the counterflow flame the steady state balance equation for species i is given by :

$$0 = -\rho u \frac{dY_i}{dz} - \frac{dj_i}{dz} + W_i(\dot{\omega}_i^+ - \dot{\omega}_i^-) \tag{3.10}$$

Here, z represents the spatial co-ordinate, ρ the density, u the mass-averaged velocity, Y_i, and W_i are the mass fraction and molecular weight of species i, j_i the diffusive flux of species i, and $\dot{\omega}_i^+$ and $\dot{\omega}_i^-$ are, respectively the rate of production and rate of consumption of species i. The first term on the right side of Eqn. (3.10) represents convective transport, the second term diffusive transport, and the third term the net rate of production of species i.

The production and consumption rate can be expressed as follows:

$$\begin{aligned}\dot{\omega}_i^+ &= \sum_k \nu_{i,k} \left[(1-\delta'_{i,k})\dot{\omega}_{f,k} - \delta'_{i,k}\dot{\omega}_{b,k}\right] \\ &= \sum_k |\nu_{i,k}| \left[(1-\delta'_{i,k})\dot{\omega}_{f,k} + \delta'_{i,k}\dot{\omega}_{b,k}\right]\end{aligned} \tag{3.11}$$

$$\begin{aligned}\dot{\omega}_i^- &= \sum_k \nu_{i,k} \left[-\delta'_{i,k}\dot{\omega}_{f,k} + (1-\delta'_{i,k})\dot{\omega}_{b,k}\right] \\ &= \sum_k |\nu_{i,k}| \left[\delta'_{i,k}\dot{\omega}_{f,k} + (1-\delta'_{i,k})\dot{\omega}_{b,k}\right]\end{aligned} \tag{3.12}$$

with $\delta'_{i,k}$ defined as

$$\delta'_{i,k} = \begin{cases} 1 & \text{if } \nu_{i,k} < 0, \\ 0 & \text{if } \nu_{i,k} > 0 \end{cases} \tag{3.13}$$

The term

$$\nu_{i,k} = \nu''_{i,k} - \nu'_{i,k}$$

where $\nu'_{i,k}$, $\nu''_{i,k}$ are the stoichiometric coefficients for species i appearing as a reactant and as a product in k^{th} reaction, respectively.

Governing equation of species i, Eqn.(**??**), could be rewritten as :

$$\dot{\omega}_i^- = -\rho u \frac{dY_i}{dz}/W_i - \frac{dj_i}{dz}/W_i + \dot{\omega}_i^+ \tag{3.14}$$

While, $\dot{\omega}_i^-$ can be expressed as:

$$\dot{\omega}_i^- = c_i \times \sum_k |\nu_{i,k}| \left[\delta'_{i,k} w_{f,k}^{den} + (1-\delta'_{i,k}) w_{b,k}^{den}\right] \tag{3.15}$$

where $w_{f,k}^{den}, w_{b,k}^{den}$ are defined as:

$$w_{f,k}^{den} = k_{f,k} \prod_{j=1}^{n} c_i^{\nu'_j - \delta_{i,j}}, w_{b,k}^{den} = k_{b,k} \prod_{j=1}^{n} c_i^{\nu''_j - \delta_{i,j}} \tag{3.16}$$

and $\delta_{i,j}$ indicates whether species j is species i:

$$\delta_{i,j} = \begin{cases} 1 & \text{if the species } j \text{ is species } i, \\ 0 & \text{otherwise.} \end{cases} \tag{3.17}$$

Combining the Eqn. (3.14) and Eqn. (3.15), the concentration of substance i, c_i can be derived from following expression:

$$c_i = \frac{-\rho u \frac{dY_i}{dz}/W_i - \frac{dj_i}{dz}/W_i + \dot{\omega}_i^+}{\sum_k |\nu_{i,k}| \left[\delta'_{i,k} w_{f,k}^{den} + (1-\delta'_{i,k}) w_{b,k}^{den}\right]} \tag{3.18}$$

Upon substituting Eqn. (3.11) into the equation above, we could obtain a detailed expres-

sion for c_i as:

$$c_i = \frac{-\rho u \frac{dY_i}{dz}/W_i - \frac{dj_i}{dz}/W_i + \sum_k |\nu_{i,k}| \left[(1-\delta'_{i,k})\dot{\omega}_{f,k} + \delta'_{i,k}\dot{\omega}_{b,k}\right]}{\sum_k |\nu_{i,k}| \left[\delta'_{i,k} w^{den}_{f,k} + (1-\delta'_{i,k}) w^{den}_{b,k}\right]} \tag{3.19}$$

In Eqn. (**??**), the terms $[-\rho u \frac{dY_i}{dz}/W_i]$ and $[-\frac{dj_i}{dz}/W_i]$ correspond to convective and diffusive mass transfer related term of species i, respectively. These terms can be neglected if steady-state approximation is satisfied. The term $\sum_k |\nu_{i,k}| \left[(1-\delta'_{i,k})\dot{\omega}_{f,k} + \delta'_{i,k}\dot{\omega}_{b,k}\right]$ accounts for all reactions producing species i while $\sum_k |\nu_{i,k}| \left[\delta'_{i,k} w^{den}_{f,k} + (1-\delta'_{i,k}) w^{den}_{b,k}\right]$ accounts for all reactions consumed species i.

The framework described by Eqn. (3.19), is used to analyze changes in the concentration of species i. For the k^{th} elemental reaction, the contribution of its forward reaction rate with respect to species c_i is:

$$\Delta c_i|_{f,k} = \begin{cases} \frac{1}{\text{sum}} \times \frac{\partial c_i}{\partial w_{f,k}} \times \Delta w_{f,k}\,, \nu_{i,k} > 0 \\ \frac{1}{\text{sum}} \times \frac{\partial c_i}{\partial w^{den}_{f,k}} \times \Delta w^{den}_{f,k}\,, \nu_{i,k} < 0 \end{cases} \tag{3.20}$$

Similarly, its backward reaction rate contribution with respect to c_i is expressed as:

$$\Delta c_i|_{b,k} = \begin{cases} \frac{1}{\text{sum}} \times \frac{\partial c_i}{\partial w_{b,k}} \times \Delta w_{b,k}\,, \nu_{i,k} < 0 \\ \frac{1}{\text{sum}} \times \frac{\partial c_i}{\partial w^{den}_{b,k}} \times \Delta w^{den}_{b,k}\,, \nu_{i,k} > 0 \end{cases} \tag{3.21}$$

The contributions of convective mass transfer with respect to changes in c_i are identified as:

$$\Delta c_i|_{\text{convection}} = \frac{1}{\text{sum}} \times \frac{\partial c_i}{\partial (\rho u \frac{dY_i}{dz})} \times \Delta(\rho u \frac{dY_i}{dz}) \tag{3.22}$$

Similarly, the contributions of diffusion mass transfer with respect to changes in c_i is expressed as:

$$\Delta c_i|_{\text{diffusion}} = \frac{1}{\text{sum}} \times \frac{\partial c_i}{\partial(\frac{dj_i}{dz})} \times \Delta(\frac{dj_i}{dz}) \tag{3.23}$$

Here, sum defined as the aggregate of all contributions to changes in c_i, encapsulating those from both the forward and backward reaction rates, as well as from the convective and diffusive mass transfers:

$$\begin{aligned}\text{sum} = &\sum \frac{\partial c_i}{\partial w_{f,k}} \times \Delta w_{f,k} + \sum \frac{\partial c_i}{\partial w_{f,k}^{den}} \times \Delta w_{f,k}^{den} \\ &+ \sum \frac{\partial c_i}{\partial w_{f,k}^{den}} \times \Delta w_{f,k}^{den} + \sum \frac{\partial c_i}{\partial w_{b,k}^{den}} \times \Delta w_{b,k}^{den} \\ &+ \frac{\partial c_i}{\partial(\rho u \frac{dY_i}{dz})} \times \Delta(\rho u \frac{dY_i}{dz}) + \frac{\partial c_i}{\partial(\frac{dj_i}{dz})} \times \Delta(\frac{dj_i}{dz})\end{aligned} \tag{3.24}$$

It has been established that for a species for which steady-state approximation is accurate, the magnitudes of both the rate of production and the rate of consumption are much larger than the sum of the magnitudes of the convective and diffusive terms [76]. Consequently, upon neglecting the diffusion and convection terms, the concentration of species i, as depicted in Eqn. (**??**), simplifies to:

$$c_i = \frac{\sum_k |\nu_{i,k}| \left[(1-\delta'_{i,k}) w_{f,k} + \delta'_{i,k} w_{b,k}\right]}{\sum_k |\nu_{i,k}| \left[\delta'_{i,k} w_{f,k}^{den} + (1-\delta'_{i,k}) w_{b,k}^{den}\right]} \tag{3.25}$$

Furthermore, the term sum simplifies in the steady-state(ss) approximation as follows:

$$\begin{aligned}\text{sum}_{ss} = &\sum \frac{\partial c_i}{\partial w_{f,k}} \times \Delta w_{f,k} + \sum \frac{\partial c_i}{\partial w_{f,k}^{den}} \times \Delta w_{f,k}^{den} \\ &+ \sum \frac{\partial c_i}{\partial w_{f,k}^{den}} \times \Delta w_{f,k}^{den} + \sum \frac{\partial c_i}{\partial w_{b,k}^{den}} \times \Delta w_{b,k}^{den}\end{aligned} \tag{3.26}$$

In scenarios where steady-state approximation is not applicable to species c_i, it becomes critical to consider all terms in the governing equation, including those related to diffusion

and convection. This comprehensive approach elucidates the relative significance of diffusion and convection and the chemical reaction term. Furthermore, for species that do not maintain steady-state, visualizing convection, diffusion and net production terms in Eqn. (3.10) helps to describe scenarios wherein species are produced in one region of the reaction zone transported to a different region of the reaction zone where they react. This is one of the key differences between reactions in flow systems (for example strained premixed and non-premixed flames) and non-flow systems (for example reactions in shock-tubes).

At a specific location, the dominance of one term over others in species equation highlights its pivotal role in shaping concentration profile. A positive value indicates an enhancement in concentration, whereas a negative value signifies a diminishing effect on concentration profile. This approach is elaborated in results and discussion section.

3.3 Demonstration of methodology

Low-temperature chemistry (LTC) is an intrinsic feature of combustion of hydrocarbons such as n-alkanes, alkenes and cycloalkanes, [77]. The LTC of n-heptane, for example, has been extensively investigated in various experimental setups, including the counterflow flame [66], shock tube[78], jet-stirred reactor[79], microgravity droplet flame [80]. Further studies have explored the impact of alcohol addition to n-heptane or other hydrocarbons in combustion characteristics[31]-[81]. While, traditional sensitivity method enhances the understanding of interactions within mechanisms, it falls short of detailing the influence between reactions and species across the reactive field.

Here, we demonstrate the use of the analysis method developed above to elucidate interaction between ethanol and n-heptane in counterflow flame. Computational results from a previous investigation [82] are used to illustrate the method. This previous study reports on species distribution, flame structure and critical conditions of auto-ignition obtained employing

the liquid-fuel counterflow configuration. These computations are performed using Cantera [61] C++ interface with modified boundary conditions at the liquid-gas interface. The mix-average transport model is applied to obtained steady-state solutions. Kinetic modeling is carried out using the San Diego Mechanism [60].

The fuels tested include n-heptane, ethanol, and their mixtures with volumetric composition of 20% n-heptane + 80% ethanol, 50% n-heptane + 50% ethanol, 70% n-heptane + 30% ethanol, 80% n-heptane + 20% ethanol, and 90% n-heptane + 10% ethanol. The oxidizer is air.

3.3.1 Auto-ignition temperature and heat release rate analysis

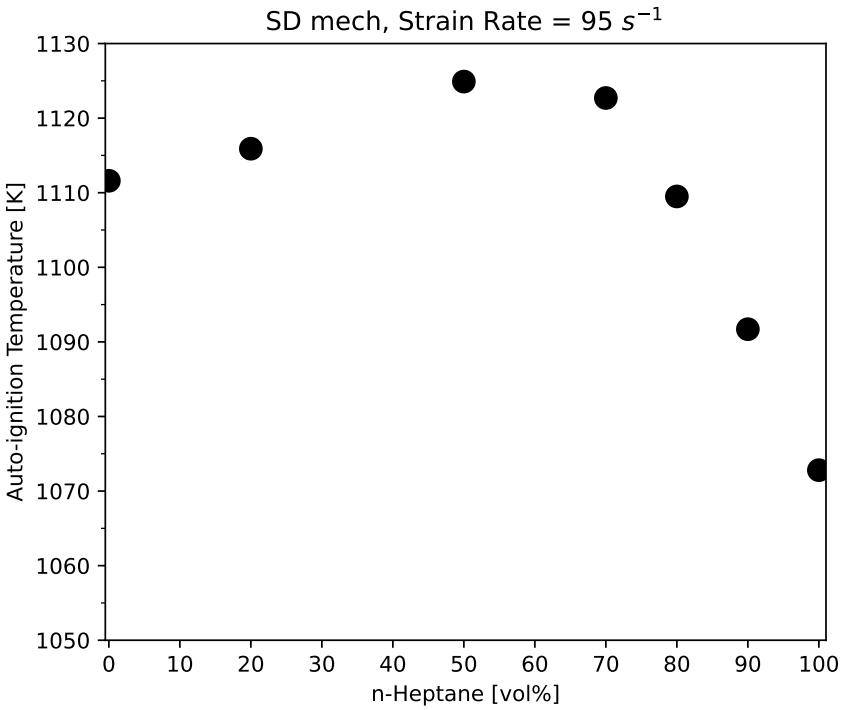

Figure 3.1: Auto-ignition temperature at strain rate of 95 s^{-1}.

Fig. 3.1 shows auto-ignition temperature calculated at low strain rate, $95s^{-1}$ for various volume fractions of ethanol in n-heptane, and Fig. 3.2 shows the variations in heat release rate, prior to auto-ignition, for these mixtures within the high-temperature zone, particularly focusing

at 4.3 mm above the liquid-gas interface and at an oxidizer temperature, T_{ox}, of 1060K. A comparison between Fig. 3.1 and Fig. 3.2 indicates a direct correlation between the magnitude of heat release rate in this zone and the requisite temperature of auto-ignition (T_{ig}). It is noteworthy that among the examined mixtures, the 50%n-heptane-50%ethanol blend stands out, because it has the highest value of ignition temperature, T_{ig}, a phenomenon that can be attributed to its lowest peak in heat release rate.

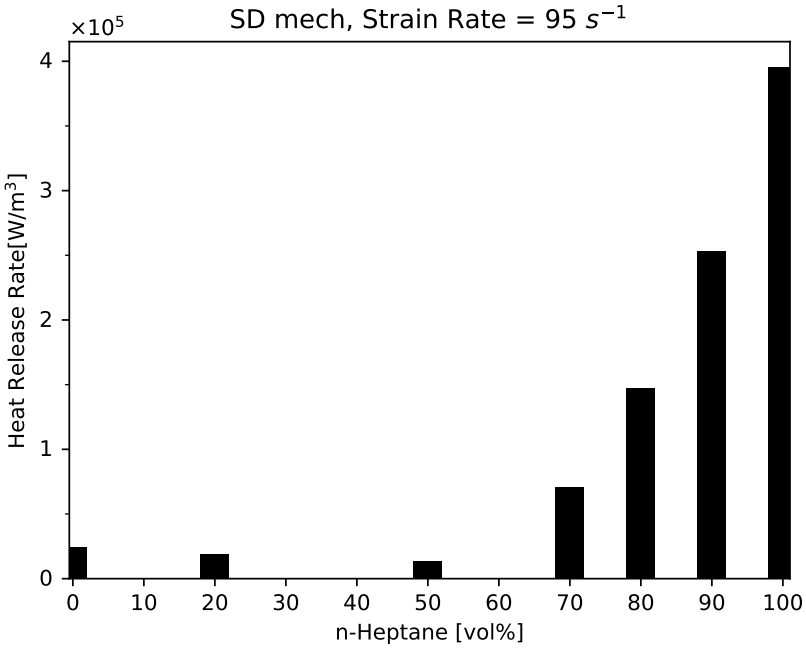

Figure 3.2: Heat release rate in the high-temperature zone [T_{ox}=1060 K]

Fig. 3.2 shows that the reduction of the volume fraction of heptane from 100% to 90% leads to a significant decrease in heat release rate. Furthermore heat-release-rate-analysis, as depicted in Fig. 3.3, directly attributes this decline of heat release rate predominantly to changes of concentrations of HCO, HO_2, OH, C_2H_5, C_2H_3, CH_2O. In contrast, the reduction in volume fraction of n-heptane from 50% to 20% correlates to an observable increase in heat release rate, as shown in Fig. 3.2. Similar results of heat-release-rate-analysis shown in Fig. 3.4 attributes the increase of heat release rate to involvement of species such as CH_3, HO_2, OH, HCO, C_2H_5OH, CH_3CHOH, CH_2O.

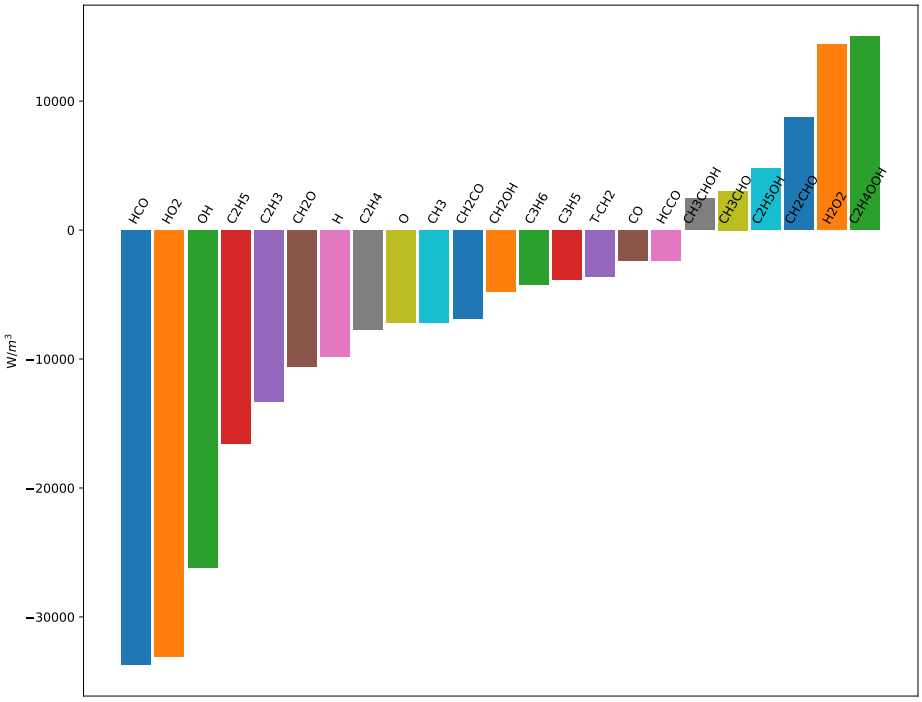

Figure 3.3: Distribution of heat release rate change from 100%n-heptane to 90%n-heptane

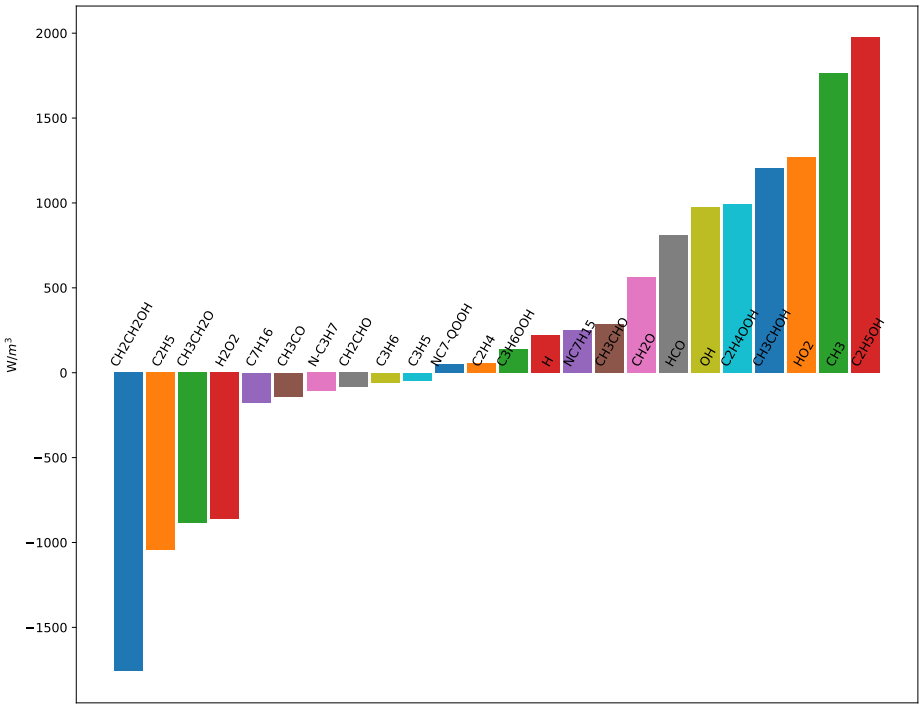

Figure 3.4: Distribution of heat release rate change from 50% n-heptane to 20% n-heptane

3.3.2 Key species in n-heptane-dominant mixtures

The species contributing to heat release rate change could be placed in two groups; one that can be considered to maintain steady-state at a selected location. and the other that does not maintain steady-state.

For species that do not satisfy steady-state approximation, their concentrations are governed by a species equation that includes diffusion term, convection term and chemical reaction term. Specifically, in Fig. 3.5, for CH_2O, that does not maintain steady-state the peak in the net production is observed around 1.2 mm, that is located in a zone where the LTC is highly active. Additionally, the positive values of the diffusion term between 2 mm and 5 mm elucidate the role of the diffusion term in promoting the transport of the CH_2O from the low-temperature zone to the high-temperature zone. Consequently, a decline of activity of LTC in the low-temperature region, caused by additional ethanol, leads to a reduction of diffusion effect, subsequently impacting heat release rate and auto-ignition at the high-temperature region. This effect is also evidenced by analysis of CH_2O concentration change, depicted in Fig. 3.6. The observed reduction of CH_2O in the high-temperature region is primarily attributed to a decrease in the value of the diffusion term. Similar behaviors are observed with other species, specifically ethylene (C_2H_4), propene(C_3H_6), and hydrogen peroxide (H_2O_2). The corresponding analyses and plots for these species are shown in the supplemental materials (Fig. A.1 - Fig. A.4).

For species that are considered to maintain steady-state, their concentrations are predominantly governed by the equilibrium between production and consumption rates at a selected location. Among the primary species shown in Fig. 3.3 that leads to heat release rate reduction, HCO, HO_2, OH, C_2H_5 and C_2H_3 are identified to be in the steady-state. This indicates these radicals are produced and consumed at approximately the same rate at the selected location. Consequently, changes in their concentrations at this location are primarily affected by certain elementary reactions, instead of species diffusion or convection. Moreover, these reactions is controlled by variations of other species in the chemical system. These related reactions and

species can be elucidated through further analysis of concentration change.

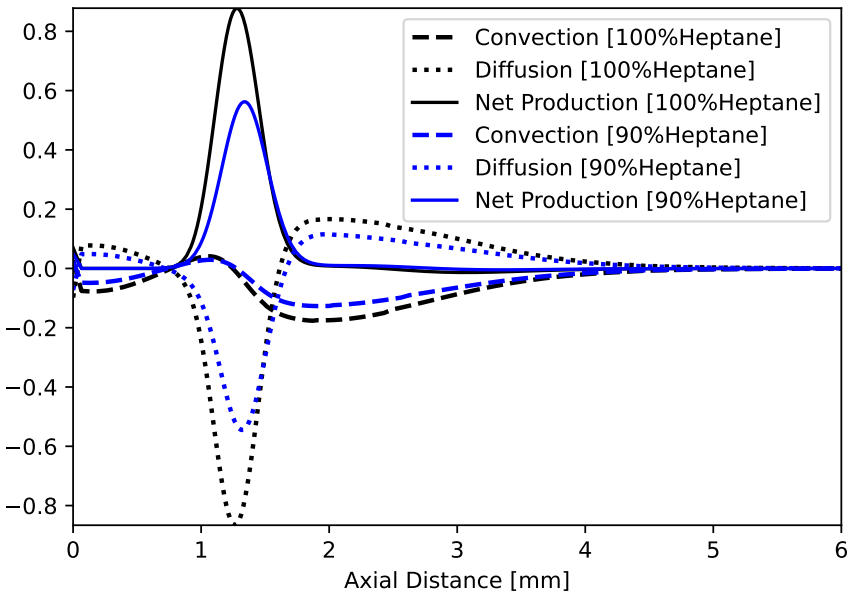

Figure 3.5: Species equation terms - CH_2O (n-heptane dominant mixtures)(ethanol dominant mixtures)

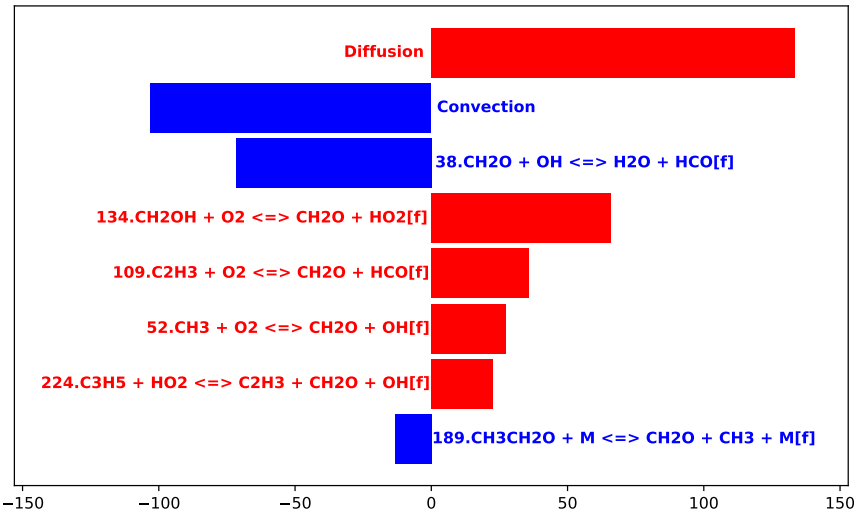

Figure 3.6: Contribution on CH_2O concentration change@4.2mm (n-heptane dominant mixtures)

Fig. 3.7 demonstrates that changes in concentration of radical OH at the high-temperature zone are primarily affected by reverse reaction of R16, which is R16r: H_2O_2 (+M) $\rightarrow$ 2 OH

(+M) , involving the decomposition of H_2O_2; H_2O_2 is not in steady state and is diffused from the low-temperature zone.

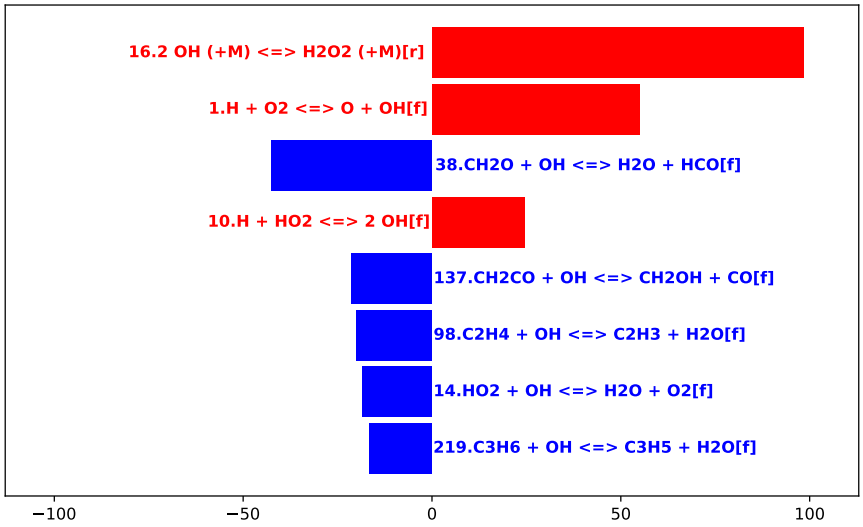

Figure 3.7: Contribution to OH concentration change@4.2mm (n-heptane dominant mixtures)

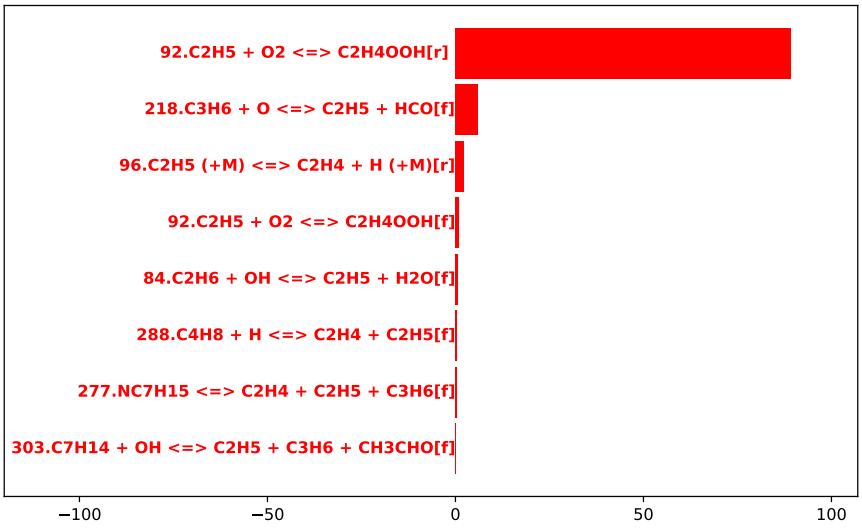

Figure 3.8: Contribution on C_2H_5 concentration change@4.2mm (n-heptane dominant mixtures)

Further concentration analysis reveals that concentration of HO_2 is predominantly controlled by HCO, through R33f: $HCO + O_2 \rightarrow CO + HO_2$. Similarly, HCO concentration are primarily controlled by CH_2O and OH via R38f: $CH_2O + OH \rightarrow H_2O + HCO$. Concentration of C_2H_3 is primarily regulated by C_2H_4 by R98f: $C_2H_4 + OH \rightarrow C_2H_3 + H_2O$. Illustrative plots of

these relationships are provided in the supplemental materials, as seen in Fig. A.5, A.6, and A.7. As mentioned before, both CH_2O and C_2H_4 are mainly transported from the low-temperature region via diffusion.

Fig. 3.8 reveals that the radical C_2H_5 is primarily influenced by R92: C_2H_5+$O_2 \rightleftharpoons C_2H_4OOH$. However, it is actually a fast reaction so that the substantial consumption of C_2H_5 in the forward reaction is counterbalanced by its production in the reverse reaction. Therefore, greater emphasis should be placed to the second reaction depicted in Fig. 3.8, R218f: C_3H_6 + O $\rightarrow$ C_2H_5 + HCO, which is primarily affected by C_3H_6. Notably, C_3H_6 is not in the steady state at the high-temperature zone and is primarily diffused from the low-temperature region.

In summary, species including CH_2O, C_2H_4, C_3H_6 and H_2O_2 predominantly diffused from the low-temperature zone, significantly influencing the heat release rate and auto-ignition process in the high-temperature zone.

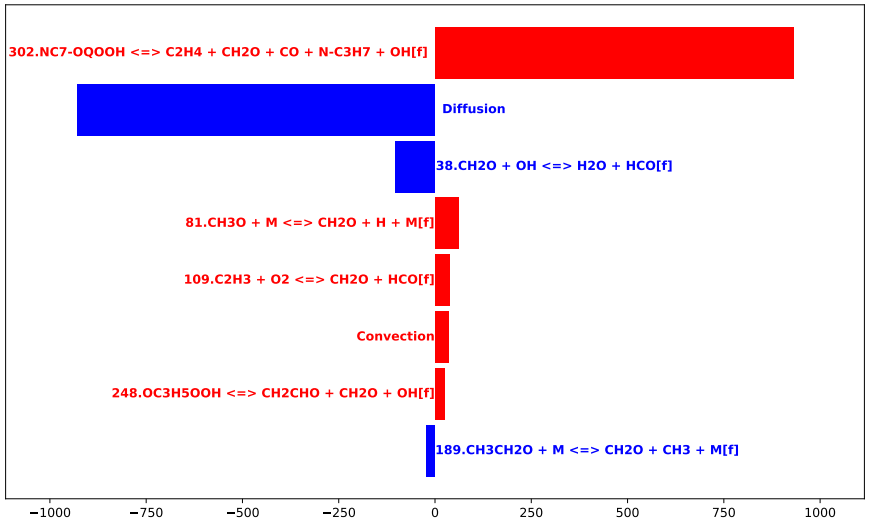

Figure 3.9: Contribution on CH_2O concentration change@1.1mm (n-heptane dominant mixtures)

This observation underscores the necessity of delineating the production mechanism of these species in the low-temperature zone. As indicated in Fig. 3.9 and Fig. 3.10, CH_2O and C_2H_4 primarily produced through reaction R302f: n-C_7OQOOH$\rightarrow$ C_2H_4 + CH_2O + CO + n-C_3H_7 + OH at the low-temperature zone.

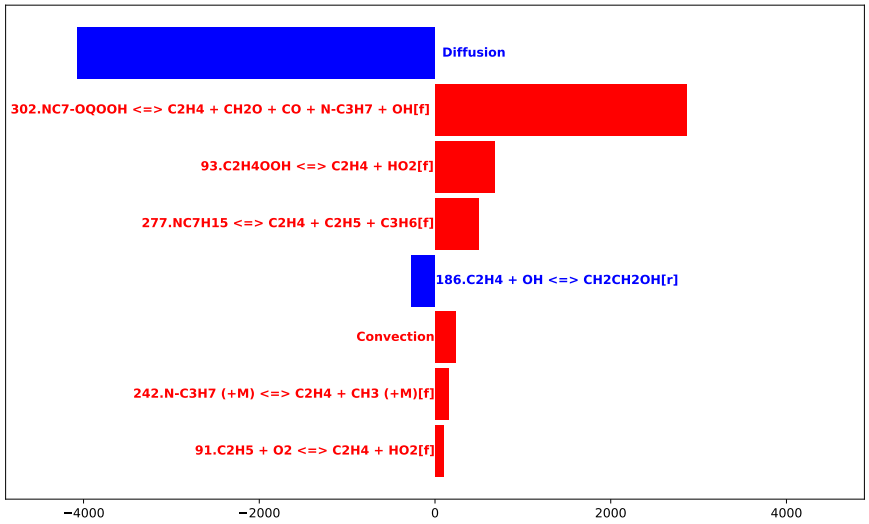

Figure 3.10: Contribution on C_2H_4 concentration change@1.1mm (n-heptane dominant mixtures)

The origins of C_3H_6 and H_2O_2 in the low-temperature zone is notably complex. Fig. 3.11 proves that concentration of C_3H_6 is predominantly regulated by n-C_3H_7. Similarly, concentration analysis of H_2O_2 and HO_2 indicate H_2O_2 is mainly converted from HO_2, which, in turn, is affected by n-C_3H_7. These analysis results are further detailed in the supplemental materials, specifically in Fig. A.8 and A.9.

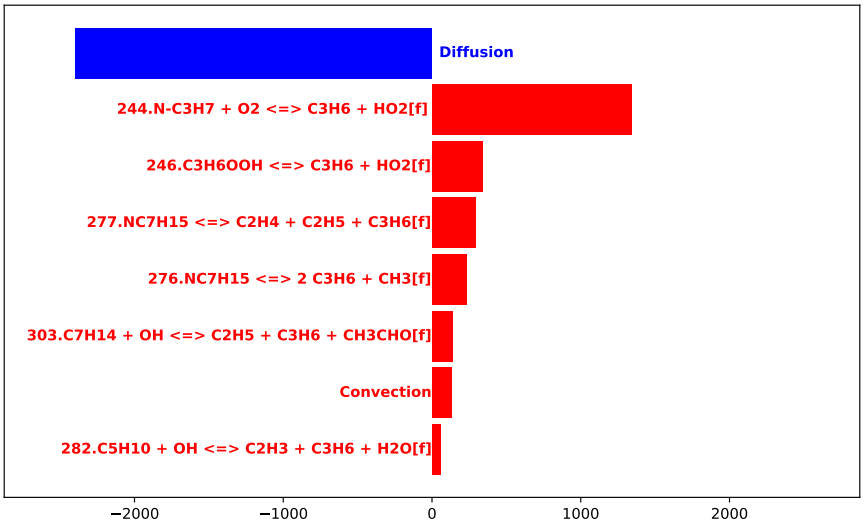

Figure 3.11: Contribution on C_3H_6 concentration change@1.1mm (n-heptane dominant mixtures)

Given its pivotal role, n-C_3H_7 emerges as a crucial species impacting both H_2O_2 and C_3H_6. It is primarily produced through reaction R302f, as indicated in Fig. 3.12. Thus, in the low-temperature region, R302f exerts a direct influence on producing CH_2O, C_2H_4, while indirectly affecting C_3H_6 and HO_2 via n-C_3H_7.

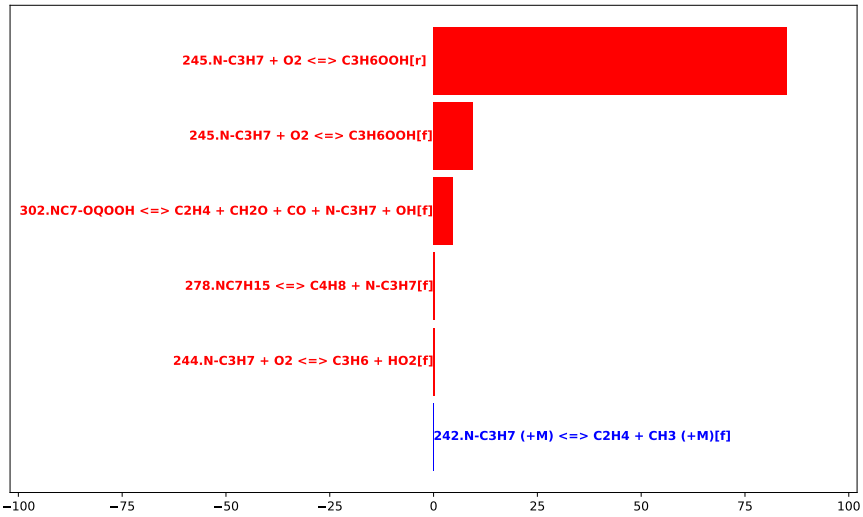

Figure 3.12: Contribution on n-C_3H_7 concentration change@1.1mm (n-heptane dominant mixtures)

Fig. 3.13 provides a comprehensive overview elucidating interplay between the low and high temperature zones in n-heptane-dominant mixtures. The addition of ethanol leads to competition of oxygen, resulting in a decreased of n-C_7OQOOH concentration in the low-temperature zone[82]. This reduction in concentration of n-C_7OQOOH subsequently diminishes the reaction rate of R302f and concentrations of its products. Ultimately, these effects propagated to the high-temperature zone through species diffusion.

3.3.3 key species in ethanol-dominant mixtures

It is observed that a decrease of n-heptane's volume fraction from 50% to 20% and a corresponding increase in ethanol's volume fraction from 50% to 80%, results in an increase in heat release rate in the high-temperature zone. This is primarily due to the formation of three

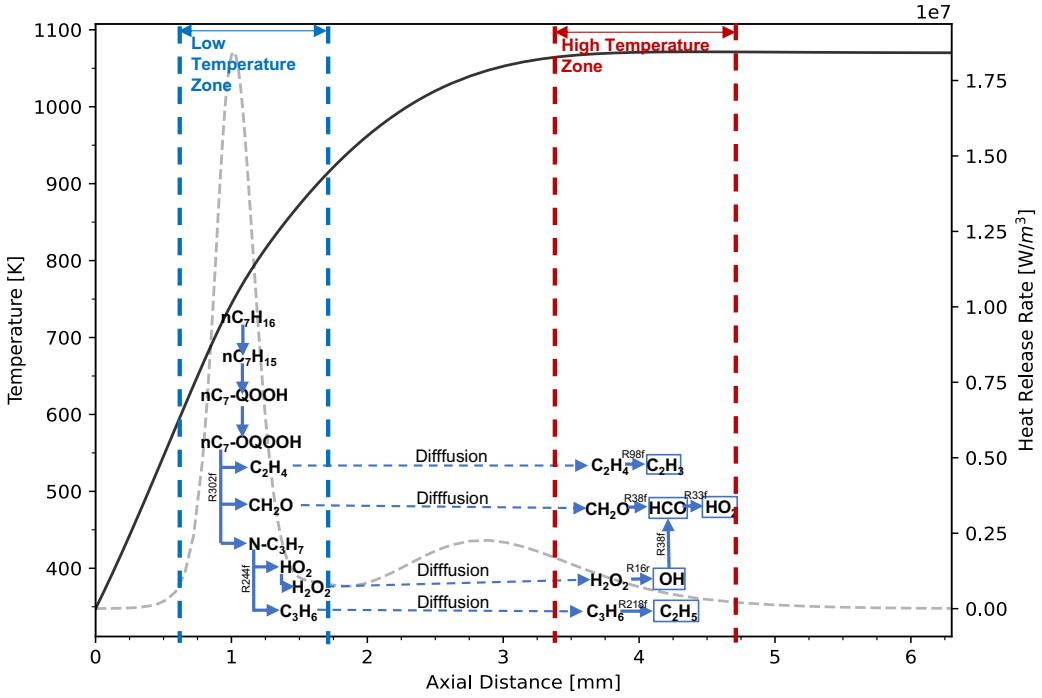

Figure 3.13: n-heptane dominant mixtures overview. In the background, the black solid line represents the temperature profile and the grey dashed line indicates heat release rate

products: CH_3CHOH, CH_2CH_2OH and CH_3CH_2O, as shown in Fig 3.19. These products are formed from ethanol undergoing decomposition through hydrogen abstraction. [3]

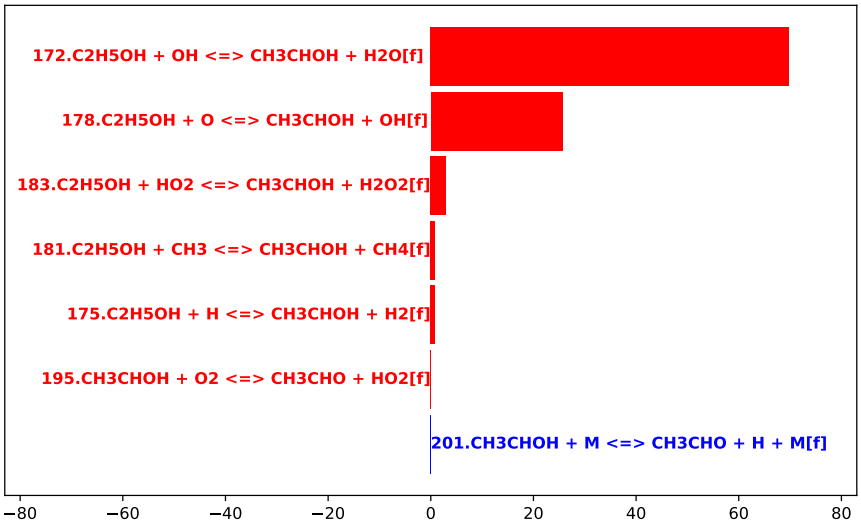

Figure 3.14: Contribution on CH_3CHOH concentration change@4.2mm (ethanol dominant mixtures)

Production of CH_3CHOH, mainly from reactions R172f: $C_2H_5OH + OH \rightarrow CH_3CHOH + H_2O$ and R178f: $C_2H_5OH + O \rightarrow CH_3CHOH + OH$, plays a significant role in increasing heat release rate, as confirmed in Fig. 3.14. Notably, one pathway to form CH_3CHOH, via R183f: $C_2H_5OH + HO_2 \rightarrow CH_3CHOH + H_2O_2$, is accompanied by a significant production of H_2O_2, as depicted in Fig. 3.15b, with the peak production around 2.0mm-2.2mm, shown in Fig. 3.15a. It is subsequently diffused to the high-temperature region, contributing to the increase of OH concentration through R16r , H_2O_2 (+M) $\rightarrow$ 2 OH (+M), corroborated by Fig. 3.16. Additionally, the reverse reaction of R186, involving the decomposition of CH_2CH_2OH, contributes to the elevation of OH concentration, as indicated in Fig. 3.16.

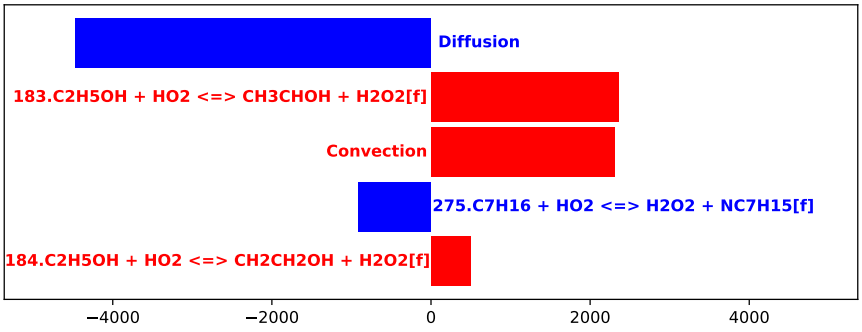

(a) At production peak (2.2mm)

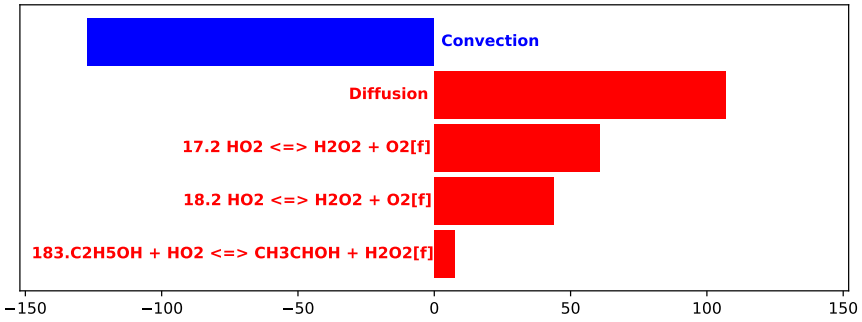

(b) At the high-temperature zone (4.2mm)

Figure 3.15: Contribution on H_2O_2 concentration change (ethanol dominant mixtures)

Furthermore, Fig. 3.17a demonstrates that the elevated levels of CH_3CHOH (through R195f) and CH_3CH_2O (through R188f) lead to an increase in CH_3CHO. Furthermore, Fig. 3.17b confirms that some of the of increase of CH_3CHO is by diffusion from its production peak

region to the high-temperature region, thereby promoting heat release rate.

As shown in Fig. 3.18, the products CH_3 and CH_2O from decomposition of CH_3CH_2O through R189f and from the step CH_3CH_2O +M$\rightarrow$ CH_2O + CH_3 +M, diffuse to the high-temperature region. This process is augmented by R52f: CH_3 + O_2 $\rightarrow$ CH_2O + OH, as illustrated in Fig A.10, wherein CH_3 reacts with O_2, further elevating the concentration of CH_2O. The increase in CH_2O and OH leads to a rise in HCO and as a consequence to an enhanced concentration of HO_2 in the high-temperature region. The concentration change analysis related to CH_2O, HCO and HO_2 are provided in Fig. A.10, Fig. A.11 and Fig. A.12 in supplemental materials.

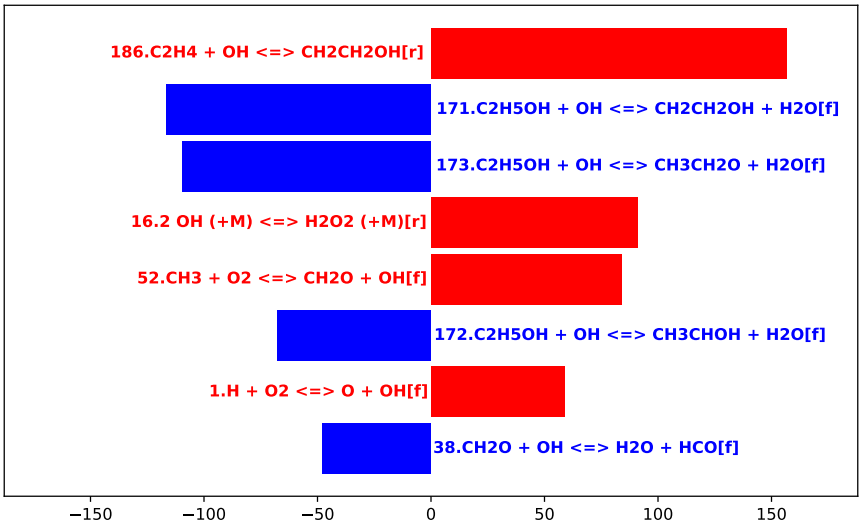

Figure 3.16: Contribution on OH concentration change @4.2mm (ethanol dominant mixtures)

The reaction pathway including CH_2O, HCO and HO_2 exhibits similarity in both n-heptane-dominant and ethanol-dominant mixtures. However, the concentration of CH_2O in n-heptane-dominant mixtures is predominantly influenced by the low-temperature chemistry of n-heptane, whereas in ethanol-dominant mixtures, CH_2O is significantly affected, directly and indirectly, by CH_3CH_2O, through ethanol's hydrogen abstraction reaction, R189f.

Additionally, the increase in HO_2 partially results in heightened level of H_2O_2 at the high-temperature region, as evidenced in Fig. 3.15b.

Fig. 3.19 succinctly summarizes the reaction pathways and diffusive effects associated with ethanol-dominant mixtures. The observed increase in heat release rate, as ethanol volume fraction increased from 50% to 80%, is primarily attributable to radicals and reactions associated with ethanol's chemistry. In these mixtures, the influence of the inhibition of LTC is considered to be negligible.

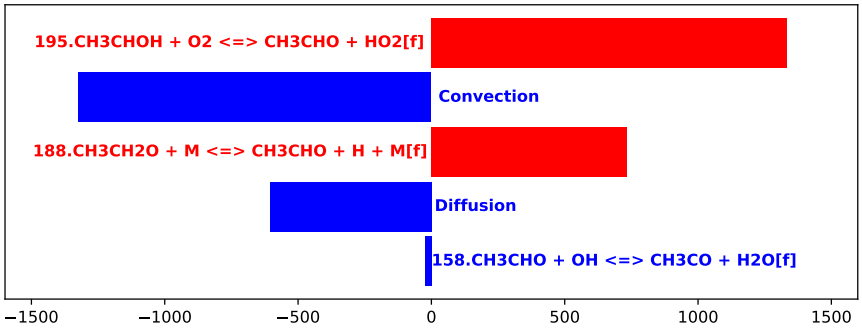

(a) At the production peak (3.0mm)

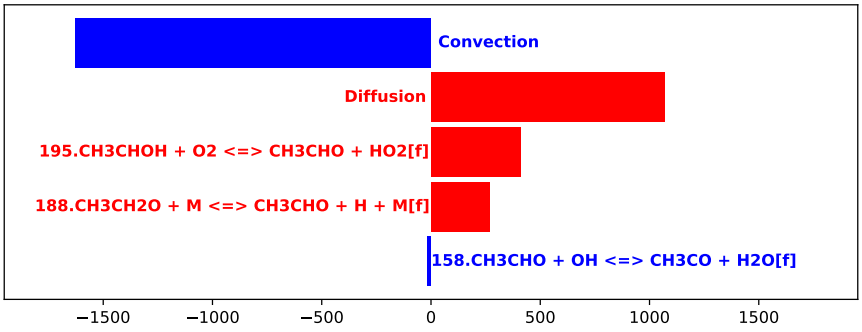

(b) At the high-temperature zone (4.2mm)

Figure 3.17: Contribution on CH_3CHO concentration change (ethanol dominant mixtures)

3.3.4 Summary

The demonstrated example specifically concerns combustion of n-heptane and ethanol mixtures in a counterflow flame at low strain rate. Simulation results indicate a correlation between heat release rate and auto-ignition temperature. Further quantitative analyses, utilizing the proposed method, reveal that changes in the heat release rate in both n-heptane and ethanol dominant mixtures are associated with the concentration change of certain species in the high-

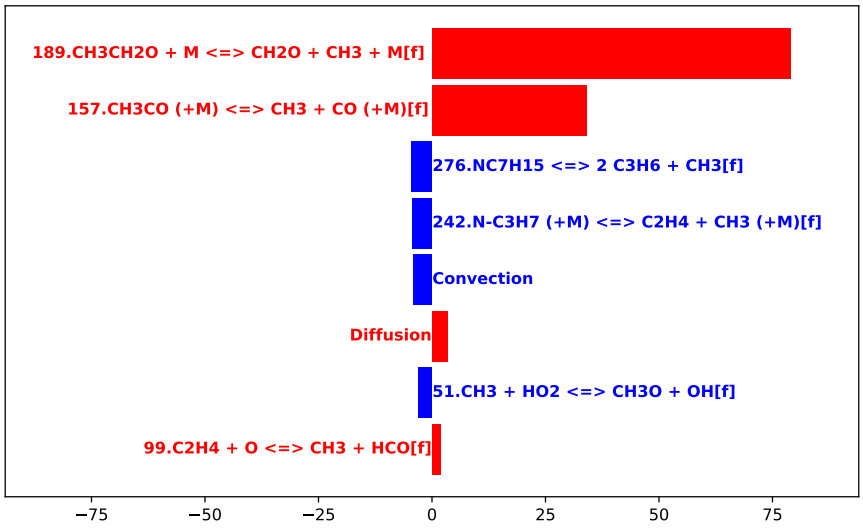

Figure 3.18: Contribution on CH_3 concentration change@4.2mm (ethanol dominant mixtures)

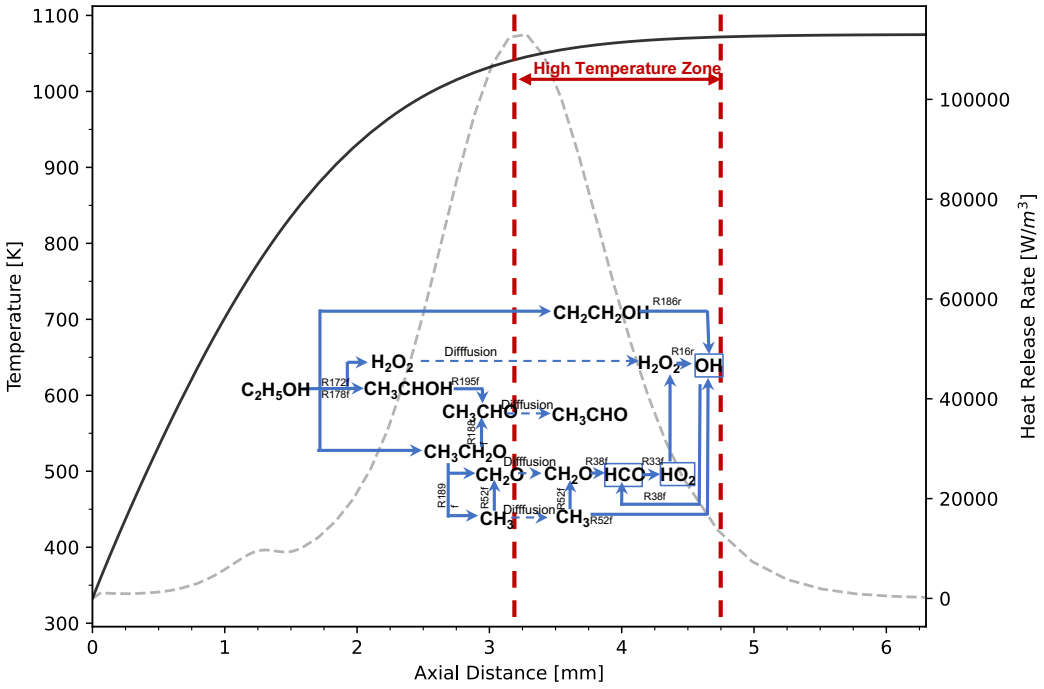

Figure 3.19: Ethanol-dominant mixtures overview. In the background, the black solid line represents the temperature profile and the grey dashed line indicates heat release rate

temperature zone.

In n-heptane-dominant mixtures, the investigation reveals that steady-state species at the high-temperature zone, including hydroxyl radicals (OH) and hydroperoxyl radicals (HO_2),

maintain the equilibrium between production and consumption rate, directly affecting heat release rate. Non-steady-state species at the high-temperature zone, such as CH_2O and C_2H_4 play significant roles in the auto-ignition process, primarily due to their involvement in low-temperature chemistry at the low-temperature zone and subsequent species diffusion to the high-temperature region.

For ethanol-dominant mixtures, the study highlights the observed increase in heat release rate with the increase in ethanol's volume fraction, attributing this elevation to the decomposition of ethanol into major products including CH_3CHOH, CH_2CH_2OH and CH_3CH_2O radicals. The production of these species, particularly through hydrogen abstraction reactions, is identified as the key pathway driving the observed increase in heat release rate.

Using the proposed method, we identified the key species involved in diffusion and demonstrate how the diffusion of these species bridges the low and high temperature zones in n-heptane-dominant mixtures. Additionally, the analysis results indicates, in the ethanol dominant mixtures, chemical kinetics are notably unaffected by n-heptane's LTC, highlighting the distinctive chemical pathways of ethanol and the influence of fuel composition on heat release rate and auto-ignition.

3.4 Conclusion and outlook

This work proposed a method of analysis to reveal the relationship between change in heat release rate and variations of species, elucidating interaction among related species and the potential influence of species transport across different temperature zones in reactive field.

For demonstration, the study investigated the auto-ignition temperature of n-heptane and ethanol mixtures in a counterflow flame configuration under low strain rates. The analysis results indicate that this method effectively quantifies and compares the influence of chemical kinetics and species diffusion effects, detailing the complex interactions of critical species that influence the heat release rate.

Future research directions may include applying the method of analysis under varying strain rates and extending to other one-dimensional flame configurations. Additionally, given the complexity of preparing the overview figures for various mixtures, future efforts will focus on streamlining the analysis process through enhancing code automation.

Acknowledgements

This chapter, in part, is currently being prepared for submission for publication of the material. Analysis of Structure and Interactions Between Chemical Reactions, Species Transport and Heat Release in Laminar Flames, L. Ji, K. Seshadri. The dissertation author was the primary investigator and author of this material.

Chapter 4

Renewable Natural Gas Production from Biomass with Power to Gas

4.1 Introduction

Power-to-gas (PtG) technology represents an approach to utilizing electric power for the production of gaseous fuels. This technology encompasses three primary systems: Power-to-hydrogen (PtH), Power-to-methane (PtM), and Power-to-syngas (PtS).

The PtH employs electrolysis to produce hydrogen from water often as an adjunct to wind parks or solar power plants for storing surplus or off-peak power.

However, hydrogen presents several challenges in practical applications. hydrogen gas is highly flammable and can easily escape containment. If hydrogen gas escapes containment, it can corrode metals. This exposure can, in turn, make the contaminated metals brittle and prone to breaking. The transportation of hydrogen is costly and challenging. Moreover, utilizing hydrogen in traditional combustion engines requires significant adaptations and redesigns to accommodate its unique properties compared to conventional fossil fuels like gasoline and methane. The development and widespread adoption of hydrogen fuel cells require substantial long-term investment and sustained financial commitment.

In our investigations, we explored incorporating the additional hydrogen produced via PtH into the methanation process of producer gas. The resulting product, methane, can be

directly utilized in transportation vehicles without the need for further modifications. Methane transportation infrastructure is also well-developed and more efficient compared to that for hydrogen, presenting fewer transport challenges. This approach leverages existing technologies and infrastructures, enhancing the practicality and economic viability of using renewable energy-derived hydrogen.

In this process, methanation is the core process combining hydrogen and CO_2 and CO to make methane [83]. The process of methanation generally follows one of two pathways: catalytic/ thermochemical or biological.

In the catalytic/thermochemical approach, often referred to as the Sabatier process[84], metal catalysts are employed to facilitate the necessary chemical reactions for fuel production. Optimal conditions for these reactions usually range between 200°C and 550°C, under pressures up to 100 bar, typically in fixed bed reactor[85]. Contrastingly, biological methanation utilizes biocatalysts, specifically methanogenic microorganisms, in place of metallic catalysts. This bio-methanation process typically operates at milder temperatures of 35°C to 70°C and at lower pressures ranging from 1 to 15 bar [86].

Central to the methanation process are the reactions for CO methanation and CO_2 methanation, which are detailed respectively below:

$$\mathrm{CO} + 3\mathrm{H_2} \Longleftrightarrow \mathrm{CH_4} + \mathrm{H_2O(g)}, \quad \Delta \mathrm{H_{298K}} = -206.1\,\mathrm{kJ/mol} \tag{4.1}$$

$$\mathrm{CO_2} + 4\mathrm{H_2} \Longleftrightarrow \mathrm{CH_4} + 2\mathrm{H_2O(g)}, \quad \Delta \mathrm{H_{298K}} = -164.1\,\mathrm{kJ/mol} \tag{4.2}$$

The proposed catalytic methanation mechanisms for both CO and CO_2 are categorized into two distinct types: (1) the associative pathway and (2) the dissociative pathway. [87]

In the associative scheme for CO_2, as illustrated in Figure 4.1 (a), CO_2 is adsorbed in association with adatom H_{ad}, leading to the formation of oxygenate intermediates that are

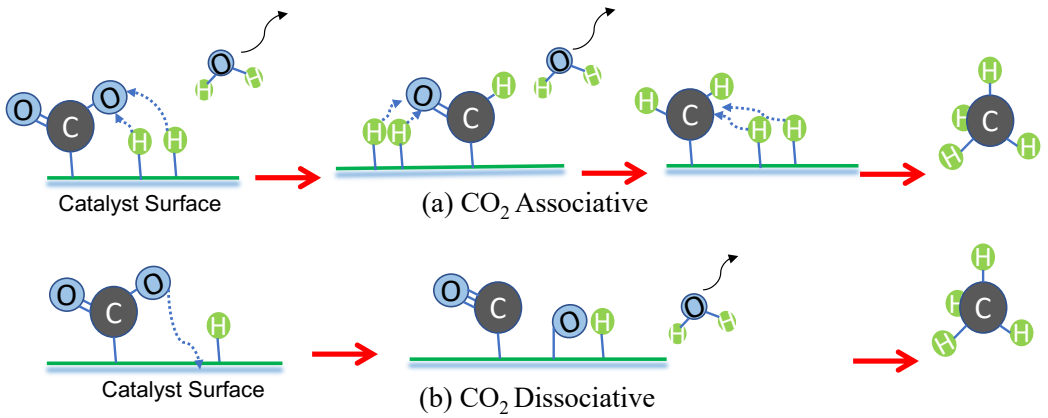

Figure 4.1: Schematic of CO_2 methanation mechanism [87]

subsequently hydrogenated to CH_4. In contrast, the dissociative scheme, depicted in Figure 4.1 (b), involves the initial dissociation of CO_2 into carbonyl (CO_{ad}) and O_{ad}, followed by the hydrogenation of the carbonyl to produce CH_4. The selection between associative and dissociative methanation mechanisms depends on the specific reaction conditions.

For CO, the associative mechanism involves the interaction of H_{ad} with CO_{ad} to form intermediates such as COH_{ad}, CHO_{ad}, or $CHOH_{ad}$, which leads to subsequent C–O bond breaking. Direct C–O bond breaking without the assistance of hydrogen is recognized as kinetically unfavorable in numerous investigations. Consequently, H_{ad} reacts with the carbonyl group to form formyl (CHO_{ad}) or carbon-hydroxyl (COH_{ad}), thereby facilitating the breaking of the C–O bond. This process is illustrated in Figure 4.2 (a).

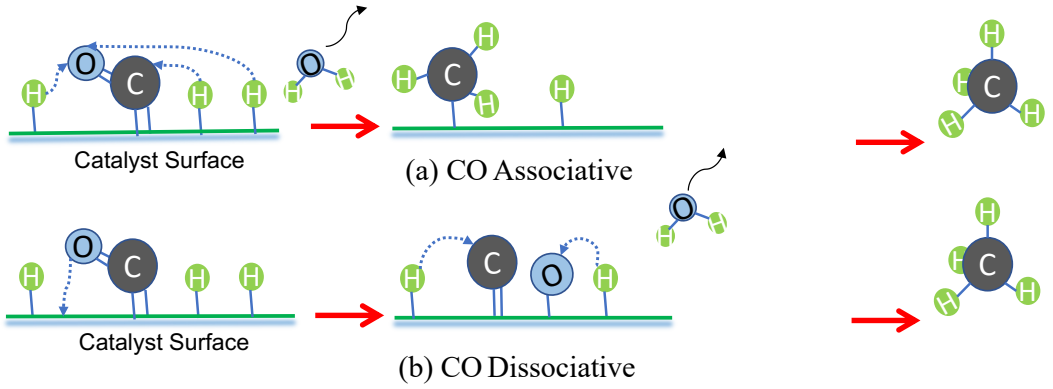

Figure 4.2: Schematic of CO methanation mechanism [87]

Conversely, the dissociative mechanism, illustrated in Figure 4.2 (b), involves the direct dissociation of adsorbed CO_{ad}, forming surface-carbon (C_{ad}) as the intermediate for methanation.[88] This process includes the direct breaking of the C–O bond at the active sites, followed by successive hydrogenation steps. CO exhibits greater activity than CO_2 in methanation processes. Previous studies have demonstrated that both associative and dissociative pathways significantly contribute to CH_4 production, each facilitating the reaction under specific conditions[89].

Given that these methanation reactions are highly exothermic, they can lead to a significant temperature increase during the process, potentially causing severe sintering of the catalyst[90]. Additionally, the effectiveness of catalytic methanation of CO_x oxides is challenged by slow kinetics. Thus, optimizing catalyst performance, especially in the low-temperature region, becomes crucial to enhance the efficiency and stability of the methanation process.[91]

Metals such as Ni, Ru, Rh, Co, and Fe have been extensively researched as methanation catalysts [91–93]. Among these, nickel (Ni) is recognized as the most practical option due to its high activity and cost-effectiveness [94]. However, Ni catalysts face several challenges, including deactivation at high temperatures due to sintering, carbon deposition, and sulfur poisoning [95]. The performance of Ni catalysts heavily depends on the characteristics of the support oxides and the stabilization and creation of adsorption sites for reactants. To enhance the dispersion and thermal stability of Ni, promoters such as MgO [96], La_2O_3 [97], and CeO_2 [98] have been employed. Particularly, MgO has gained popularity due to its effectiveness and affordability, making it a favored choice for enhancing methanation reactions.

Moreover, the integration of ruthenium[99], highly active for methanation, with Ni catalysts to create Ni-Ru bimetallic catalysts has garnered attention for improving activity, stability and sulfur tolerance. Tinku, et al developed and patented catalyst including Ni, Ru and MgO exhibited superior stability, especially, in comparison to a promoted Ni-based commercial catalyst [91] [100]. They found that a combination of 2.5% MgO and 25% (Ni95Ru05) on Sasol alumina support yielded the highest activity. Furthermore, experiments employing high-surface-

area commercial alumina supports with the Ni-Ru-Mg catalyst demonstrated CO conversion activity comparable to that of commercial catalysts. Crucially, this catalyst configuration effectively eliminated deactivation due to coke formation, a common issue in the low H_2/CO-ratio producer gas typically found in biomass gasification.

Thus, in the current investigation, the Ru-Ni-MgO catalyst (2.5% MgO-25%(Ni95Ru05)), supported on high-surface-area commercial alumina, has been utilized to evaluate its performance in methanation activity for producer gas across a wide range of H/C ratios. The experiments on the catalytic methanation of producer gas with additional hydrogen increasing the H/C ratios were conducted in both a temperature-controlled, fixed-bed reactor and fluidized-bed reactor, under atmospheric pressure

4.2 Experiments of Methanation

4.2.1 Fixed Bed Reactor

The investigation of the methanation of the CO and CO_2 in producer gas with additional hydrogen from power to gas, was conducted in a temperature-controlled fixed-bed methanation flow reactor developed in previous research [101] and shown schematically in Figure 4.3. A Ni/Ru/MgO methanation catalyst was used in the experiments previously developed [91] and patented [100].

The fixed bed reactor, a crucial reactor for heterogeneous catalytic reactions, emphasizes the effectiveness of catalyst and associated heat and mass transfer processes. It comprises a cylindrical column packed with catalyst pellets that facilitate the production of methane from input producer gas, eliminating the need for separation between catalyst and product [102].

In our investigation regarding weight hourly space velocity (WHSV) of 96000 scc/hr/g, the reactor contained 250mg of the catalyst as prepared previously [91] on a Sasol Puralox 300/200 alumina support (290 micron diameter, impregnated surface area 106m^2/g) and mixed with 5.0 g of (1.5mm) quartz chips in a 10 mm ID quartz tube. Gas composition before and

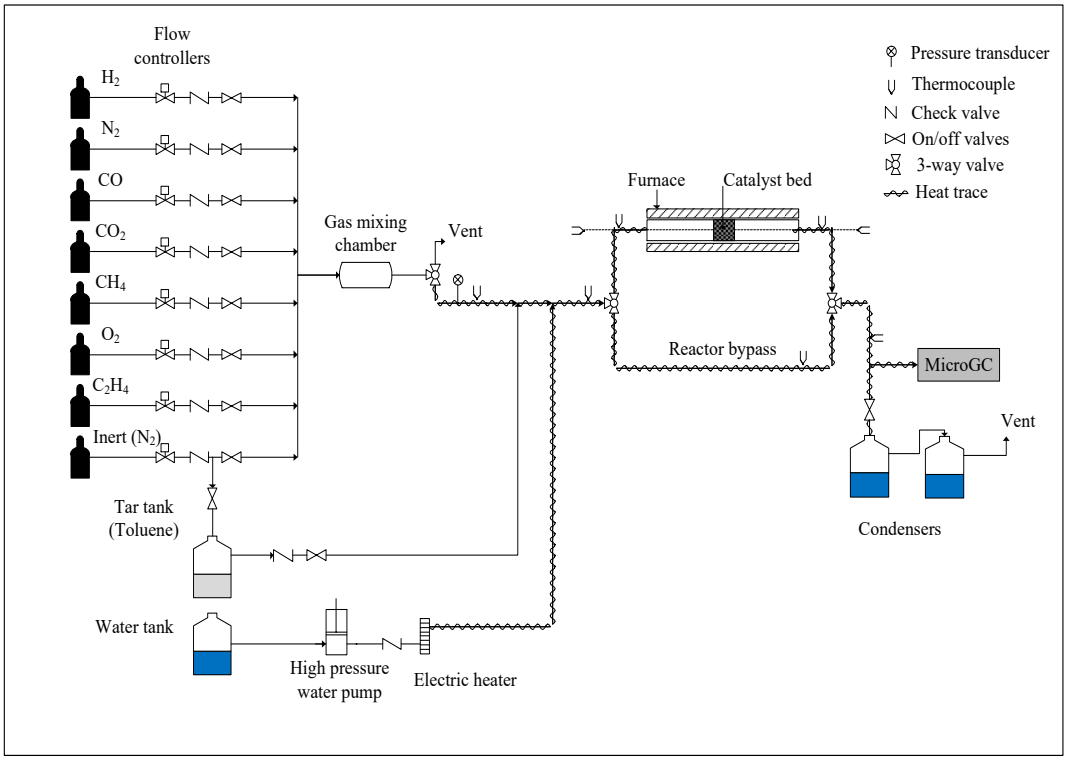

Figure 4.3: Fixed-bed reactor schematic for the production of renewable natural gas from methanation of producer gas.

after the flow reactor methanation were measured with the Agilent 990 micro gas chromatograph (GC).

The methanation experiments were conducted on simulated producer gas with CO and CO_2 at the relative proportions in Table 4.1 with additional hydrogen. CH_4 is not present in the input gases to provide better sensitivity to the methanation production reactions and N_2 is added to provide additional heat capacity to moderate the temperature increase associated with the exothermic methanation reaction. Ethylene (C_2H_4), normally present in producer gas, was not included to prevent coking in the fixed-bed reactor.

The producer gas compositions on a molar basis (%) in the study are summarized in Table 4.1 along with the ratio of $H_2/CO+CO_2$ content on a molar basis. The standard producer gas composition has a low hydrogen/carbon ratio H/C = $H_2/(CO+CO_2)$ = 0.83. The test cases cover from below the standard producer gas hydrogen/carbon ratio up to a maximum of H/C

Table 4.1: Simulated producer gas composition test cases with increased hydrogen and hydrogen/carbon ratio.

Case	H_2 (%)	CO (%)	CO_2 (%)	N_2 (%)	$\frac{H_2}{CO+CO_2}$
Case 1	34.4	36.9	18.7	20	0.75
Case 2	48.0	18.9	13.1	20	1.50
Case 3	53.4	15.7	10.9	20	2.00
Case 4	60.0	11.8	8.2	20	3.00
Case 5	64.0	9.4	6.6	20	4.00

$=H_2/(CO+CO_2)=$ 4.0. The total flow in the experiment was maintained at 400 mL/min with an overall weight hourly space velocity (WHSV) of 96000 scc/hr/g. For overall weight hourly space velocity at 64000 scc/hr/g, the catalyst loading is 375mg with 7.5 g quartz chips.

4.2.2 Fluidized Bed Reactor

The fluidized bed reactor is employed for a variety of multiphase chemical reactions, such as the production of fuels, polymers, and coal gasification, etc. In these reactors, fluid is passed at high velocity through a bed of solid catalyst, suspending the particles and causing them to behave as if they were fluidized. This reactor type offers several advantages over fixed bed reactors. The fluid-like behavior of the catalyst ensures thorough mixing with the gas, promoting uniform temperature gradients and effectively minimizing local hot and cold spots. However, fluidized bed reactors are typically larger than fixed bed reactors, presenting challenges in modeling and understanding their internal dynamics.

Figure 4.4 presents a process flow diagram of a fluidized-bed methanation setup, designed for the production of renewable natural gas through the methanation of producer gas. The system is divided into three main sections. The gas cleaning unit removes sulfur species to low ppb levels, ensuring that the gas stream is sufficiently purified before methanation. The gas generation unit is tasked with the accurate production of the gas stream that supplies the methanation reactor. Finally, the methanation-reaction unit encompasses the main fluidized-bed reactor, which is equipped with an axial sampling unit and a temperature control unit, among other components.

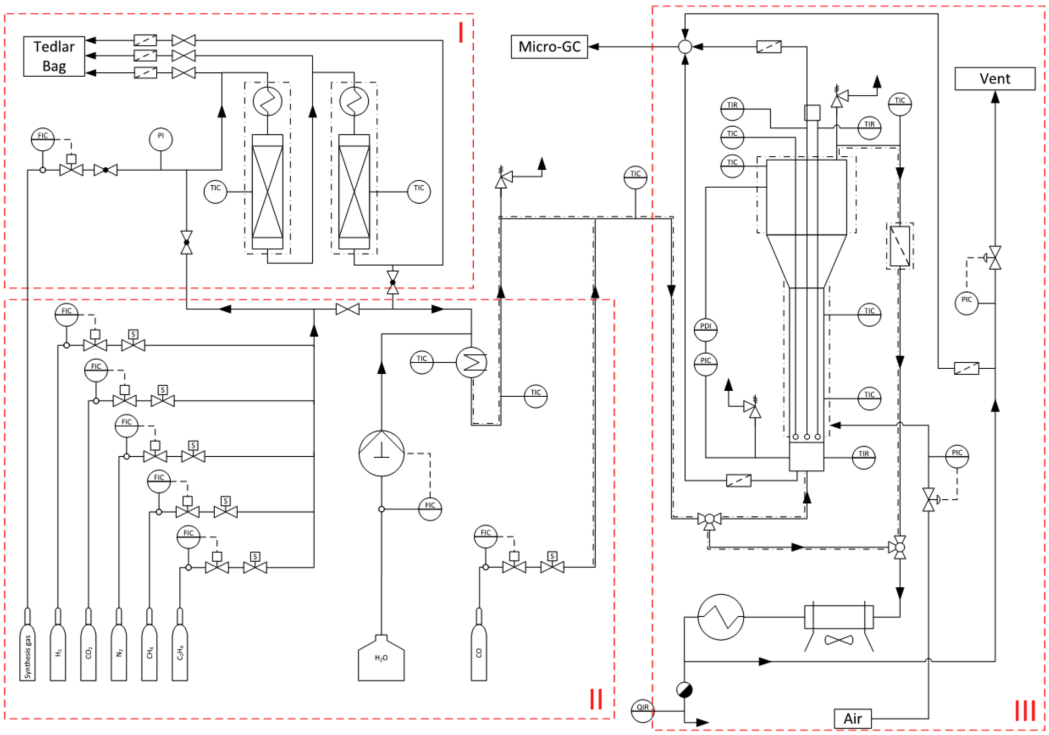

Figure 4.4: Schematic of a fluidized-bed reactor for the production of renewable natural gas from the methanation of producer gas. The setup consists of a gas cleaning unit (I), gas-generation unit (II), and methanation-reaction unit(III) [100]

Further specifications of the fluidized-bed reactor are detailed here [101]

The methanation reactor tube contained 1.5 g of the Ni/Ru/MgO catalyst on the Sasol Puralox 300/200 alumina and mixed with 100 g non-catalytic Puralox 300/130. The higher density of the uncoated Puralox 300/130 is a closer match to the Puralox 300/200 that has been coated with the catalyst. Gas composition before and after the flow reactor methanation was measured with Agilent 3000 micro gas chromatograph (GC).

The methanation experiments were conducted on CO and CO_2 at the relative proportions as in the fixed-bed experiments following Table 4.2 with additional hydrogen. As previously noted, no CH_4 is present to provide sensitivity to the methanation reactions and N_2 is added to provide additional heat capacity to moderate the temperature increase associated with the exothermic methanation reaction. Ethylene (C_2H_4) was not included in the fixed-bed experiments to prevent coking but was added to the fluidized-bed experiments in some test to examine the

Table 4.2: Volumetric flow rates (L/min) of gases used in the fluidized-bed methanation experiments with increased hydrogen and hydrogen/carbon ratio with total flow 2.4 L/min.

Case	H_2	CO	CO_2	N_2	$\frac{H_2}{CO+CO_2}$
Case 1	0.825	0.646	0.449	0.480	0.75
Case 2	1.153	0.452	0.314	0.480	1.50
Case 3	1.281	0.377	0.262	0.480	2.00
Case 4	1.440	0.283	0.197	0.480	3.00
Case 5	1.536	0.226	0.157	0.480	4.00

Table 4.3: Volumetric flow rates (L/min) of gases used in the fluidized-bed methanation experiments with increased hydrogen and hydrogen/carbon ratio with total flow 2.4 L/min (C_2H_4)

Case	H_2	CO	CO_2	C_2H_4	N_2	$\frac{H_2}{CO+CO_2}$	$\frac{H_2+2\times C_2H_4}{CO+CO_2+2\times C_2H_4}$
Case 1	0.825	0.646	0.449	0.045	0.435	0.75	0.77
Case 2	1.153	0.452	0.314	0.031	0.449	1.50	1.47
Case 3	1.281	0.377	0.262	0.026	0.454	2.00	1.93
Case 4	1.440	0.283	0.197	0.020	0.460	3.00	2.85
Case 5	1.536	0.226	0.157	0.016	0.464	4.00	3.78

effect.

The volumetric flows used in the fluidized-bed methanation study are presented in Table 4.2 along with the molar ratio of H_2/(CO+CO_2). The test cases cover the hydrogen/carbon ratio from 0.75 to a maximum of 4.0. The total flow in the experiment was maintained at 2.4 L/min with an overall weight hourly space velocity (WHSV)96000 scc/hr/g. The molar fraction of tested gases and WHSV are identical to the initial fixed bed experiments.

The volumetric flows used in the fluidized-bed methanation study are presented in Table 4.3 along with the molar ratio of H_2/(CO+CO_2). The test cases cover the hydrogen/carbon ratio from 0.75 to a maximum of 4.0. The total flow in the experiment was maintained at 2.4 L/min with an overall weight hourly space velocity (WHSV) of 96000 scc/hr/g, identical to the initial fixed bed experiments.

The following expression was used to investigate the performance of catalysts for methanation. The percent conversion for a reactant *A* is calculated as:

$$Conversion_{[A]}(\%) = \left[\frac{mass_A^{in} - mass_A^{out}}{mass_A^{in}}\right] \times 100 \tag{4.3}$$

where $mass_A$ denotes the mass flow rate of reactant A in g/s.

The yield of methane is calculated as:

$$\mathrm{CH_4^{yield}}(\%) = \left[\frac{mass_{\mathrm{CH_4}}^{out}/Mw_{CH_4}}{mass_{CO}^{in}/Mw_{CO} + mass_{CO_2}^{in}/Mw_{CO_2} + 2 \times mass_{C_2H_4}^{in}/Mw_{C_2H_4}}\right] \times 100 \tag{4.4}$$

where $mass_{\mathrm{CO}}^{in}$, $mass_{\mathrm{CO_2}}^{in}$, $mass_{\mathrm{C_2H_4}}^{in}$ denote the inlet mass flow of CO, CO_2 and C_2H_4, in g/s. $mass_{\mathrm{CH_4}}^{out}$ is the outlet mass flow of CH_4. Mw is the molecular weight.

The ethane yield relative to ethylene is defined as:

$$\mathrm{C_2H_6^{yield}}(\%) = \left[\frac{mass_{\mathrm{C_2H_6}}^{out}/Mw_{\mathrm{C_2H_6}}}{mass_{\mathrm{C_2H_4}}^{in}/Mw_{\mathrm{C_2H_4}}}\right] \times 100 \tag{4.5}$$

where $mass_{\mathrm{C_2H_6}}^{out}$ the mass flow rate of ethane at the outlet and $mass_{\mathrm{C_2H_4}}^{in}$ is the mass flow rate of ethylene at the inlet.

The selectivity of CH_4, CO_2, CO in terms of carbon are calculated as:

$$\mathrm{CH_4^C}(\%) = \left[\frac{mol_{\mathrm{CH_4}}^{out}}{mol_{\mathrm{CH_4}}^{out} + mol_{\mathrm{CO}}^{out} + mol_{\mathrm{CO_2}}^{out}}\right] \times 100 \tag{4.6}$$

$$\mathrm{CO_2^C}(\%) = \left[\frac{mol_{\mathrm{CO_2}}^{out}}{mol_{\mathrm{CH_4}}^{out} + mol_{\mathrm{CO}}^{out} + mol_{\mathrm{CO_2}}^{out}}\right] \times 100 \tag{4.7}$$

$$\mathrm{CO^C}(\%) = \left[\frac{mol_{\mathrm{CO}}^{out}}{mol_{\mathrm{CH_4}}^{out} + mol_{\mathrm{CO}}^{out} + mol_{\mathrm{CO_2}}^{out}}\right] \times 100 \tag{4.8}$$

where $mol_{\mathrm{CH_4}}^{out}, mol_{\mathrm{CO_2}}^{out}, mol_{\mathrm{CO}}^{out}$ denote the molar flow of CH_4, CO_2 and CO in products, in mol/s.

The selectivity of CH_4, H_2, H_2O in terms of hydrogen are calculated as:

$$CH_4^H(\%) = \left[\frac{4 \times mol_{CH_4}^{out}}{4 \times mol_{CH_4}^{out} + 2 \times mol_{H_2}^{out} + 2 \times mol_{H_2O}^{out}}\right] \times 100 \quad (4.9)$$

$$H_2^H(\%) = \left[\frac{2 \times mol_{H_2}^{out}}{4 \times mol_{CH_4}^{out} + 2 \times mol_{H_2}^{out} + 2 \times mol_{H_2O}^{out}}\right] \times 100 \quad (4.10)$$

$$H_2O^H(\%) = \left[\frac{2 \times mol_{H_2O}^{out}}{4 \times mol_{CH_4}^{out} + 2 \times mol_{H_2}^{out} + 2 \times mol_{H_2O}^{out}}\right] \times 100 \quad (4.11)$$

where $mol_{CH_4}^{out}, mol_{H_2}^{out}, mol_{H_2O}^{out}$ denote the molar flow of CH_4, H_2 and H_2O in products, in mol/s.

4.3 Results and Discussion

4.3.1 Results of Fixed-Bed Methanation at WHSV = 96000 scc/hr/g

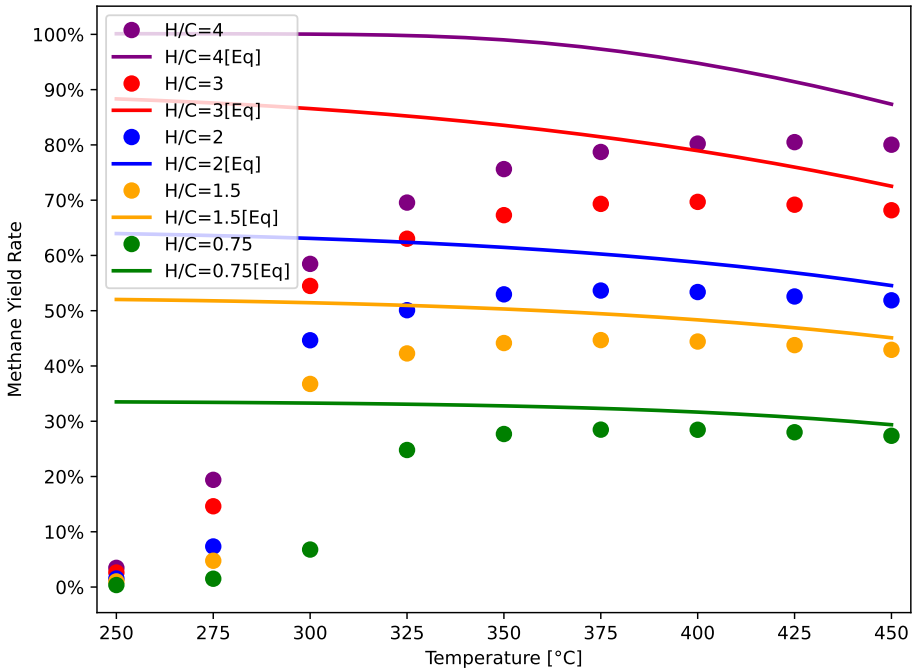

Figure 4.5: Methane yield from the methanation of CO and CO_2 in simulated producer gas as a function of reactor temperature and increased H_2 compared to equilibrium model. The symbols represent experiments and lines are simulations

The methane yield from fixed-bed methanation experiments with 250 mg of catalyst from producer gas CO and CO_2 with increasing the hydrogen/carbon ratio is presented in Figure 4.5. The numerical results are calculated based on chemical equilibrium model. At H/C= 0.75 for the methanation of the CO and CO_2 the methane yield is 28.5% at a temperature of 400 °C. This result compares to the chemical equilibrium value of 31.7%. As the H/C ratio is increased to 4.0 the methane yield is increased to 80.2% at 400 °C compared to a chemical equilibrium value of 94.8%. Under all conditions the measured methane yield is below the potential chemical equilibrium yield. Although approaching the equilibrium value at the lowest H/C=0.75, the departure from equilibrium yield increases with increasing H/C.

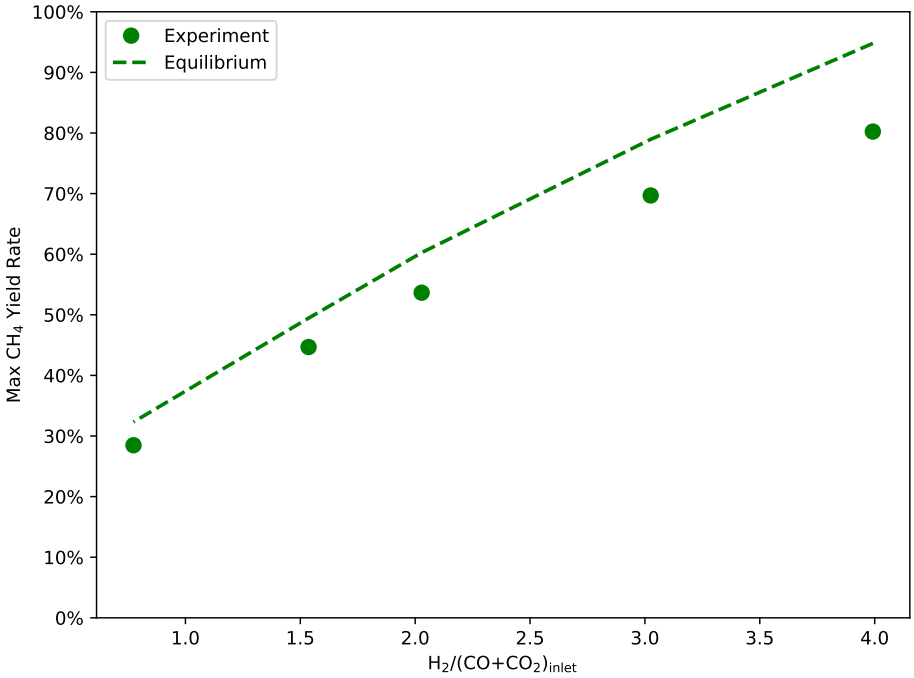

Figure 4.6: Methane yield from the methanation of CO and CO_2 as a function of increased H_2 compared to equilibrium model. The symbols represent experiments and line is the equilibrium yield.

The maximum methane yield, as a function of temperature and H/C ratio from experimental measurements and chemical model results is presented in Figure 4.6. At the weight hourly space velocity WHSV = 96000 scc/hr/gm the measured methane yield is below the chemical equilibrium model value over the entire range of increasing hydrogen/carbon ratio. The

corresponding reactor temperature is almost around 400 °C.

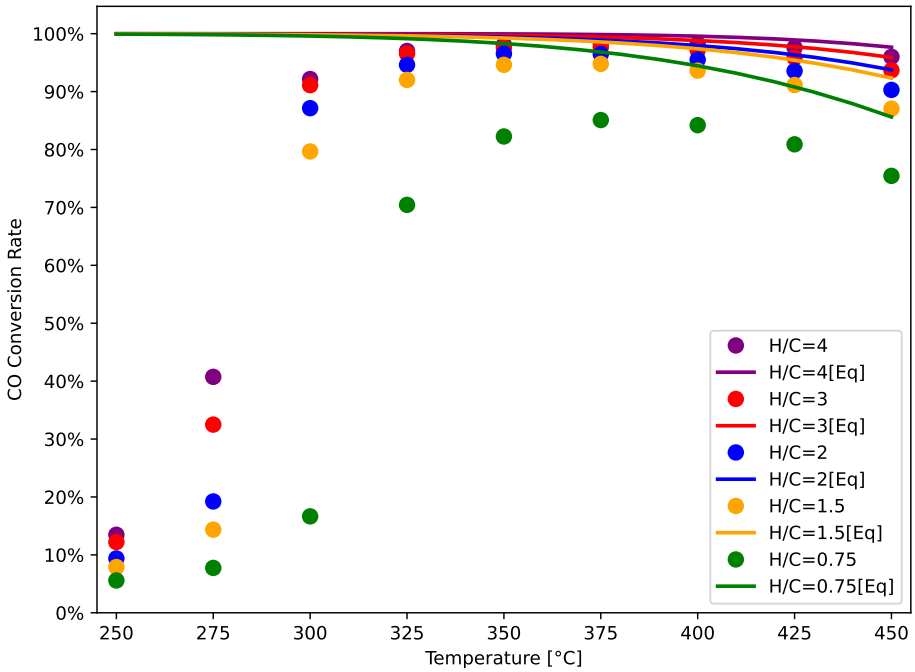

Figure 4.7: CO conversion as a function of reactor temperature and increased H/C ratio compared with chemical equilibrium model. The symbols represent experiments and lines are simulations.

The conversion of CO in the catalytic methanation process is shown in Figure 4.7. At the lowest hydrogen/carbon (H/C) ratio of 0.75, the maximum CO conversion reached 85% at 375 °C, compared to a chemical equilibrium conversion of 97%. As the H/C ratio increased, so did the CO conversions. At the highest H/C ratio of 4.0, the maximum CO conversion was 98.4% at 375 °C, which is near the equilibrium value of 99.5%. Under all tested conditions, the experimental CO conversion remained below the theoretical chemical equilibrium values. It is important to note that not all converted CO contributed to CH_4 production; some was also converted to CO_2 through the water-gas shift reaction 4.12.

$$CO + H_2O \Longleftrightarrow H_2 + CO_2 \qquad \Delta H_{298\,K} = -41\,\text{kJ/mol} \tag{4.12}$$

The conversion of CO_2 in the catalytic methanation process is illustrated in Figure 4.8. Using simulated producer gas at the lowest H/C ratio of 0.75, the CO_2 conversion was net

negative, at -39.7% at 400 °C, primarily due to the conversion of CO to CO_2. No net positive conversion of CO_2 was observed until the H/C ratio exceeded 2.0. At the highest H/C ratio of 4.0, the CO_2 conversion peaked at 65% at 400 °C. Without significant hydrogen addition (H/C $>$ 2.0) to the producer gas, the conversion of CO_2 does not contribute to net methane production. Below an H/C ratio of 2.0, CO_2 conversion remains negative and falls short of reaching potential chemical equilibrium conversion levels. Conversely, above an H/C ratio of 2.0, although CO_2 conversion becomes positive, it still does not achieve the potential chemical equilibrium conversion.

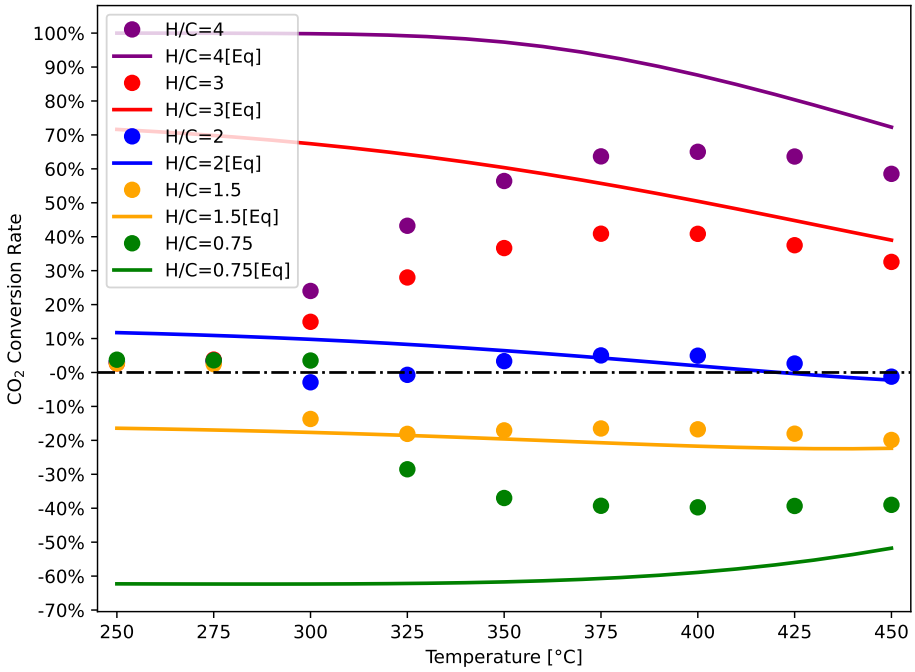

Figure 4.8: CO_2 conversion as a function of reactor temperature and H/C ratio compared to chemical equilibrium model. The symbols represent experiments and lines are simulations.

In addition to the CO_2 removal by methanation, the water-gas shift reaction 4.12 can generate CO_2 from the water produced by the methanation reactions 4.1 and 4.2. At high hydrogen/carbon (H/C) ratios, the abundant presence of H_2 helps to suppress the production of CO_2 from the water-gas shift reaction.

The conversion of H_2 as a function of temperature is displayed in Figure 4.9. The highest

H_2 conversion observed was 87% at a temperature of 375 °C, and an H/C ratio of 0.75. Under all tested conditions, the experimental H_2 conversion remains below the potential chemical equilibrium values. At the highest H/C ratio of 4.0, the conversion was 68.3%, with a significant presence of H_2 in the methanation product gas stream.

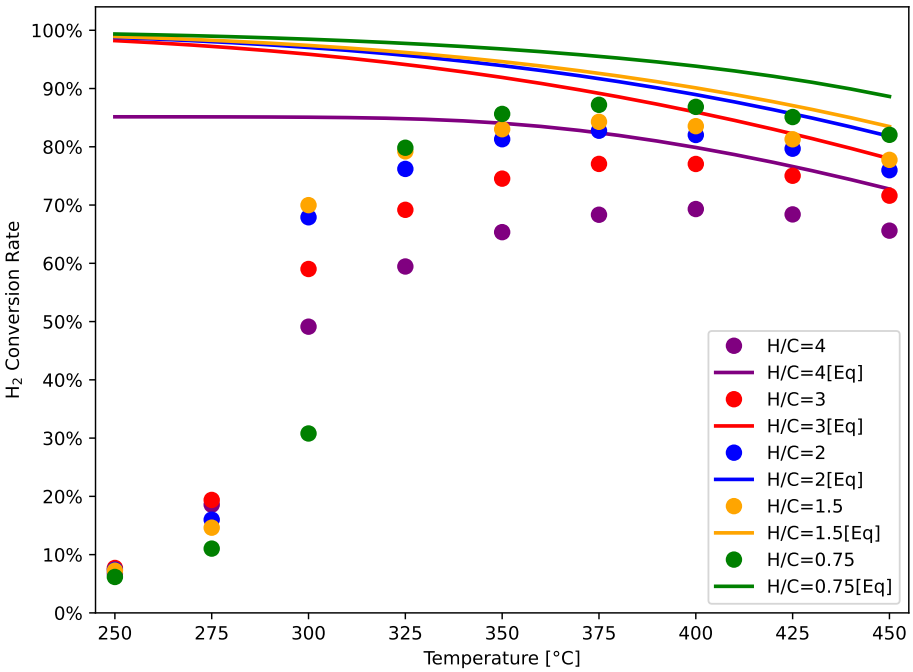

Figure 4.9: H_2 conversion as a function of temperature and H/C ratio for the methanation of CO and CO_2 and comparison with a chemical equilibrium model. The symbols represent experiments and lines are simulations.

The selectivity of carbon during the methanation process in terms of the CO_2 and CH_4 is presented in Figure 4.10 as function of temperature and H/C ratio. The highest selectivity to CH_4 and least to CO_2 occurs at highest H_2 addition at H/C=4.0 and a temperature of 400 °C. The lowest selectivity to CH_4 and highest selectivity to CO_2 occurs at the lowest H_2 addition at H/C=0.75.

The selectivity of CO in the methanation process is presented in Figure 4.11 . At all H/C ratios the CO is above the potential chemical equilibrium levels. At that highest H/C = $H_2/(CO+CO_2)$ = 4.0 ratio the selectivity level for CO was 1% with the remaining carbon in CO_2 and CH_4 in Figure 4.10.

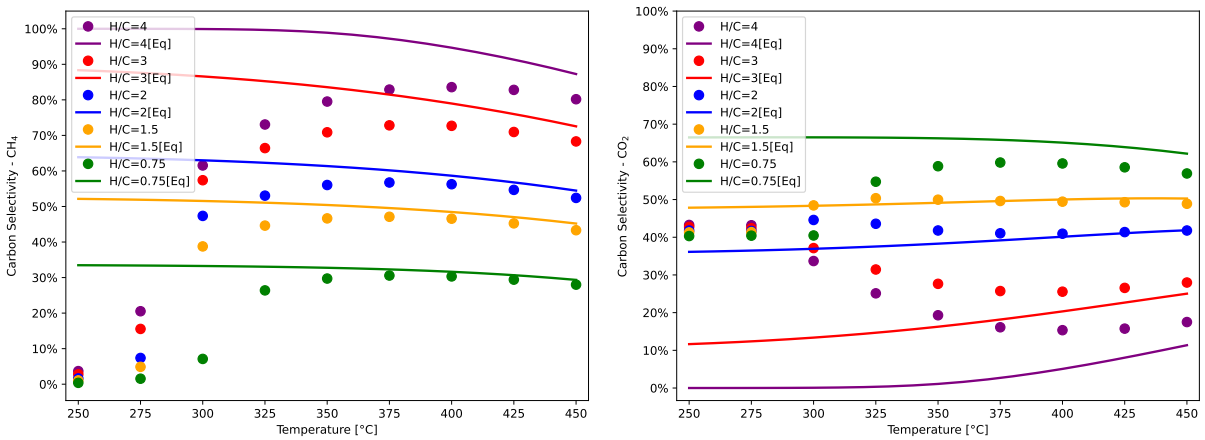

(a) CH_4 **(b)** CO_2

Figure 4.10: Selectivity of CO_2 and CH_4 during methanation of CO and CO_2 as a function of temperature and H/C ratio. The symbols represent experiments and lines are simulations.

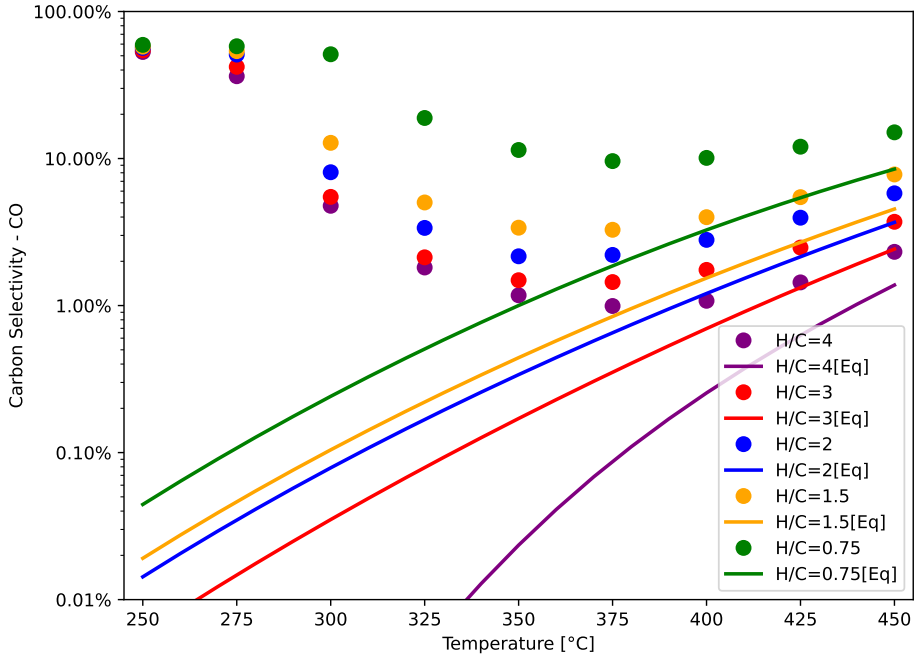

Figure 4.11: Selectivity of CO in the methanation process with increasing H/C ratio and temperature. The symbols represent experiments and lines are simulations.

The removal of CO is essential for upgrading methanation gas to pipeline quality; therefore, the quantity of residual CO remaining in the product stream is a critical consideration. Furthermore, water will be extracted via condensation before the CO removal process. The concentrations of CO in the product stream, both with and without water removal, are shown

in Figure 4.12 . Minimum CO content in methanation product gas is 0.21 % and with water removal 0.27% at H/C =4.0 at a temperature of 375°C.

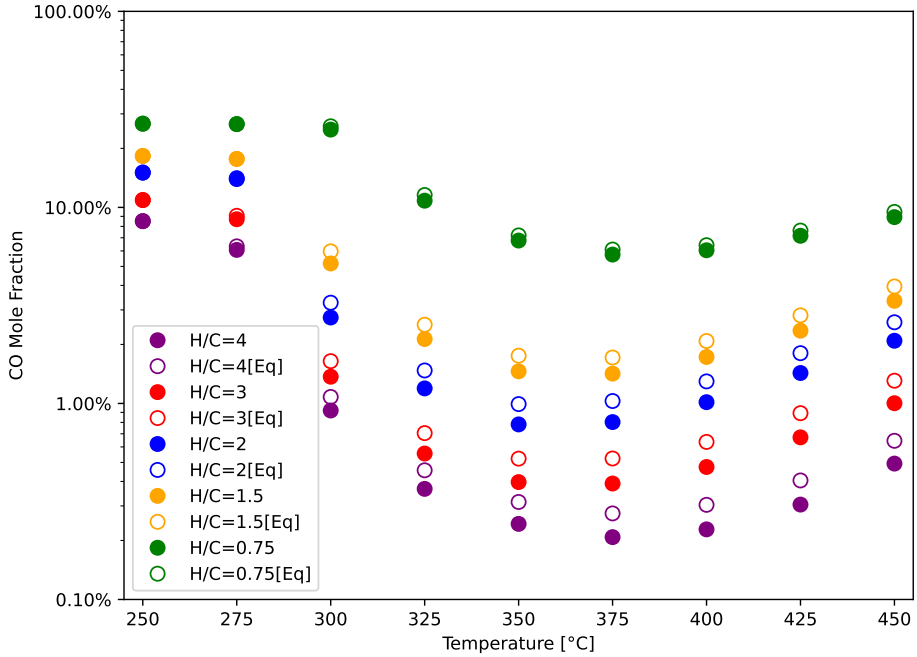

Figure 4.12: CO molar fraction in methanation product gas with and without water removal. The solid symbols represent experimental data without water removal; The hollow symbols represent experimental data with water removal

The removal of residual CO from the primary methanation product gas stream is often accomplished using a secondary methanation process. Consequently, it is crucial to understand the H_2 content of the methanation product gas both with and without water removal, as this affects decisions regarding secondary methanation or recycling back to the primary methanation. This information is critical for optimizing the efficiency and sustainability of the methanation process.

The H_2 concentration in the product gas both with and without water removal is presented in Figure 4.13. Specifically, at an H/C ratio of 4.0 and a temperature of 375°C, the H_2 content is 27.9% without water removal and increases to 34.9% with water removal. At a lower H/C ratio of 0.75, which is close to the standard producer gas H/C ratio of 0.83, the H_2 content in the product stream is 6.45%. Remarkably, this concentration remains nearly unchanged with the

removal of water.

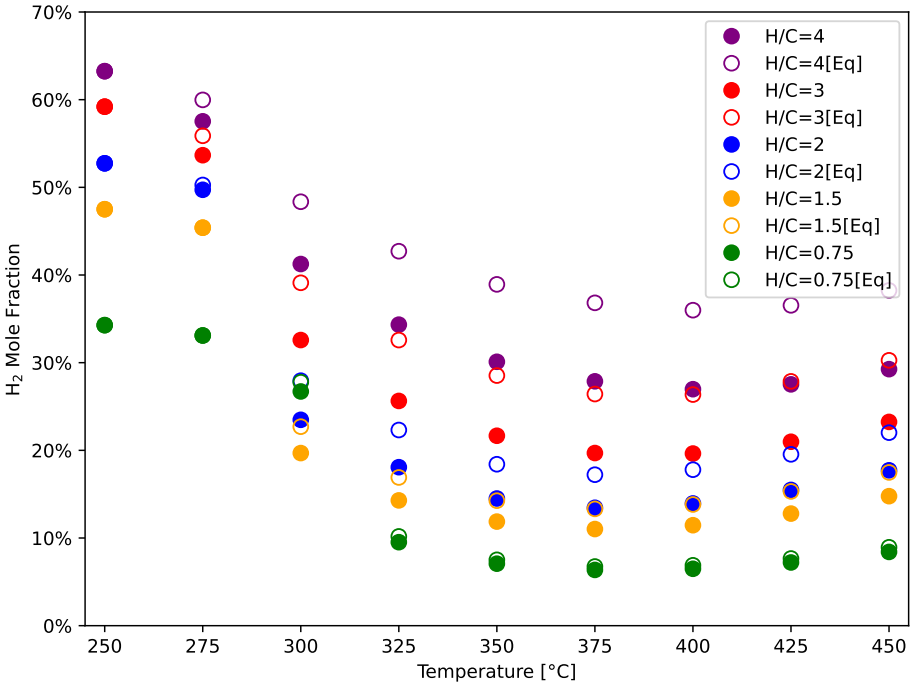

Figure 4.13: H_2 in methanation product gas with and without water removal. The solid symbols represent experimental data without water removal; The hollow symbols represent experimental data with water removal

In summary of fixed bed methanation at 96000 scc/hr/g, the methanation yield from the combined CO and CO_2 in producer gas at 400 °C is 28.5% at an H/C ratio of 0.75, increasing to a maximum of 80.2% at an H/C of 4.0. CO conversion at 375 °C reaches 85% at H/C=0.75 and peaks at 98.4% at H/C=4.0. Conversely, CO_2 conversion at 400 °C starts at -39.8% at H/C=0.75 and reaches up to 65% at H/C=4.0. Notably, CO_2 does not contribute to the net methanation yield until the H/C ratio exceeds 2.0. The minimum CO content in the methanation product gas is 0.21% and increases slightly to 0.27% with water removal at H/C=4.0 and 375°C. At the same conditions,the H_2 content in the methanation product stream is 27.9%, which rises to 34.9% with water removal. Overall, the methanation yield remains below chemical equilibrium values, with the discrepancy widening as the H/C ratio is increased to 4.0. This suggests that at a Weight Hourly Space Velocity (WHSV) of 96000 scc/hr/g, there may not be enough active sites

available to accommodate the additional hydrogen needed to enhance the methanation reactions at higher H/C ratios.

4.3.2 Results of Fixed-Bed Methanation at WHSV = 64000 scc/hr/g

To improve the methane yield reaching equilibrium for the Ni/Ru/MgO catalyst, the fixed-bed methanation experiments were repeated with a 50% increase in catalyst loading, raising the amount to 375 mg. To preserve the same dilution ratio, the loading of quartz chips was also increased to 7.5 g. As a result, the weight hourly space velocity (WHSV), defined as the ratio of the mass flow rate of feed to the mass of the catalyst within the reactor, decreased from 96000 scc/hr/g to 64000 scc/hr/g. The performance of the increased catalyst loading (1.5X) on the methanation CO and CO_2 with increasing hydrogen/carbon ratio for the simulated producer gas for the compositions listed in Table 4.1 is presented in Figure 4.14 .

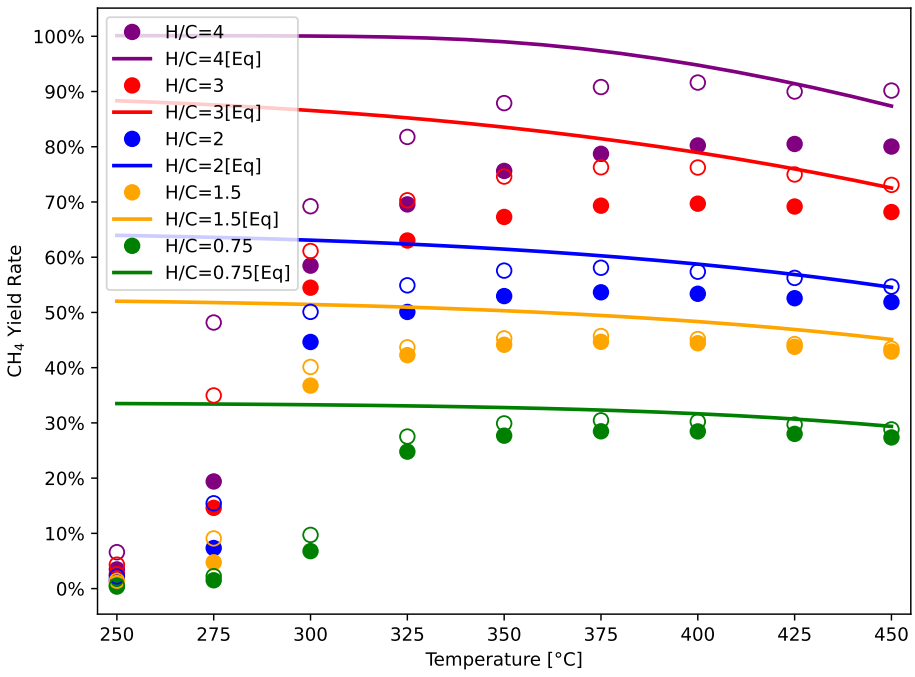

Figure 4.14: Methane yield from producer gas at 1.0X and 1.5X catalyst loading as a function of reactor temperature and increased H/C ratio and comparison to equilibrium model. The symbols represent experiments and lines are simulations. Solid symbols denote a catalyst loading of 1.0X, and hollow symbols represent a 1.5X loading.

At H/C= 0.75 for the methanation of CO and CO_2 the methane yield is 30.2% at a temperature of 400°C. This result compares to the chemical equilibrium value of 31.7%. As the H/C ratio is increased to 4.0 the methane yield is increased to 91.6% at 400 °C compared to a chemical equilibrium value of 94.8%. Under all conditions the measured methane yield with the 50% increase in catalyst loading is improved over the base catalyst loading (1.0X) in Figure 4.14 for all H/C ratios and most improved at the highest H/C= 4.0.

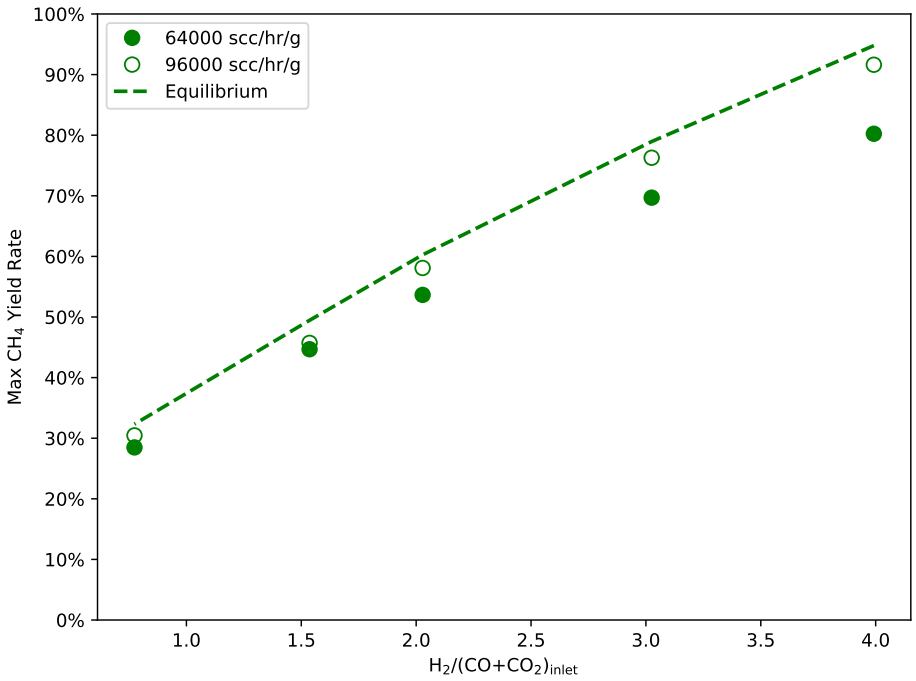

Figure 4.15: Methane yield at 400 °C from the methanation of simulated producer gas at 1.0X and 1.5X catalyst loading with decreased WHSV from 96000 to 64000 scc/hr/g as a function of H/C ratio compared to equilibrium model. The symbols in the figure represent experimental data, while the lines indicate simulation results. Solid symbols denote a catalyst loading of 1.0X, and hollow symbols represent a 1.5X loading.

The methane yield at 400 °C as a function of H/C ratio from measurements at both WHSV = 96000 and 64000 scc/hr/g and chemical equilibrium results is are presented in Figure 4.15. With the decrease in the weight hourly space velocity to WHSV = 64000 scc/hr/gm, the methane yield with the increased catalyst loading (1.5X) approaches the equilibrium yield over the range of H/C, particularly improving the performance at the highest H/C ratio. The

enhancement in methane yield becomes more pronounced as the H/C ratio increases.

Conversion of CO in catalytic methanation with 1.5X catalyst loading is presented in Figure 4.16 . At the lowest H/C ratio (0.75) the maximum CO conversion was increased to 93.2% from 85% at 375 °C and compares to an equilibrium CO conversion of 97%. The CO conversion increased with increasing hydrogen/carbon ratio. At the highest hydrogen/carbon ratio (4.0) the CO conversion was increased to 99.3% from 98.4% at 375 °C and compares to the equilibrium value of 99.5%. The improvement in CO conversion with increased catalyst loading is more pronounced at lower H/C ratios but becomes limited at higher ratios.

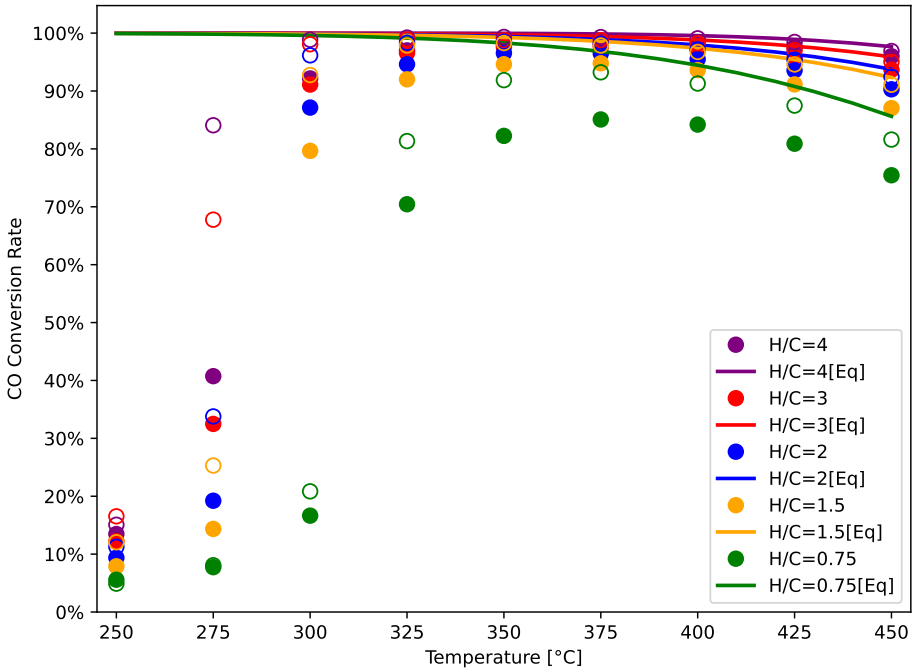

Figure 4.16: CO conversion as a function of reactor temperature with 1.5X increased catalyst loading and increased H/C ratio compared with chemical equilibrium model. The symbols in the figure represent experimental data, while the lines indicate simulation results. Solid symbols denote a catalyst loading of 1.0X, and hollow symbols represent a 1.5X loading.

The conversion of CO_2 in catalytic methanation using a 1.5X catalyst loading is displayed in Figure 4.17. Increasing the catalyst loading proves beneficial for achieving chemical equilibrium results at temperatures of no less than 400 °C. At the highest H/C ratio of 4.0, the CO_2 conversion reached a maximum of 81.8% at 400 °C, compared to 65% with the 1.0X loading. At

the lowest H/C ratio of 0.75, the CO_2 conversion decreased from -39.7% to -49.3% at 400 °C, which is closer to the equilibrium model prediction of -58.9%. No net positive conversion of CO_2 is observed until the H/C ratio exceeds 2.0, consistent with results using the 1.0X catalyst loading.

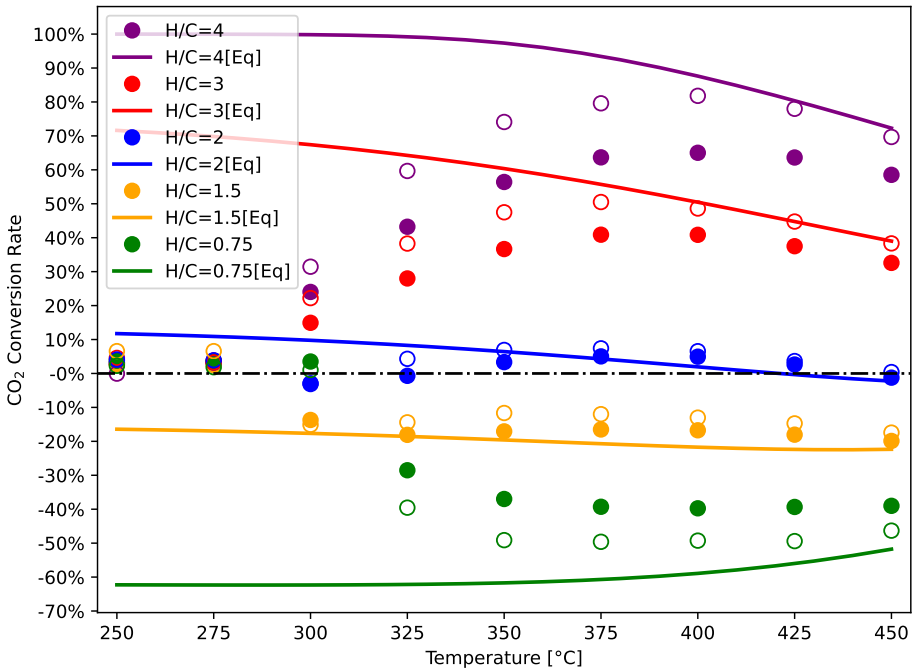

Figure 4.17: CO_2 conversion as a function of reactor temperature with 1.0X and 1.5X catalyst loading and H/C ratio compared to chemical equilibrium model.The symbols in the figure represent experimental data, while the lines indicate simulation results. Solid symbols denote a catalyst loading of 1.0X, and hollow symbols represent a 1.5X loading. Dotted-dashed lines are used to indicate a zero conversion.

Unless a significant amount of hydrogen (H/C $>$ 2.0) is added to the producer gas, the conversion of CO_2 does not contribute to the net production of methane. Below H/C =1.5 and above a H/C=1.5 the CO_2 conversion is closer to the potential equilibrium conversion with the 1.5X catalyst loading compared to the 1.0X loading. In addition to the removal of CO_2 through methanation, the water-gas shift reaction 4.12 can generate CO_2 from the H_2O produced in the methanation process. At higher H/C ratios, the presence of excess H_2 helps suppress the production of CO_2 in the water-gas shift reaction.

The conversion of H_2 as a function of temperature with increased catalyst loading (1.5X) is presented in Figure 4.18 . The maximum H_2 conversion at 1.5X loading was 91.1% at a temperature of 375 °C and a H/C ratio 0.75 and is only slightly higher than the 87.2% conversion at 1.0X. Under all conditions the experimental H_2 conversion is below the potential chemical equilibrium value. The conversion at the highest H/C ratio (4.0) and 1.5X catalyst loading was 71.7% only a slight increase compared to 68.3% at 1.0X with significant H_2 remaining in the methanation product gas.

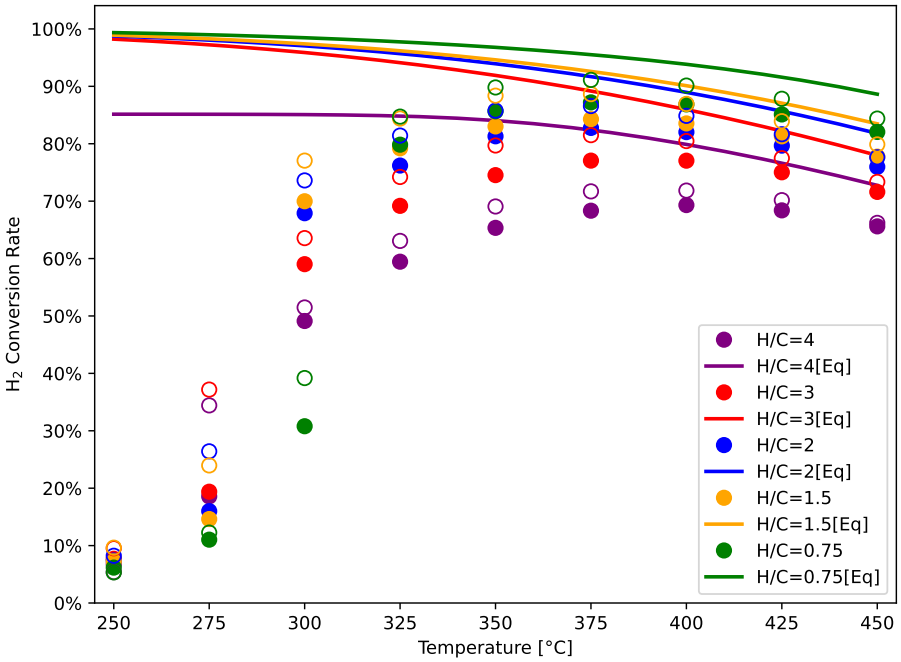

Figure 4.18: Conversion of H_2 as a function of temperature and H/C ratio with 1.5X increased catalyst loading for the methanation of CO and CO_2 compared to chemical equilibrium model. The symbols in the figure represent experimental data, while the lines indicate simulation results. Solid symbols denote a catalyst loading of 1.0X, and hollow symbols represent a 1.5X loading.

The selectivity of carbon during the methanation process with increased catalyst loading (1.5X) in terms of the CO_2 and CH_4 is presented in Figure 4.19 as function of temperature and H/C ratio. The highest selectivity to CH_4 and least to CO_2 occurs at highest H_2 addition at H/C=4.0 and a temperature of 400°C. The lowest selectivity to CH_4 and highest selectivity to CO_2 occurs at the lowest H_2 addition at H/C=0.75. The increase in catalyst loading improves

attaining the equilibrium levels , particularly at higher H/C ratios.

The selectivity of CO in the methanation process with increased catalyst loading (1.5X) is presented in Figure 4.20 . At all H/C ratios the CO is above the potential chemical equilibrium levels. At that highest $H_2/(CO+CO_2)$ ratio, 4.0, the selectivity level for CO was less than 1% in the range 250°C to 425°C, with the remaining carbon in CO_2 and CH_4 in Figure 4.19.

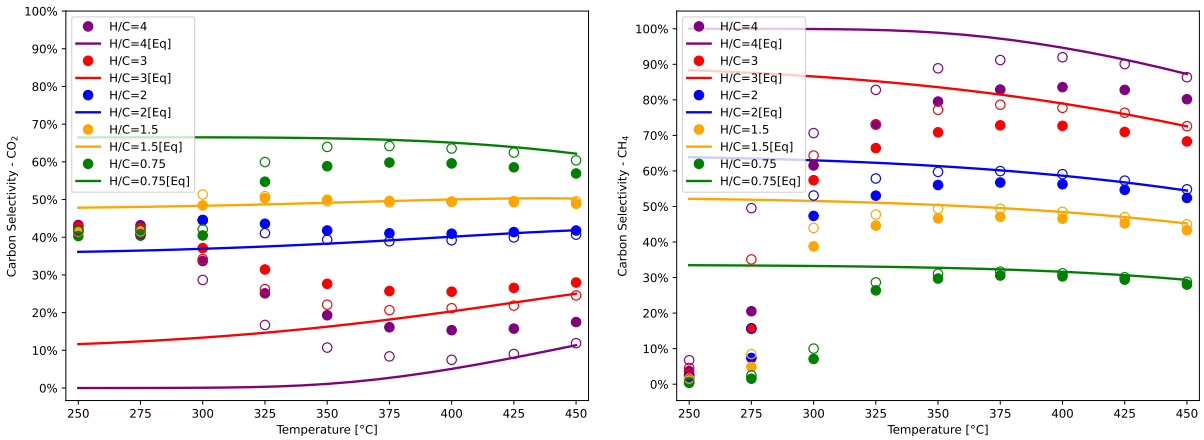

(a) CO_2 **(b)** CH_4

Figure 4.19: Selectivity of CO_2 and CH_4 during methanation of CO and CO_2 at 1.5X catalyst loading as a function of temperature and H/C ratio. The symbols in the figure represent experimental data, while the lines indicate simulation results. Solid symbols denote a catalyst loading of 1.0X, and hollow symbols represent a 1.5X loading.

The selectivity of hydrogen towards CH_4(a), H_2O(b), and H_2(c) in the methanation product gas is depicted in Figure 4.21. At the lowest H/C ratio of 0.75, the selectivity towards CH_4 is at its highest, correlating with the minimum selectivity of H_2O and H_2 in the methanation. In contrast, at the highest H/C ratio of 4.0, the selectivity towards CH_4 is at its minimum, while the concentrations of H_2O and H_2 are at their maximum. This pattern suggests that a higher percentage of hydrogen atoms preferentially form hydrogen gas at higher H/C ratios, whereas at lower H/C ratios, they are more likely to form CH_4. Consequently, excessive input of hydrogen results in a lower coefficient of its utilization.

The removal of residual CO from the primary methanation product gas may necessitate a secondary methanation process. It is therefore essential to assess the CO and H_2 contents

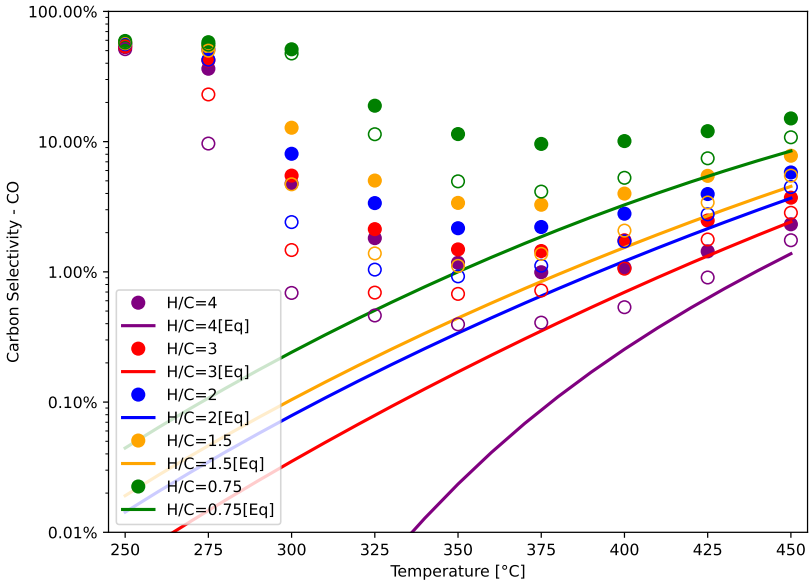

Figure 4.20: Selectivity of CO in the methanation process at 1.5X catalyst loading with increasing H/C ratio and temperature. The symbols in the figure represent experimental data, while the lines indicate simulation results. Solid symbols denote a catalyst loading of 1.0X, and hollow symbols represent a 1.5X loading.

in the methanation product gas both with and without water removal, to facilitate decisions about secondary methanation or recycling back to the primary process. Figure 4.22 displays the concentrations of CO and H_2 in the product gas under these conditions. At an H/C ratio of 4.0 and a temperature of 375°C, the H_2 mole fraction increases from 23% to 33% with water removal, while the CO mole fraction rises from 0.08% to 0.12%. At a lower H/C ratio of 0.75, the H_2 content marginally increases from 4.4% to 4.6% with water removal, and the CO mole fraction increases from 2.5% to 2.7%, showing minimal change consistent with results using 1.0X catalyst loadings.

In summary, the investigation of fixed-bed methanation at 64000 scc/hr/g reveals several key findings: The methanation yield increases with a 1.5X increase in catalyst loading, particularly at higher H/C ratios, due to the additional active sites available on the catalyst surface. Specifically, at 400 °C, the methane yield increases from 80% to 91.6% at an H/C ratio of 4.0. Compared to a WHSV of 96000 scc/hr/g, the methanation yield at 64000 scc/hr/g is closer to the

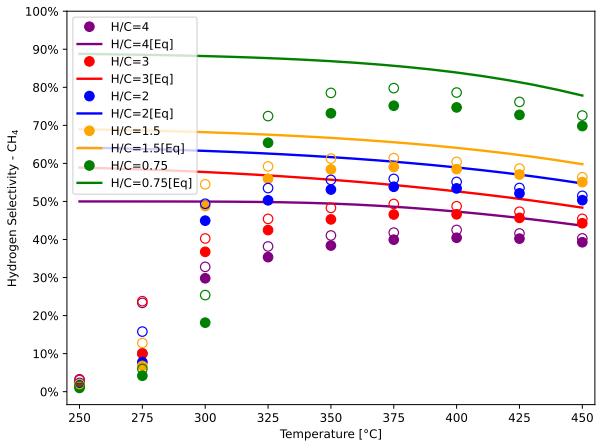

(a) CH_4

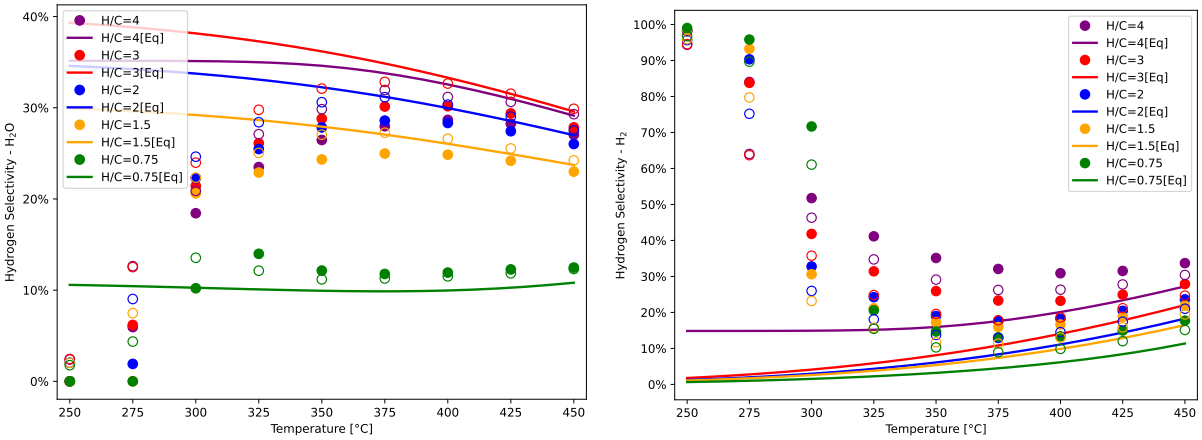

(b) H_2O **(c)** H_2

Figure 4.21: Hydrogen selectivity to (a) CH_4, (b) H_2O, and (c) H_2 in the methanation ouput gas. The symbols represent experiments and lines are simulations. Solid symbols denote a catalyst loading of 1.0X, and hollow symbols represent a 1.5X loading.

chemical equilibrium prediction for temperatures above 400 °C. Furthermore, CO conversion improvement at 64000 scc/hr/g is more notable at an H/C ratio of 0.75, increasing from 85% to 93% at 375 °C, while being limited at higher H/C ratios. Additionally, at this WHSV, there is no net CO_2 contribution to the methanation yield until the H/C ratio exceeds 2.0, consistent with findings at 96000 scc/hr/g. For H/C ratios above 2.0, CO_2 conversion increases with enhanced catalyst loading at 400 °C, whereas for ratios below 2.0, the conversion decreases, approaching

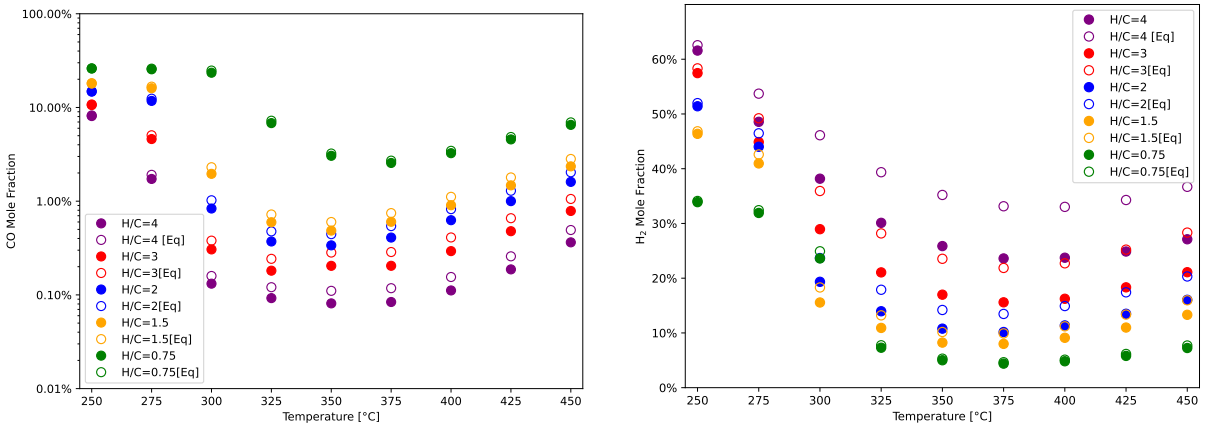

(a) CO **(b)** H_2

Figure 4.22: CO and H_2 concentrations in methanation product gas with and without water removal. Symbols in the figures represent experimental data, while lines indicate simulation results. Solid symbols denote a catalyst loading of 1.0X, and hollow symbols represent a 1.5X loading.

chemical equilibrium due to the water-gas shift reaction. Lastly, the H_2 and CO content in the methanation product stream, both with and without water removal at an H/C ratio of 4.0 and a temperature of 375°C, are slightly lower than those observed with 1.0X loading.

4.3.3 Results of Fluidized-Bed Methanation WHSV = 96000 scc/hr/g

In this section, the performance of the catalyst for the methanation of the CO and CO_2 with additional hydrogen experiments was investigated in fluidized bed reactor.

The methane yield from fluidized-bed methanation experiments on producer gas CO and CO_2 with increasing the hydrogen/carbon ratio is depicted in Figure 4.23. At an H/C ratio of 0.75, the methane yield from the methanation of CO and CO_2 is 17.4% at a temperature of 400 °C. This yield is significantly lower than the chemical equilibrium value of 31.7%. As the H/C ratio increases to 4.0, the methane yield also rises, reaching 59.6% at 400 °C, yet this still falls short of the chemical equilibrium value of 94.8%. Across all tested conditions, the measured methane yield remains below the potential chemical equilibrium yield.

In contrast to the results observed in a fixed bed reactor, experimental data from a

fluidized bed reactor exhibit a diverging trend when the temperature exceeds 375 °C. Unlike the decreasing trend predicted, the experimental data continue to show an increase. This discrepancy is likely due to differences in temperature measurement methods between the two reactor types. In the fixed bed reactor, temperatures are measured at the head and end of the reactor. However, the actual internal temperature of the reactor may be higher than the measured values due to the heat released in such a confined stationary space.

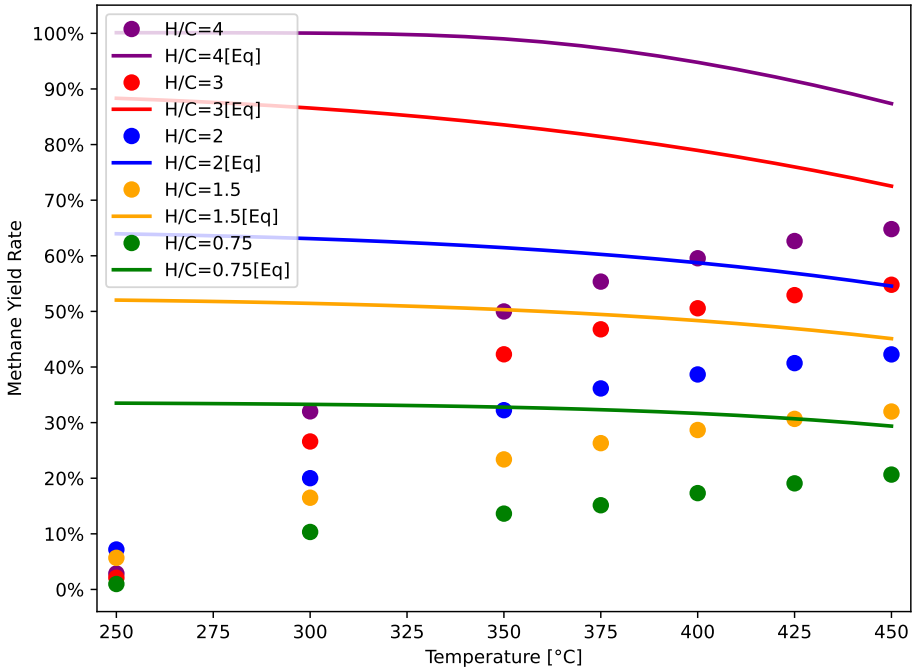

Figure 4.23: Methane yield from the fluidized-bed methanation of CO and CO_2 in producer gas at WHSV =960000 scc/hr/g as a function of reactor temperature and increased H_2 compared to equilibrium model. The symbols represent experiments and lines are simulations.

In the fluidized bed reactor, the recorded temperatures are likely higher than the actual average temperatures within the reactor, due to measurements being taken at only one location within the reactor tube. Specifically, the thermocouple in our experiments is positioned at the top surface of the fluidized bed material when there is no gas flow. Given the relatively large space of the fluidized bed reactor, this single measurement point does not adequately represent the average temperature where reactions are most active. Additionally, the complex temperature distribution within the fluidized bed reactor complicates accurate temperature assessment. Consequently, the

actual temperatures corresponding to those reported in Figure 4.23 are much lower. Therefore, when the figure indicates a temperature of 375 °C, the catalyst is still within its activation temperature range.

The larger discrepancy between experimental and predicted results in the fluidized bed reactor, compared to the fixed bed reactor, possibly be attributed to uneven temperature distribution. In a fixed bed reactor, the catalyst remains stationary uniformly mixed with quartz chips in a confined reactor space , ensuring more uniform temperature conditions. In contrast, the catalyst in a fluidized bed reactor moves within a much larger space, encountering varied temperature zones. Specifically, the catalyst may pass through areas where the temperatures are significantly lower than those measured at the reactor's surface. Additionally, the catalyst loading in the fluidized bed reactor may be insufficient. Although the Weight Hourly Space Velocity (WHSV) is the same for both reactor types, the complex dynamics within the fluidized bed reactor suggest that a different WHSV might be more optimal. As a result, the final product collected at the exit of the fluidized bed reactor often exhibits lower yields compared to that from a fixed bed reactor, reflecting these temperature discrepancies.

The methane yield at 400 °C, as influenced by temperature and hydrogen/carbon (H/C) ratio, is presented in Figure 4.24 from experimental measurements and equilibrium results for both fixed-bed and fluidized-bed methanation at a WHSV of 96000 scc/hr/g. The methane yield measured in the fixed-bed setup remains below the chemical equilibrium values across all H/C ratios. Meanwhile, the yields from the fluidized-bed methanation are substantially lower than those of the fixed-bed, indicating a significant deviation from the chemical equilibrium.

The conversion of CO in the fluidized-bed methanation process is presented in Figure 4.25. At the lowest hydrogen/carbon (H/C) ratio of 0.75, the maximum CO conversion achieved is 55.5% at 450 °C, which is significantly below the equilibrium conversion of 85.6%. As the H/C ratio increases, so does the CO conversion; at the highest H/C ratio of 4.0, the CO conversion peaks at 80.6% at 450 °C, still under the equilibrium value of 97%. Across all conditions, the measured CO conversion remains below the chemical equilibrium values and is notably lower

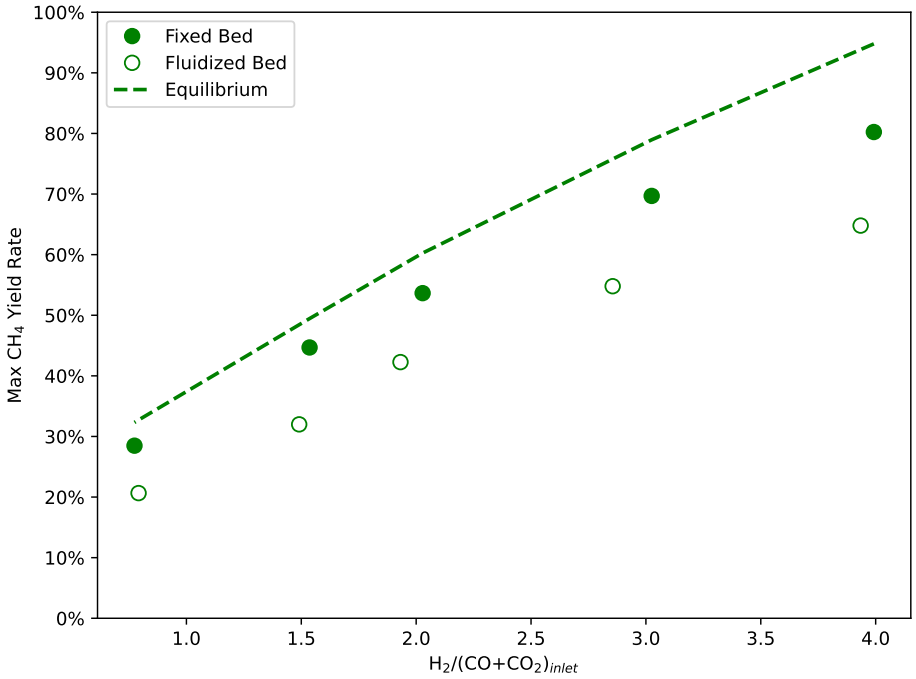

Figure 4.24: Methane yield at 400 °C from the methanation of CO and CO_2 in producer gas in fixed-bed and fluidized-bed reactors at WHSV=96000 scc/hr/gm and an equilibrium model as a function of increased H_2. The symbols represent experiments and lines are simulations.

than the results observed in the fixed-bed process, as shown in Figure4.6 . Additionally, not all the CO that is converted contributes to CH_4 production; a portion is also converted to CO_2 via the water-gas shift reaction 4.12.

The conversion of CO_2 in the fluidized-bed methanation process is illustrated in Figure 4.26. For gas at the lowest H/C = 0.75 ratio the CO_2 conversion was net negative, -18.9% at 450 °C and was the result of the conversion of CO to CO_2. No net positive conversion of CO_2 occurs until the H/C ratio is increased above 2.0 which is consistent with the fixed-bed results in Figure 4.8. At the highest H/C ratio (4.0) the CO_2 conversion was 42.9% at 450 °C. Unless significant hydrogen (H/C >2.0) is added to the producer gas the conversion of CO_2 contributes no net production of methane. Below H/C =2.0 the CO_2 conversion is negative but does not reach the potential chemical equilibrium conversion. Above a H/C=2.0 ratio the CO_2 conversion is positive and also does not reach the potential chemical equilibrium conversion. In addition to CO_2 removal by methanation, the water-gas shift reaction 4.12 will produce CO_2 from the water

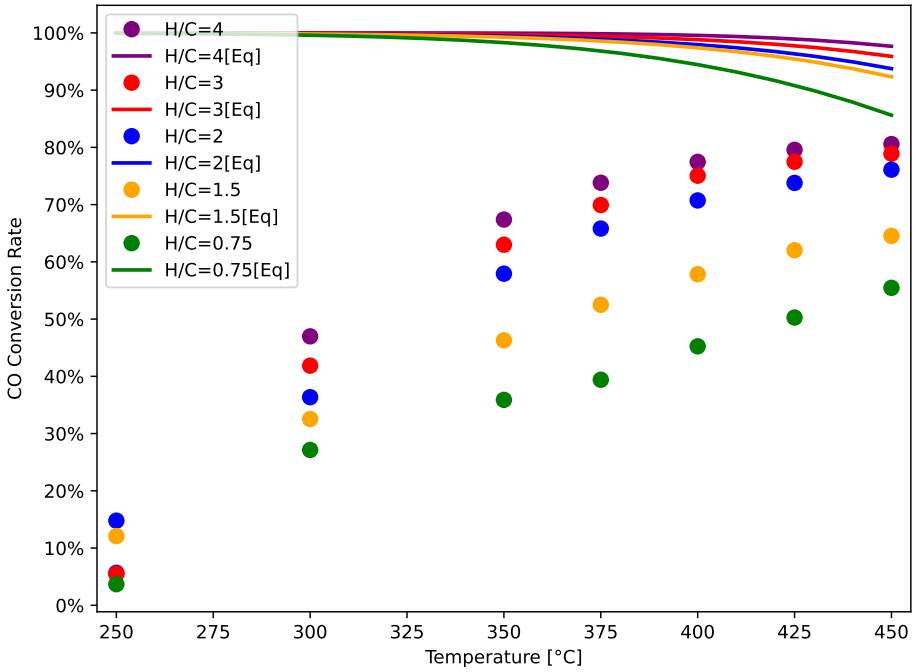

Figure 4.25: CO conversion as a function of fluidized-bed temperature and increased H/C ratio compared with chemical equilibrium model. The symbols represent experiments and lines are simulations.

produced from the methanation reaction. The water-gas shift reaction significantly influences the expected equilibrium conversion of CO_2. Additionally, the catalytic activity for this reaction in the fluidized bed reactor appears to be much lower than that for methanation. This discrepancy is largely attributed to the uneven temperature distribution within the fluidized bed reactor and the potential overestimation of the reactor's temperature.

At high H/C ratio the presence of excess H_2 helps to suppress the production of CO_2 from the water gas shift reaction. The conversion of CO_2 in the fluidized-bed methanation reactor at the same WHSV(960000 scc/hr/gm) is substantial reduced compared to fixed-bed methanation.

The conversion of H_2 as a function of temperature is illustrated in Figure 4.27. The highest observed H_2 conversion, 68%, occurred at a temperature of 450 °C. Under all experimental conditions, the H_2 conversion remains below the potential chemical equilibrium values. Notably, the conversion peak typically observed in fixed-bed reactors around 450 °C is absent in this figure.

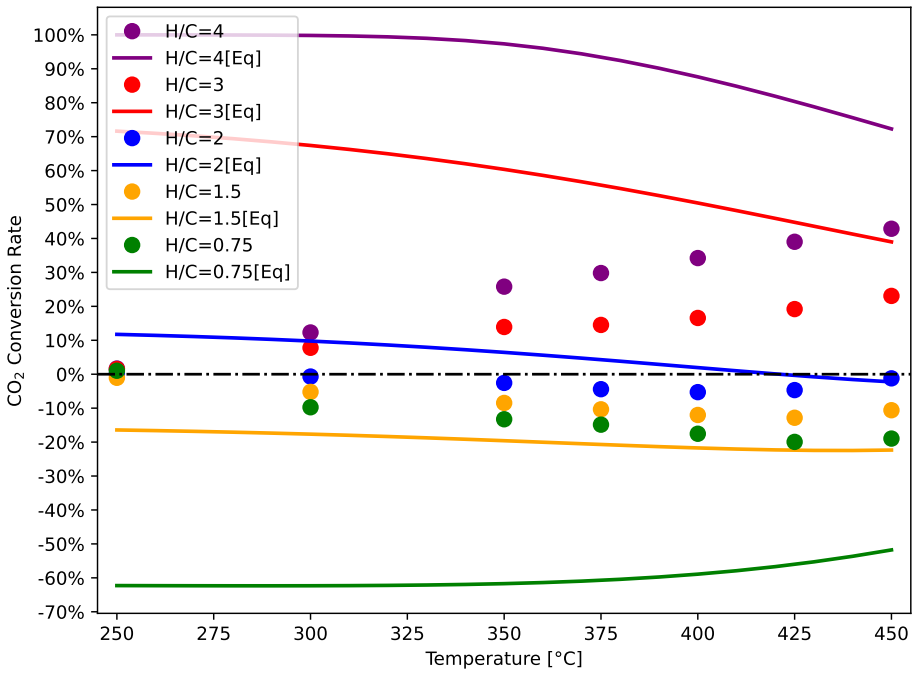

Figure 4.26: CO_2 conversion in fluidize-bed methanation reactor as a function of reactor temperature and H/C ratio compared to chemical equilibrium model. The symbols represent experiments and lines are simulations.

The selectivity of carbon during the methanation process, specifically regarding CO_2 and CH_4, is illustrated in Figure 4.28 as a function of temperature and H/C ratio. The highest selectivity towards CH_4 and the lowest towards CO_2 are observed at the highest H_2 addition, corresponding to an H/C ratio of 4.0 and a temperature of 450 °C. Conversely, the lowest selectivity to CH_4 and the highest selectivity to CO_2 occur at the minimal H_2 addition, at an H/C ratio of 0.75.

The selectivity of CO in the fluidized-bed methanation process is depicted in Figure 4.29. For all H/C ratios, the selectivity for CO remains above the potential chemical equilibrium levels. At the highest H/C ratio of $H_2/(CO+CO_2) = 4.0$, the selectivity level for CO reaches around 10%, with the remaining carbon distributed between CO_2 and CH_4. This is substantially higher than the 1% CO selectivity observed in the fixed-bed methanation results, which are presented in Figure 4.11.

In summary, an investigation of methanation under a fluidized-bed reactor operating

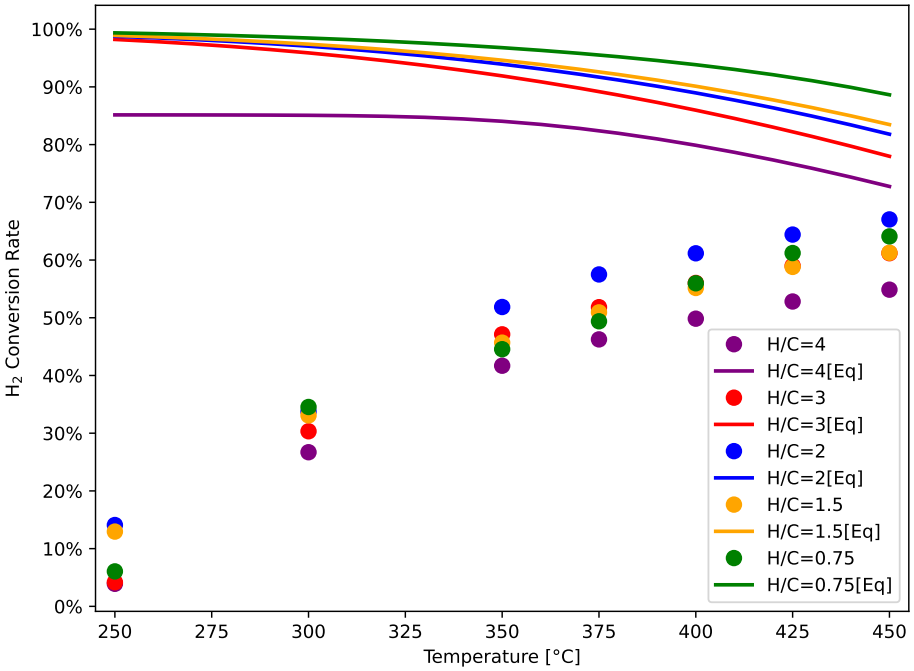

Figure 4.27: Conversion of H_2 as a function of temperature and H/C ratio for the fluidized-bed methanation of CO and CO_2 and comparison with a chemical equilibrium model. The symbols represent experiments and lines are simulations.

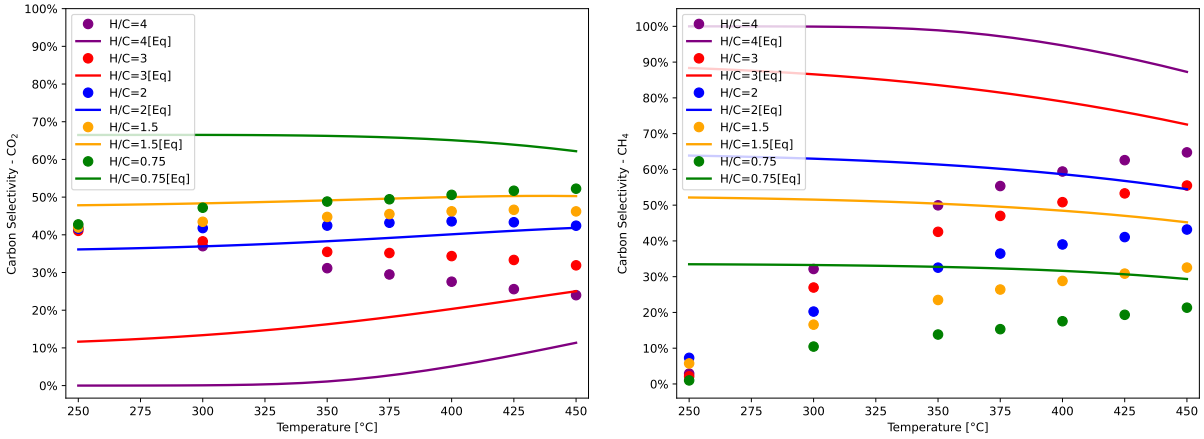

(a) CO_2 **(b)** CH_4

Figure 4.28: Selectivity of CO_2 and CH_4 during fluidized-bed methanation of CO and CO_2 as a function of temperature and H/C ratio

at 96000 scc/hr/g has yielded several crucial insights: Firstly, the methanation yield from the combined CO and CO_2 in producer gas at 400 °C is 17.4% at an H/C ratio of 0.75, increasing to 59.6% at H/C=4.0. However, these yields remain below chemical equilibrium values, and the

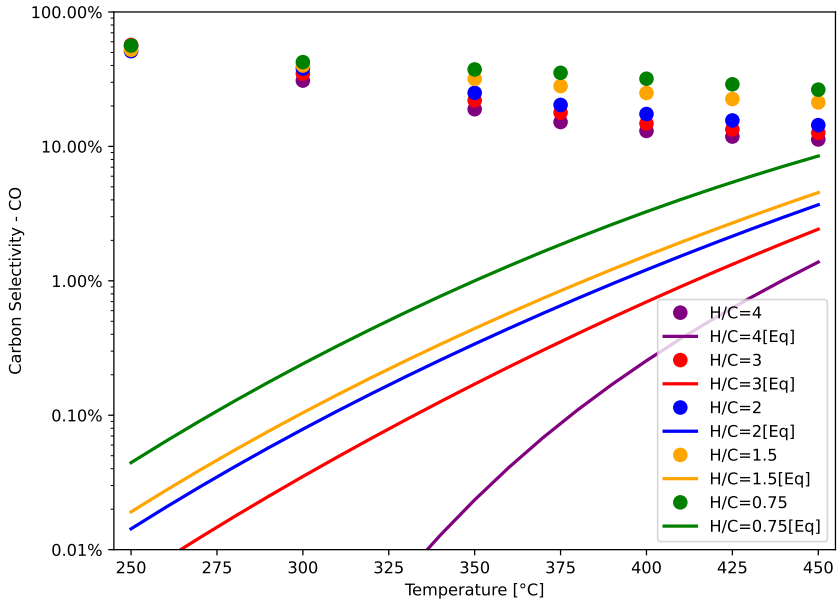

Figure 4.29: Selectivity of CO in the fluidized-bed methanation process with increasing H/C ratio and temperature. The symbols represent experiments and lines are simulations.

gap widens as the H/C ratio increases, with fluidized-bed methanation performance significantly lagging behind that observed in fixed-bed reactors. Specifically, CO conversion at 450 °C is only 55.5% at H/C=0.75, peaking at 80.6% at H/C=4.0. Additionally, CO_2 conversion at the same temperature is -18.9% at H/C=0.75, improving to a maximum of 42.9% at H/C=4.0. Notably, CO_2 does not contribute to the methanation yield until the H/C ratio exceeds 2.0, a finding consistent with those from fixed-bed reactors. At the highest H/C ratio of 4.0, CO_2 selectivity in the fluidized-bed reaches around 10%, significantly higher than the 1% observed in fixed-bed settings. To enhance methanation reaction performance, the fluidized-bed reactor may require substantially higher catalyst loading and a reduction in weight hourly space velocity. Moreover, improving the precision of temperature measurement within the fluidized-bed reactor is crucial for optimizing performance.

4.3.4 Results of Fluidized-Bed Methanation with C_2H_4 at WHSV = 96000 scc/hr/g

In the fixed-bed methanation experiments, ethylene (C_2H_4) was excluded due to its tendency to form coke and deactivate the catalyst. The impact of ethylene on fluidized-bed methanation was explored using a test mixture based on CO and CO_2, in the proportions specified in Table 4.3, with an addition of hydrogen. Notably, no CH_4 was present to affect the sensitivity of the methanation reactions, and N_2 was included to enhance the heat capacity, thereby helping to moderate the temperature increase associated with these exothermic reactions.

The composition of the tested producer gas, which includes a 2% concentration of ethylene—accounting for 10% relative to the CO_2 present—is detailed in Table 4.3. To maintain a constant flow rate during the experiments, the N_2 flow was adjusted downward by an amount equal to the added ethylene flow rate. The test cases examined a range of H/C ratios ($H_2/(CO+CO_2)$) from 0.75 to a maximum of 4.0, based on the CO and CO_2 present. The inclusion of ethylene (C_2H_4) altered the overall H/C ratio, decreasing it for ratios above 1.0 and increasing it for those below 1.0. The total flow rate during the experiments was kept constant at 2.4 L/min, with an overall WHSV of 96000 scc/hr/g, consistent with the previous fluidized-bed experiments.

The methane yield from fluidized-bed methanation experiments and from chemical equilibrium involving CO and CO_2, with and without the addition of ethylene and varying hydrogen/carbon ratios, is illustrated in Figure 4.30. With the addition of ethylene, the methane yield from chemical equilibrium increases for H/C ratios less than 3.0 and marginally decreases for H/C ratios greater than 3.0. At the current catalyst loading (WHSV = 96000 scc/hr/g), the measured methane yield is significantly lower than the potential chemical equilibrium yield across all H/C ratios.

The experimental results shown in Figure 4.30 demonstrate that the presence of ethylene reduces the methane yield at the lowest H/C ratio (0.75). Across a range of H/C ratios from 1.50

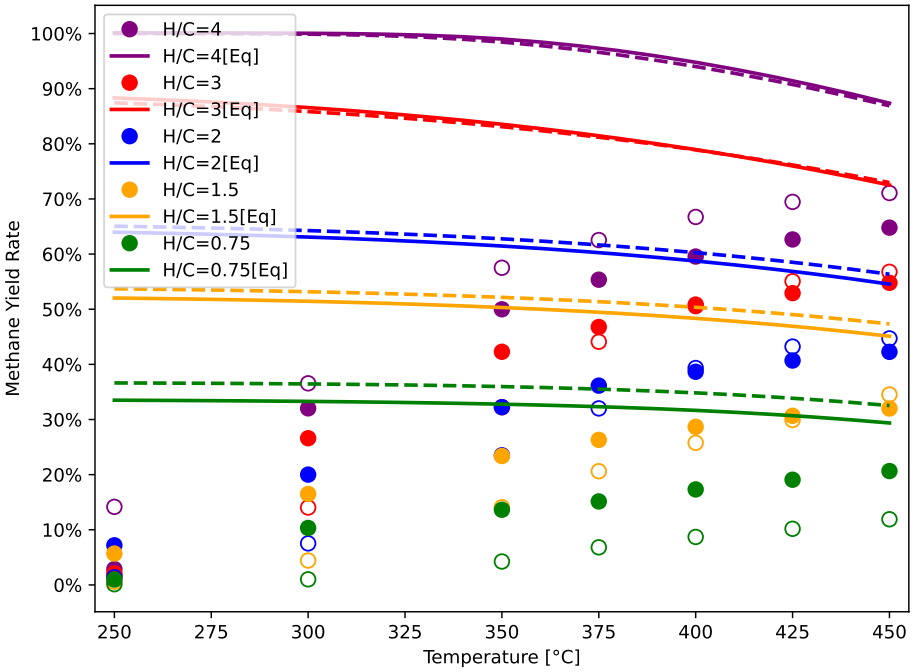

Figure 4.30: Methane yield in the fluidized-bed methanation of CO and CO_2 with and without the presence of ethylene(C_2H_4) as a function of reactor temperature and increased H_2. The symbols represent experiments and lines are simulations. Solid symbols and lines represents excluding C_2H_4 and hollow symbols and dashed lines represent including C_2H_4

to 3.0, the presence of ethylene decreases the methane yield at lower temperatures but matches or exceeds the yield without ethylene at higher temperatures.

At the highest H/C ratio of 4.0, the presence of ethylene enhances the methane yield over a temperature range from 250°C to 450°C. Conversely, at the lowest H/C ratio of 0.75, the methanation of CO and CO_2 results in a maximum methane yield of 20.7% at 450°C. With ethylene present, the yield decreases to 11.9%. However, at the highest H/C ratio of 4.0, the maximum methane yield without ethylene is 64.8% at 450°C, which increases to 71.1% when ethylene is added.

The chemistry of ethylene during the methanation process with H_2 can be explained by reactions 4.13 and 4.14. Ethylene (C_2H_4) reacts with additional H_2 to directly produce CH_4 via reaction 4.14. Additionally, through reaction 4.13, C_2H_4 can be converted into ethane (C_2H_6), which is then further consumed in reaction 4.15. Thus, the addition of C_2H_4 at higher H/C ratios

is beneficial in improving the methane yield.

$$C_2H_4 + H_2 \Longleftrightarrow C_2H_6 \qquad \Delta H_{298\,K} = -139.7\,kJ/mol \tag{4.13}$$

$$C_2H_4 + 2H_2 \Longleftrightarrow 2CH_4 \qquad \Delta H_{298\,K} = -201.86\,kJ/mol \tag{4.14}$$

$$C_2H_6 + H_2 \Longleftrightarrow 2CH_4 \qquad \Delta H_{298\,K} = -64.9\,kJ/mol \tag{4.15}$$

The conversion of ethylene during the methanation experiments is presented in Figure 4.31 . As the temperature and the H/C ratio is increased, ethylene conversion is increased. Over the range of temperature and H/C ratio the chemical equilibrium conversion of ethylene is 100%. The reasons for this difference remain to be investigated.

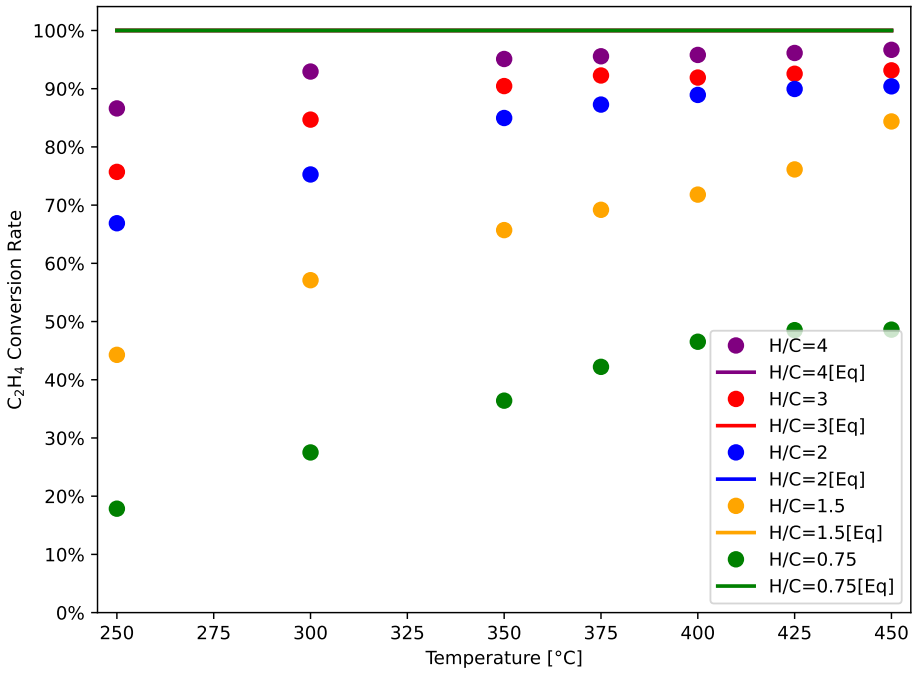

Figure 4.31: The conversion of ethylene (C_2H_4) in fluidized-methanation as a function of reactor temperature and increased H_2 compared to equilibrium model. The symbols represent experiments and lines are simulations.

In the fixed-bed methanation experiments, no ethylene (C_2H_4) is present in output gas. Thus, no ethane (C_2H_6) is formed from reaction 4.13 in our experiments. Thus, it is defined ethane yield as ethane at outlet relative to ethylene at the inlet. In the fluidized-bed experiments, the ethane yield relative to the ethylene initially present in the simulated producer gas (Table 4.3) is illustrated in Figure 4.32.

For H/C ratios less than 3.0, the ethane yield increases as the temperature rises from 250°C to 300°C, then begins to decline at 300°C. This trend is primarily attributed to the catalyst becoming more active and consuming C_2H_6 when the temperature exceeds 300°C.

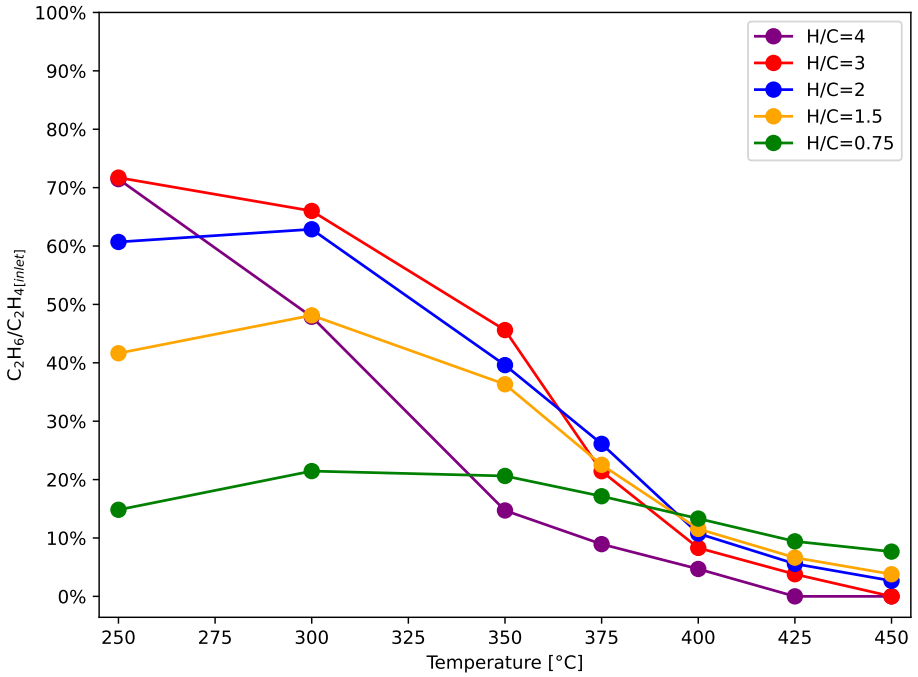

Figure 4.32: Ethane (C_2H_6) yield from ethylene (C_2H_4) as a function of reactor temperature and increased H_2 in the methanation of simulated producer gas

As the temperature exceeds 400°C, the ethane yield decreases with increasing H/C ratios from 0.75 to 4.0. This decrease is because the sufficient hydrogen provided is conducive to converting C_2H_6 to CH_4. At the highest H/C ratio of 4.0, the ethane yield diminishes more rapidly as temperature increase from 250°C to 350°C due to the excess presence of hydrogen, enhancing the conversion of C_2H_6 to CH_4.

In summary, an investigation into methanation incorporating ethylene within a fluidized-bed reactor at a WHSV of 96000 scc/hr/g has revealed several crucial insights. At temperatures above 375 °C, ethylene reduces the methanation yield at the lowest H/C ratio of 0.75. However, for H/C ratios greater than 1.50, the presence of ethylene actually increases the methane yield. Despite this, the methanation yield remains significantly lower than the chemical equilibrium yield across all H/C ratios, a discrepancy partly due to experimental limitations and the inherent characteristics of the fluidized-bed reactor. At the lowest H/C ratio, the ethane yield is minimal and begins to decrease starting at 350 °C, primarily due to methane production and the consumption of hydrogen in methanation reactions. Moreover, as the H/C ratio increases from 1.5 to 3.0, the ethane yield initially rises but then diminishes as the catalyst becomes more effective at temperatures above 350 °C.

4.4 Conclusion

In this chapter, the methanation performance of a Ni-Ru-MgO catalyst was evaluated in a fixed-bed reactor at Weight Hourly Space Velocities (WHSVs) of 96000 scc/hr/g and 64000 scc/hr/g, and the results were compared with chemical equilibrium predictions. It was observed that at temperatures above 375 °C, the experimental data generally followed the equilibrium trends, with performances at 64000 scc/hr/g aligning more closely with these predictions compared to those at 96000 scc/hr/g.

In methanation processes involving producer gas composed of CO and CO_2, lowering the WHSV to 64000 scc/hr/g markedly enhanced the methane yield rate. However, this adjustment had a limited effect on the improvement of CO and H_2 conversion rates. Furthermore, at this lower WHSV, the CO_2 conversion rate improved when the H/C ratio was above 2 but declined below this threshold, largely due to the effects of the water-gas shift reaction. As a result, CO_2 did not contribute to methane production unless the H/C ratio exceeded 2.0.

To achieve chemical equilibrium, it was found necessary to increase the catalyst loading.

Moreover, to ensure effective methane production, an excess of hydrogen is required to counteract the negative effects of the water-gas shift reaction.In summary, considering the activation temperature of the catalyst and the impact of temperature on chemical equilibrium, the optimal conditions for methane production using this catalyst in a fixed-bed reactor were established. With Weight Hourly Space Velocities (WHSV) of 64000 scc/hr/g and 96000 scc/hr/g, the theoretically ideal operational parameters were determined to be approximately 400 °C with a hydrogen/carbon (H/C) ratio of 4.0. Future investigations will aim to explore lower WHSV values than those currently tested to determine if the optimal temperature can be reduced to a value closer to the catalyst's activation temperature.

Additionally, methanation performance was evaluated under a fluidized bed reactor at a WHSV of 96000 scc/hr/g. The performance in the fluidized bed reactor was found to be lower than that observed in the fixed bed reactor, suggesting that the catalyst loading tested was not optimized for the fluidized bed configuration. There is potential that increased loading in the fluidized bed reactor may enhance methantion performance, which remains to be investigated further. The influence of additional C_2H_4 on the methane yield rate was also investigated in the fluidized bed setting. It was found that at temperatures above 375 °C, adding C_2H_4 beneficially increases the methane yield for H/C ratios greater than 1.50, whereas it diminishes the yield at the lowest H/C ratio of 0.75.

Future investigations should focus on enhancing the experimental setup in fluidized bed reactor, particularly by improving temperature measurement and control systems to ensure a more uniform temperature distribution throughout the reactor. Additionally, it would be beneficial to measure the product composition and temperature at various locations inside the reactor to gain a deeper understanding of the reaction dynamics. Moreover, implementing a detailed Computational Fluid Dynamics (CFD) model that includes chemical reactions could provide further insights into the processes occurring within fluidized bed reactors.

Acknowledgements

This chapter, in part, is from coauthored and unpublished material, Renewable Natural Gas Production from Biomass with Power to Gas, by L Ji, R Cattolica. The dissertation author was the primary investigator and author of this material.

Conclusion and outlook

This dissertation has explored the interaction of combustion and optimization of production within the realm of renewable biofuels, focusing on the interactions between biofuels and alkanes, as well as the optimization of biomethane production. Each part of the study has contributed significantly to understanding and enhancing biofuel utilization and production, which are crucial for reducing reliance on traditional fossil fuels and mitigating environmental impacts.

In the initial chapters, our experiments and simulations elucidated how the addition of iso-butanol affects the autoignition temperatures of alkanes, specifically n-decane and n-heptane. Upon further investigation of an ethanol/n-heptane mixture, we discovered that these alcohols inhibit low-temperature chemistry by altering the availability of oxygen and competing reaction pathways. This modification significantly raises the ignition temperature of n-heptane, providing valuable insights into the design of fuel blends that resist premature ignition and enhance engine efficiency.

A significant innovation of this thesis is the development of a novel analytical method inspired by neural network sensitivity analysis, aimed at dissecting the autoignition processes in biofuel blends. This technique effectively pinpointed critical reactive species and elucidated their interactions within various temperature domains. By deepening the understanding of chemical kinetics and species diffusion in reactive flows, this method not only advances analytical approaches in the field of combustion but also opens avenues for more comprehensive models that integrate chemical reactions and species transfer.

In the latter part of the thesis, our focus shifted towards optimizing the methanation

process of biomass producer gas augmented with hydrogen. Through meticulous experimentation, we determined the optimal operational conditions for a Ni-Ru-MgO catalyst in fixed bed reactors. Our findings highlight the importance of operational temperature and hydrogen/carbon ratios in maximizing methanation efficiency and yield. This work contributes to the development of more effective catalytic processes for biomethane production, which is essential for sustainable energy solutions.

The results obtained throughout this dissertation not only advance our understanding of the complex interaction in biofuel combustion but also lay a groundwork for the future commercial production of renewable natural gas. In terms of combustion, future studies should continue to explore the inhibition mechanisms uncovered here to determine their universality across other alkanes and biofuels. Regarding biomethane production, subsequent investigations will aim at developing commercial-scale processes in fluidized bed reactors, significantly advancing the production of sustainable energy.

Appendix A

Supplementary Materials

A.1 Concentration Analysis Results

A.1.1 n-Heptane Dominant Mixtures

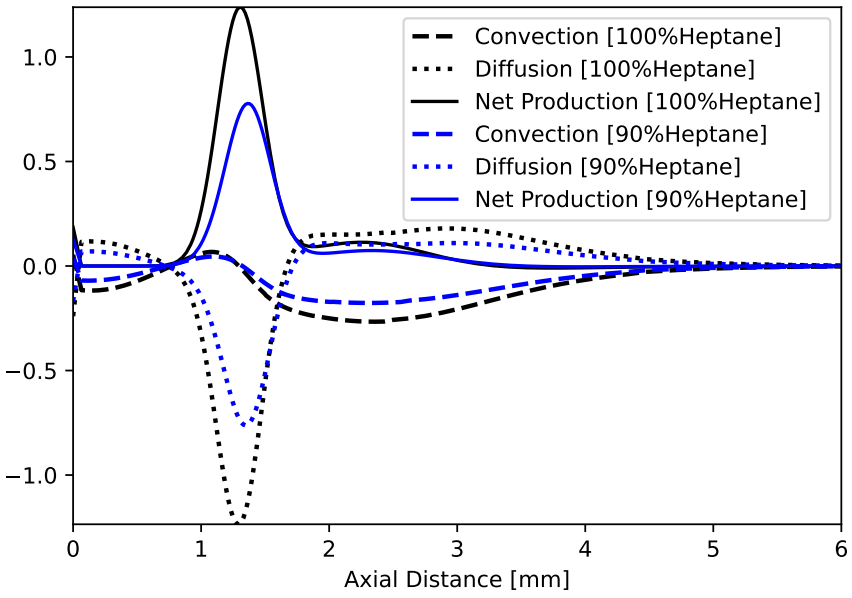

Figure A.1: C_2H_4 species equation terms (n-heptane dominant mixtures)

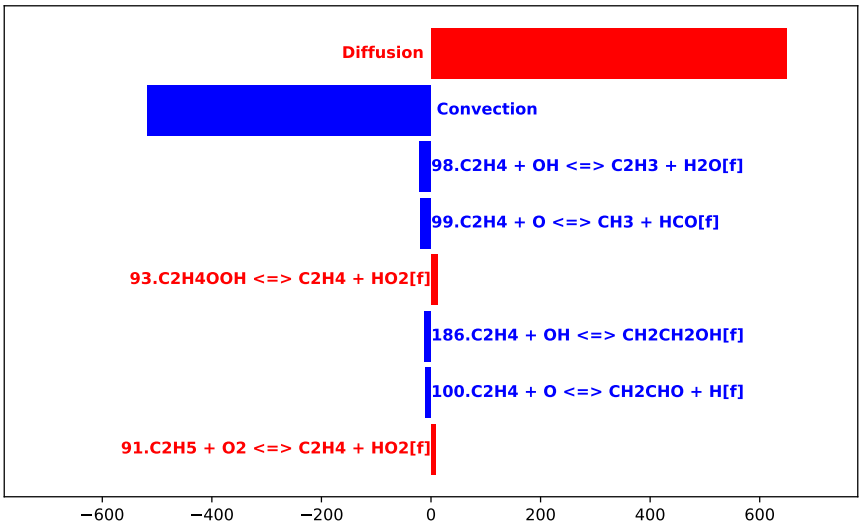

Figure A.2: Contribution on C_2H_4 concentration change @4.2mm

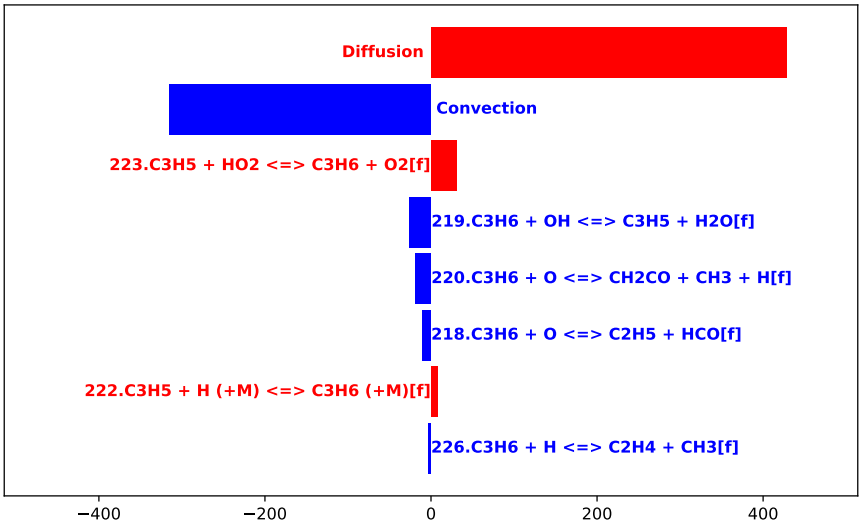

Figure A.3: Contribution on C_3H_6 concentration change @4.2mm (n-heptane dominant mixtures)

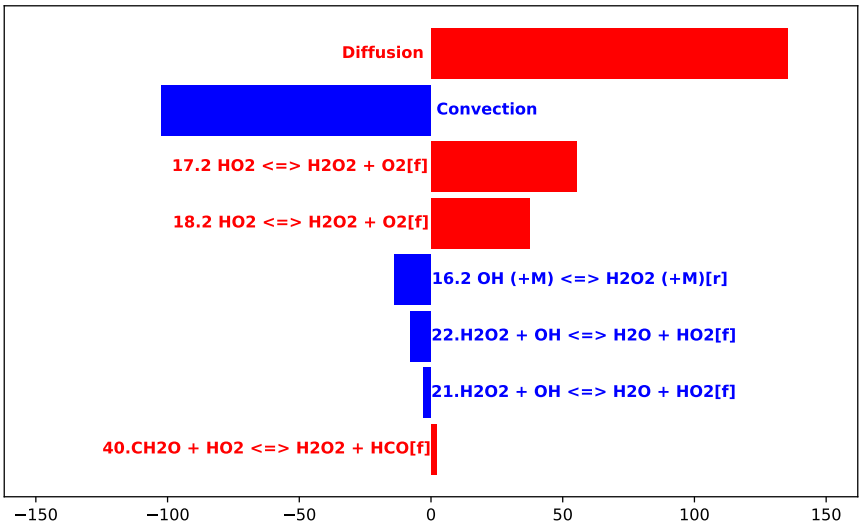

Figure A.4: Contribution on H_2O_2 concentration change @4.2mm (n-heptane dominant mixtures)

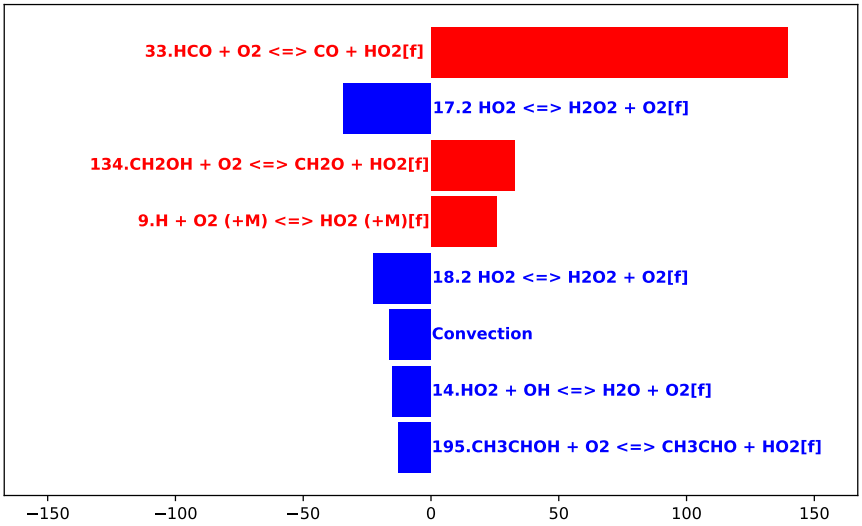

Figure A.5: Contribution on HO_2 concentration change @4.2mm (n-heptane dominant mixtures)

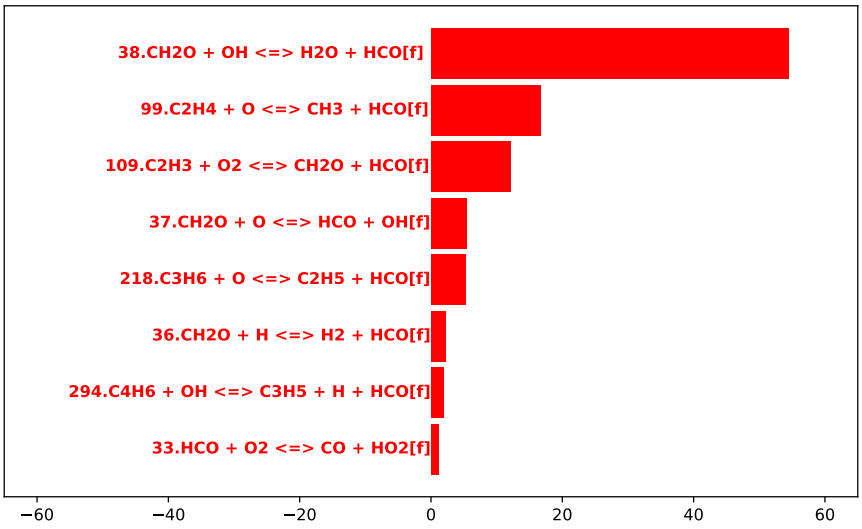

Figure A.6: Contribution on HCO concentration change @4.2mm (n-heptane dominant mixtures)

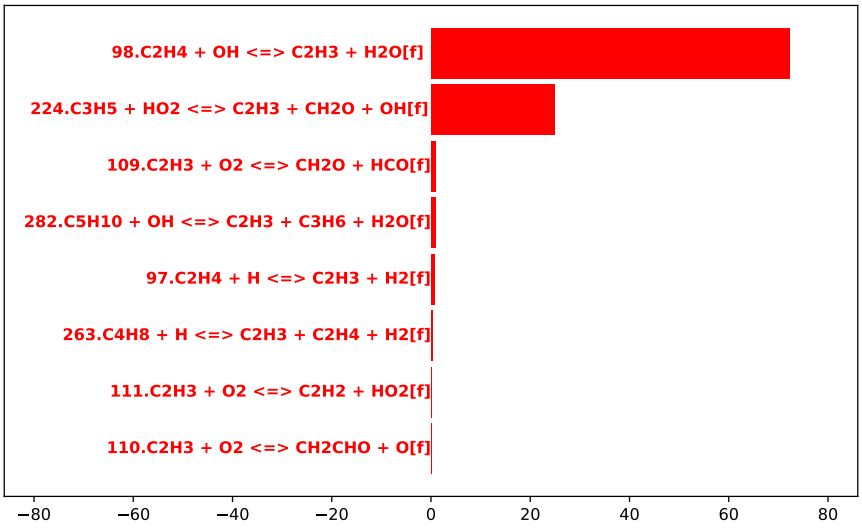

Figure A.7: Contribution on C_2H_3 concentration change @4.2mm (n-heptane dominant mixtures)

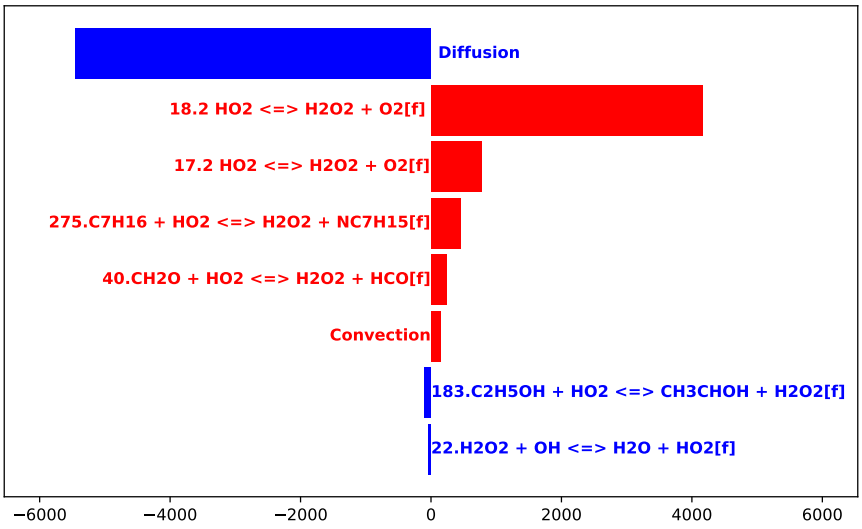

Figure A.8: Contribution on H_2O_2 concentration change @1.1mm (n-heptane dominant mixtures)

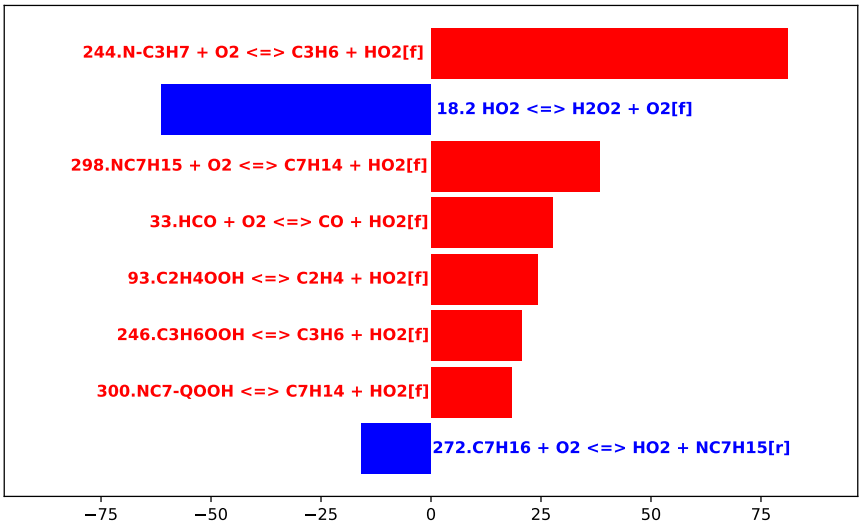

Figure A.9: Contribution on HO_2 concentration change @1.1mm (n-heptane dominant mixtures)

A.1.2 Ethanol Dominant Mixtures

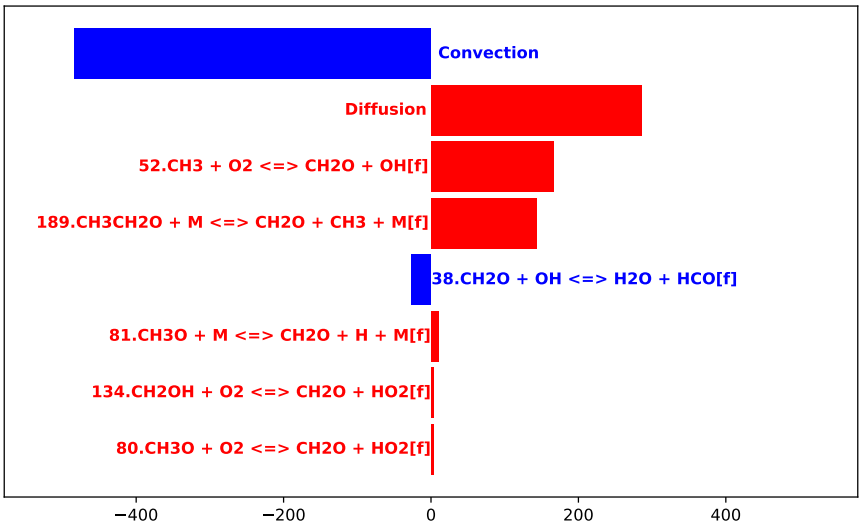

Figure A.10: Contribution on CH_2O concentration change @4.2mm (ethanol dominant mixtures)

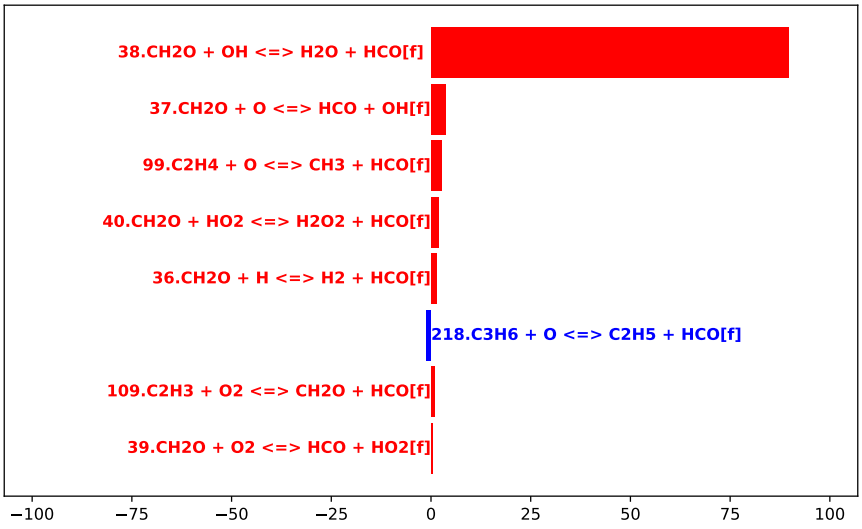

Figure A.11: Contribution on HCO concentration change @4.2mm (ethanol dominant mixtures)

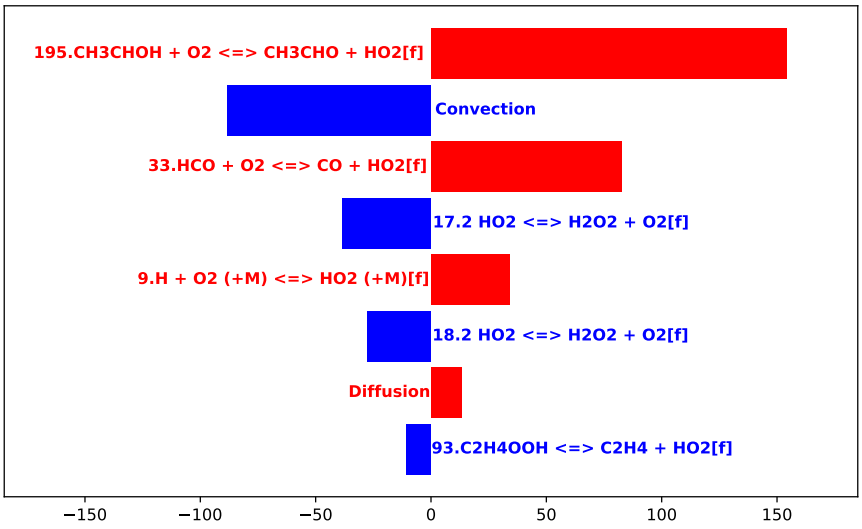

Figure A.12: Contribution on HO_2 concentration change @4.2mm (ethanol dominant mixtures)

Bibliography

[1] https://www.eia.gov/dnav/pet/hist/LeafHandler.ashx?n=PET&s=MGFUPUS1&f=A, 2024.

[2] https://www.eia.gov/dnav/pet/hist/LeafHandler.ashx?n=PET&s=MFERIUS1&f=A, 2024.

[3] S. M. Sarathy, P. Oßwald, N. Hansen, and K. Kohse-Höinghaus. Alcohol combustion chemistry. *Progress in Energy and Combustion Science*, 44:40–102, 2014.

[4] Yuqiang Li, Wei Tang, Yong Chen, Jiangwei Liu, and Chia fon F. Lee. Potential of acetone-butanol-ethanol (ABE) as a biofuel. *Fuel*, 242:673–686, 2019.

[5] George A. Olah. *Beyond Oil and Gas: The Methanol Economy*, volume 44. 2005.

[6] https://www.ers.usda.gov/data-products/u-s-bioenergy-statistics/, 2024.

[7] Chao Jin, Mingfa Yao, Haifeng Liu, Chia fon F. Lee, and Jing Ji. Progress in the production and application of n-butanol as a biofuel. *Renewable and Sustainable Energy Reviews*, 15(8):4080–4106, 2011.

[8] Poonam Singh Nigam and Anoop Singh. Production of liquid biofuels from renewable resources. *Progress in Energy and Combustion Science*, 37(1):52–68, 2011.

[9] Nawa Raj Baral and Ajay Shah. Techno-economic analysis of cellulosic butanol production from corn stover through acetone–butanol–ethanol fermentation. *Energy & Fuels*, 30(7):5779–5790, 2016.

[10] Thaddeus Chukwuemeka Ezeji, Nasib Qureshi, and Victor Ujor. Chapter 7 - isobutanol production from bioenergy crops. In Vijai K. Gupta, Maria G. Tuohy, Christian P. Kubicek, Jack Saddler, and Feng Xu, editors, *Bioenergy Research: Advances and Applications*, pages 109–118. Elsevier, Amsterdam, 2014.

[11] Arthur M. Brownstein. Chapter 5 - isobutanol. In Arthur M. Brownstein, editor, *Renewable Motor Fuels*, pages 47–56. Butterworth-Heinemann, Boston, 2015.

[12] Daniel J. Gaspar, Brian H. West, Danial Ruddy, Trenton J. Wilke, Evgueni Polikarpov, Teresa L. Alleman, Anthe George, Eric Monroe, Ryan W. Davis, Derek Vardon, Andrew D. Sutton, Cameron M. Moore, Pahola T. Benavides, Jennifer Dunn, Mary J. Biddy, Susanne B. Jones, Michael D. Kass, Josh A. Pihl, Melanie M. Debusk, Magnus Sjöberg, Jim Szybist, C. Scott Sluder, Gina Fioroni, and William J. Pitz. Top ten blendstocks for turbocharged gasoline engines: Bioblendstocks with potential to deliver the for highest engine efficiency. 9 2019.

[13] S. M. Sarathy, A. Farooq, and G. T. Kalghatgi. Recent progress in gasoline surrogate fuels. *Progress in Energy and Combustion Science*, 65:67–108, 2018.

[14] R. Grana, A. Frassoldati, T. Faravelli, U. Niemann, E. Ranzi, R. Seiser, R. Cattolica, and K. Seshadri. An experimental and kinetic modeling study of combustion of isomers of butanol. *Combustion and Flame*, 157:2137–2154, 2010.

[15] Alessio Frassoldati, Alberto Cuoci, Tiziano Faravelli, Ulrich Niemann, Eliseo Ranzi, Reinhard Seiser, and Kalyanasundaram Seshadri. An experimental and kinetic modeling study of n-propanol and iso-propanol combustion. *Combustion and Flame*, 157(1):2–16, 2010.

[16] Yujie Wang, Alberto Cuoci, Songtao Guo, Liang Ji, C. Thomas Avedisian, Kalyanasundaram Seshadri, and Alessio Frassoldati. Experimental and numerical investigation of ester droplet combustion: Application to butyl acetate. *Proceedings of the Combustion Institute*, 39(2):2543–2551, 2023.

[17] Yujie Wang, Jun Feng, Songtao Guo, Matthew Haefner, Jie Zhang, Yi Wang, and Thomas Avedisian. Combustion of butyl acetate as an alternative additive to petroleum fuels. 11 2020.

[18] Inna Gorbatenko, Alison S. Tomlin, Malcolm Lawes, and Roger F. Cracknell. Experimental and modelling study of the impacts of n-butanol blending on the auto-ignition behaviour of gasoline and its surrogate at low temperatures. *Proceedings of the Combustion Institute*, 37(1):501–509, 2019.

[19] S. S. Goldsborough, S. Cheng, D. Kang, C Saggese, S. W. Wagnon, and W. J. Pitz. Effects of isoalcohol blending with gasoline on autoignition behavior in a rapid compression machine: Isopropanol and isobutanol. *Proceedings of the Combustion Institute*, 38:5655–5664, 2021.

[20] E. K. Mayhew, C. M. Mitsingas, V. D. Coburn, J. E.G. Temme, and C. M. Kweon. Effects of fuel blending on first stage and overall ignition processes. *Proceedings of the Combustion Institute*, 38:5733–5740, 2021.

[21] Z. Yang, Y. Qian, X. Yang, Y. Wang, Y. Wang, Z. Huang, and X. Lu. Autoignition of

n-butanol/n-heptane blend fuels in a rapid compression machine under low-to-medium temperature ranges. *Energy Fuels*, 27:7800–7808, 2013.

[22] O. Welz, J. D. Savee, A. J. Eskola, L. Sheps, D. L. Osborn, and C. A. Taatjes. Low-temperature combustion chemistry of biofuels: Pathways in the low-temperature (550-700 k) oxidation chemistry of isobutanol and tert-butanol. *Proceedings of the Combustion Institute*, 34:5655–5664, 2013.

[23] Y. Xu and C. T. Avedisian. Combustion of n-butanol, gasoline, and n-butanol/gasoline mixture droplets. *Energy & Fuels*, 29:3467–3475, 2015.

[24] A. Dalili, J. D. Brunson, S. Guo, M. Turello, F. Pizzetti, L. Badiali, C. T. Avedisian, K. Seshadri, A. Cuoci, F. A. Williams, A. Frassoldati, and M. C. Hicks. The role of composition in the combustion of n-heptane/iso-butanol mixtures: Experiments and detailed modelling. *Combustion Theory and Modelling*, 24:1002–1020, 2020.

[25] A. Cuoci, C. T. Avedisian, J. D. Brunson, S. Guo, A. Dalili, Y. Wang, M. Mehl, A. Frassoldati, K. Seshadri, J. E. Dec, and D. Lopez-Pintor. Simulating combustion of a seven-component surrogate for a gasoline/ ethanol blend including soot formation and comparison with experiments. *Fuel*, 288:119451, 2021.

[26] Matteo Pelucchi, Mattia Bissoli, Carlo Cavallotti, Alberto Cuoci, Tiziano Faravelli, Alessio Frassoldati, Eliseo Ranzi, and Alessandro Stagni. Improved kinetic model of the low-temperature oxidation of n-heptane. *Energy & Fuels*, 28(11):7178–7193, 2014.

[27] A. Mzé-Ahmed, K. Hadj-Ali, P. Diévart, and P. Dagaut. Kinetics of oxidation of a synthetic jet fuel in a jet-stirred reactor: Experimental and modeling study. *Energy & Fuels*, 24(9):4904–4911, 2010.

[28] R. Le Dortz, C. Strozzi, J. Sotton, and M. Bellenoue. Evaluation of the surrogates capacity to reproduce the laminar burning velocities and the sensitivity to stretching of a commercial kerosene under constant volume combustion conditions. *Fuel*, 287:119426, 2021.

[29] Ahmet Böğrek, Can Haşimoğlu, Alper Calam, and Bilal Aydoğan. Effects of n-heptane/toluene/ethanol ternary fuel blends on combustion, operating range and emissions in premixed low temperature combustion. *Fuel*, 295:120628, 2021.

[30] Yujie Wang, Andrea Scaboro, Liang Ji, Songtao Guo, Alberto Cuoci, Alessio Frassoldati, and Thomas Avedisian. Droplet burning of n-butyl acetate/n-heptane mixtures in the standard atmosphere: experiments and numerical modeling. 11 2023.

[31] Jiaxiang Zhang, Shaodong Niu, Yingjia Zhang, Chenglong Tang, Xue Jiang, Erjiang Hu, and Zuohua Huang. Experimental and modeling study of the auto-ignition of n-heptane/n-

butanol mixtures. *Combustion and Flame*, 160(1):31–39, 2013.

[32] Yalan Liu and Junxia Ding. Combustion chemistry of n-heptane/ethanol blends: a reaxff study. *Molecular Simulation*, 47(1):37–45, 2021.

[33] J. Shinjo and J. Xia. Combustion characteristics of a single decane/ethanol emulsion droplet and a droplet group under puffing conditions. *Proceedings of the Combustion Institute*, 36(2):2513–2521, 2017.

[34] Kai Zhang, Yishu Xu, Longjiang Qin, Yang Liu, Huakun Wang, Yimin Liu, and Xiaobei Cheng. Experimental and numerical study of soot volume fraction and number density in laminar co-flow diffusion flames of n-decane/n-butanol blends. *Fuel*, 330:125620, 2022.

[35] C.F.H. Tipper and A. Titchard. The effect of additives on the cool flame combustion of n-heptane. *Combustion and Flame*, 16(3):223–232, 1971.

[36] K. Seshadri, S. Humer, and R. Seiser. Activation-energy asymptotic theory of autoignition of condensed hydrocarbon fuels in non-premixed flows with comparison to experiment. *Combustion Theory and Modelling*, 12:831–855, 2008.

[37] K. Seshadri and F. A. Williams. Laminar flow between parallel plates with injection of a reactant at high reynolds number. *International Journal of Heat and Mass Transfer*, 21(2):251–253, February 1978.

[38] T. L. Bergman, A. S. Lavine, F. P. Incropera, and D. P. DeWitt. *Fundamentals of Heat and Mass Transfer*. Wiley, New York, 8 edition, 2017.

[39] William E. Ranz. Evaporation from drops. *Chemical Engineering Progress*, 48:142–180, 1952.

[40] A. Cuoci, A. Frassoldati, T. Faravelli, and E. Ranzi. OpenSMOKE++: an object-oriented framework for the numerical modeling of reactive systems with detailed kinetic mechanisms. *Computer Physics Communications*, 192:237–264, 2015.

[41] A. Cuoci, A. Frassoldati, T. Faravelli, and E. Ranzi. Frequency response of counterflow diffusion flames to strain rate harmonic oscillations. *Combustion Science and Technology*, 180:767–784, 2008.

[42] K. Seshadri, A. Frassoldati, A. Cuoci, T. Faravelli, U. Niemann, P. Weydert, and E. Ranzi. Experimental and kinetic modeling study of combustion of jp-8, its surrogates and components in laminar premixed flows. *Combustion Theory and Modelling*, 15:569–583, 2011.

[43] R. Grana, K. Seshadri, A. Cuoci, U. Niemann, T. Faravelli, and E. Ranzi. Kinetic

modelling of extinction and autoignition of condensed hydrocarbon fuels in non-premixed flows with comparison to experiment. *Combustion and Flame*, 159:130–141, 2012.

[44] U. Niemann, R. Seiser, and K. Seshadri. Ignition and extinction of low molecular weight esters in nonpremixed flows. *Combustion Theory and Modelling*, 14:831–855, 2010.

[45] R. Gehmlich, A. Kuo, and K. Seshadri. Experimental investigations of the influence of pressure on critical extinction conditions of laminar nonpremixed flames burning condensed hydrocarbon fuels, jet fuels, and surrogates. *Proceedings of the Combustion Institute*, 35:937–943, 2014.

[46] D. W. Green and R. H. Perry. *Perry's Chemical Engineers' Handbook*. McGraw Hill, 8 edition, 2008.

[47] The CRECK Modeling Group kinetic mechanisms. https://creckmodeling.chem.polimi.it/menu-kinetics/menu-kinetics-detailed-mechanisms. Version 2003: March 2020.

[48] G. Bagheri, E. Ranzi, M. Pelucchi, A. Parente, A. Frassoldati, and T. Faravelli. Comprehensive kinetic study of combustion technologies for low environmental impact: MILD and OXY-fuel combustion of methane. *Combustion and Flame*, 212:142–155, 2020.

[49] E. Ranzi, C. Cavallotti, A. Cuoci, A. Frassoldati, M. Pelucchi, and T. Faravelli. New reaction classes in the kinetic modeling of low temperature oxidation of n-alkanes. *Combustion and Flame*, 162:1679–1691, 2015.

[50] A. Frassoldati, R. Grana, T. Faravelli, E. Ranzi, P. Oßwald, and K. Kohse-Höinghaus. Detailed kinetic modeling of the combustion of the four butanol isomers in premixed low-pressure flames. *Combustion and Flame*, 159:2295–2311, 2012.

[51] Eliseo Ranzi, Alessio Frassoldati, Silvia Granata, and Tiziano Faravelli. Wide-range kinetic modeling study of the pyrolysis, partial oxidation, and combustion of heavy n-alkanes. *Industrial & Engineering Chemistry Research*, 44(14):5170–5183, 2005.

[52] Judit Zádor, Craig A. Taatjes, and Ravi X. Fernandes. Kinetics of elementary reactions in low-temperature autoignition chemistry. *Progress in Energy and Combustion Science*, 37(4):371–421, 2011.

[53] N. Peters, G. Paczko, R. Seiser, and K. Seshadri. Temperature cross-over and non-thermal runway at two-stage ignition of n-heptane. *Combustion and Flame*, 128:38–59, 2002.

[54] J.P.J. van Lipzig, E.J.K. Nilsson, L.P.H. de Goey, and A.A. Konnov. Laminar burning velocities of n-heptane, iso-octane, ethanol and their binary and tertiary mixtures. *Fuel*, 90(8):2773–2781, 2011.

[55] I. Schifter, L. Diaz, R. Rodriguez, J.P. Gómez, and U. Gonzalez. Combustion and emissions behavior for ethanol–gasoline blends in a single cylinder engine. *Fuel*, 90(12):3586–3592, 2011. Environmental Modeling of Catalytic Reactions in the Oil Refining Industry.

[56] Marco Lubrano Lavadera, Christian Brackmann, Gianluca Capriolo, Torsten Methling, and Alexander A. Konnov. Measurements of the laminar burning velocities and NO concentrations in neat and blended ethanol and n-heptane flames. *Fuel*, 288:119585, 2021.

[57] William J Pitz, Nicholas P Cernansky, Frederick L Dryer, FN Egolfopoulos, JT Farrell, Daniel G Friend, and Heinz Pitsch. Development of an experimental database and chemical kinetic models for surrogate gasoline fuels. *SAE Transactions*, pages 195–216, 2007.

[58] JT Farrell, NP Cernansky, FL Dryer, Chung King Law, DG Friend, CA Hergart, RM McDavid, AK Patel, Charles J Mueller, and Heinz Pitsch. Development of an experimental database and kinetic models for surrogate diesel fuels. Technical report, SAE Technical Paper, 2007.

[59] L. Ji, A. Cuoci, A. Frassoldati, M. Mehl, T. Avedisian, and K. Seshadri. Experimental and computational investigation of the influence of iso-butanol on autoignition of *n*-decane and *n*-heptane in non-premixed flows. *Proceedings of the Combustion Institute*, 39:2007–2015, 2023.

[60] The San Diego Mechanism. http://web.eng.ucsd.edu/mae/groups/combustion/mechanism.html, 2016.

[61] "David G. Goodwin, Harry K. Moffat, Ingmar Schoegl, Raymond L. Speth, and Bryan W. Weber". Cantera: An object-oriented software toolkit for chemical kinetics, thermodynamics, and transport processes., 2023. Version 3.0.0.

[62] Carl L. Yaws. *Yaws' Handbook of Thermodynamic and Physical Properties of Chemical Compounds*. Knovel, 2003.

[63] Gerald Mairinger, Alessio Frassoldati, Ryan Gehmlich, Ulrich Niemann, Alessandro Stagni, Eliseo Ranzi, and Kalyanasundaram Seshadri. Autoignition of condensed hydrocarbon fuels in non-premixed flows at elevated pressures. *Combustion Theory and Modelling*, 20(6):995–1009, 2016.

[64] Song Cheng, Dongil Kang, Aleksandr Fridlyand, S. Scott Goldsborough, Chiara Saggese, Scott Wagnon, Matthew J. McNenly, Marco Mehl, William J. Pitz, and David Vuilleumier. Autoignition behavior of gasoline/ethanol blends at engine-relevant conditions. *Combustion and Flame*, 216:369–384, 2020.

[65] Hiroshi Tsuji. Counterflow diffusion flames. *Prog. Energ. Combust. Sci.*, 8(2):93–119,

1982.

[66] R. Seiser, H. Pitsch, K. Seshadri, W.J. Pitz, and H.J. Gurran. Extinction and autoignition of n-heptane in counterflow configuration. *Proc. Combust. Inst*, 28(2):2029–2037, 2000.

[67] H Rabitz, M Kramer, and D Dacol. Sensitivity analysis in chemical kinetics. *Annu. Rev. Phys. Chem.*, 34(1):419–461, 1983.

[68] Tamas Turanyi. Applications of sensitivity analysis to combustion chemistry. *Reliab. Eng. Syst. Saf.*, 57(1):41–48, 1997. The Role of Sensitivity Analysis in the Corroboration of Models and its Links to Model Structural and Parametric Uncertainty.

[69] Todd A. Oliver Kalen Braman and Venkat Raman. Adjoint-based sensitivity analysis of flames. *Combust. Theor. Model*, 19(1):29–56, 2015.

[70] Wenting Sun, Zheng Chen, Xiaolong Gou, and Yiguang Ju. A path flux analysis method for the reduction of detailed chemical kinetic mechanisms. *Combust. Flame*, 157(7):1298–1307, 2010.

[71] Wei Wang and Xiaolong Gou. An improved path flux analysis with multi generations method for mechanism reduction. *Combust. Theor. Model*, 20(2):203–220, 2016.

[72] Weiqi Ji, Weilun Qiu, Zhiyu Shi, Shaowu Pan, and Sili Deng. Stiff-pinn: Physics-informed neural network for stiff chemical kinetics. *J. Phys. Chem. A*, 125(36):8098–8106, 2021.

[73] Yuting Weng and Dezhi Zhou. Multiscale physics-informed neural networks for stiff chemical kinetics. *J. Phys. Chem. A*, 126(45):8534–8543, 2022.

[74] Xingyu Su, Weiqi Ji, Jian An, Zhuyin Ren, Sili Deng, and Chung K. Law. Kinetics parameter optimization of hydrocarbon fuels via neural ordinary differential equations. *Combust. Flame*, 251:112732, 2023.

[75] Jacek M. Zurada, Aleksander Malinowski, and Shiro Usui. Perturbation method for deleting redundant inputs of perceptron networks. *Neurocomputing*, 14(2):177–193, 1997.

[76] Forman Williams. *Combustion Theory. 2nd edition*. CRC Press, 1 1985.

[77] Shiling Liu, John C. Hewson, Jacqueline H. Chen, and Heinz Pitsch. Effects of strain rate on high-pressure nonpremixed n-heptane autoignition in counterflow. *Combust. Flame*, 137(3):320–339, 2004.

[78] J. Herzler, L. Jerig, and P. Roth. Shock tube study of the ignition of lean n-heptane/air mixtures at intermediate temperatures and high pressures. *Proc. Combust. Inst*, 30(1):1147–1153, 2005.

[79] Cheng Xie, Maxence Lailliau, Gani Issayev, Qiang Xu, Weiye Chen, Philippe Dagaut, Aamir Farooq, S. Mani Sarathy, Lixia Wei, and Zhandong Wang. Revisiting low temperature oxidation chemistry of n-heptane. *Combust. Flame*, 242:112177, 2022.

[80] Tanvir I. Farouk and Frederick L. Dryer. Isolated n-heptane droplet combustion in microgravity: "cool flames" – two-stage combustion. *Combust. Flame*, 161(2):565–581, 2014.

[81] Songtao Guo, Alberto Cuoci, Yujie Wang, C Thomas Avedisian, Liang Ji, Kalyanasundaram Seshadri, Nicholas DiReda, and Frassoldati Alessio. Combustion characteristics of a tier ii gasoline certification fuel and its surrogate with iso-butanol: experiments and detailed numerical modeling. Technical report, American Chemical Society, Chicago, Ill., 2022.

[82] Liang Ji, Kalyanasundaram Seshadri, and Forman A. Williams. Experimental and computational investigation of the influence of ethanol on auto-ignition of n-heptane in non-premixed flows. *Proceedings of the Combustion Institute*, 40(1):105423, 2024.

[83] Joseph Ferrari. *Chapter 4 - Renewable Fuels for Long-Term Energy Storage*, pages 109–138. Elsevier, 2021.

[84] K. Müller, M. Fleige, F. Rachow, and D. Schmeißer. Sabatier based CO2-methanation of flue gas emitted by conventional power plants. *Energy Procedia*, 2013.

[85] W. Boll, G. Hochgesand, and W.-D. Müller. *Methanation and Methane Synthesis*. Wiley-VCH Verlag GmbH & Co. KGaA, Weinheim, 2006.

[86] R. K. Thauer, A.-K. Kaster, H. Seedorf, W. Buckel, and R. Hedderich. Nat. rev. micro. *Nature Reviews Microbiology*, 6:579–591, 2008.

[87] Bin Miao, Su Su Khine Ma, Xin Wang, Haibin Su, and Siew Hwa Chan. Catalysis mechanisms of CO2 and CO methanation. *Catal. Sci. Technol.*, 6:4048–4058, 2016.

[88] G. Alex Mills and Fred W. Steffgen. Catalytic methanation. *Catalysis Reviews*, 8(1):159–210, 1974.

[89] M.P. Andersson, F. Abild-Pedersen, I.N. Remediakis, T. Bligaard, G. Jones, J. Engbæk, O. Lytken, S. Horch, J.H. Nielsen, J. Sehested, J.R. Rostrup-Nielsen, J.K. Nørskov, and I. Chorkendorff. Structure sensitivity of the methanation reaction: H2-induced CO dissociation on nickel surfaces. *Journal of Catalysis*, 255(1):6–19, 2008.

[90] Guojing Jin, Fangna Gu, Qing Liu, Xiaoyan Wang, Lihua Jia, Guangwen Xu, Ziyi Zhong, and Fabing Su. Highly stable Ni/SiC catalyst modified by Al2O3 for CO methanation reaction. *RSC Adv.*, 2016.

[91] Tinku Baidya, Robert Cattolica, and Reinhard Seiser. Ni-Ru-MgO catalyst with high activity and stability for methanation of syngas and producer gas. *Catalysis Today*, 397-399:69–80, 2022. SI:CCE-2021.

[92] Stefan Bajohr, Jens Schneider, Steffi Matthischke, Michael Schlüter, Manuel Götz, Jonathan Lefebvre, Praseeth Prabhakaran, and Siegfried. Review on methanation – from fundamentals to current projects. *Fuel*, 2016.

[93] A.L. Kustov, A.M. Frey, K.E. Larsen, T. Johannessen, J.K. Nørskov, and C.H. Christensen. CO methanation over supported bimetallic ni–fe catalysts: From computational studies towards catalyst optimization. *Applied Catalysis A: General*, 320:98–104, 2007.

[94] Shin-Kun Ryi, Sung-Wook Lee, Kyung-Ran Hwang, and Jong-Soo Park. Production of synthetic natural gas by means of a catalytic nickel membrane. *Fuel*, 94:64–69, 2012.

[95] Jens Sehested. Four challenges for nickel steam-reforming catalysts. *Catalysis Today*, 111(1):103–110, 2006. Frontiers in Catalysis: A Molecular View of Industrial Catalysis.

[96] Meng Guo and Gongxuan Lu. The effect of impregnation strategy on structural characters and CO2 methanation properties over MgO modified Ni/SiO2 catalysts. *Catalysis Communications*, 54:55–60, 2014.

[97] H.G.J. Lansink Rotgerink, R.P.A.M. Paalman, J.G. van Ommen, and J.R.H. Ross. Studies on the promotion of nickel—alumina coprecipitated catalysts: Ii. Lanthanum oxide. *Applied Catalysis*, 45(2):257–280, 1988.

[98] Hezhi Liu, Xiujing Zou, Xueguang Wang, Xionggang Lu, and Weizhong Ding. Effect of CeO2 addition on Ni/Al2O3 catalysts for methanation of carbon dioxide with hydrogen. *Journal of Natural Gas Chemistry*, 21(6):703–707, 2012.

[99] Sudhanshu Sharma, Zhenpeng Hu, Peng Zhang, Eric W. McFarland, and Horia Metiu. CO2 methanation on Ru-doped ceria. *Journal of Catalysis*, 278:297–309, 2011.

[100] Robert Cattolica, Reinhard Seiser, and Tinku Baidya. Catalyst for the methanation of syngas and producer gas, Jan 2022. The Regents of the University of California.

[101] Reinhard Seiser, Robert Cattolica, and Michael Long. Renewable natural gas production from woody biomass via gasification and fluidized-bed methanation. Final Project Report CEC-500-2020-055, California Energy Commission, August 2020.

[102] Sujata Brahma, Biswajit Nath, Bidangshri Basumatary, Bipul Das, Pankaj Saikia, Khemnath Patir, and Sanjay Basumatary. Biodiesel production from mixed oils: A sustainable approach towards industrial biofuel production. *Chemical Engineering Journal Advances*, 10:100284, 2022.